

**Fabrication of high quality, low bandgap amorphous Silicon & amorphous Silicon
Germanium alloy solar cells by chemical Annealing**

By

Ashutosh Shyam

A dissertation submitted to the graduate faculty
in partial fulfillment of the requirements for the degree of

DOCTOR OF PHILOSOPHY

Major: Electrical Engineering

Graduate Committee:

Vikram Dalal, Major Professor

Joseph Shinar

Mani Mina

Sumit Chaudhury

Rana Biswas

Iowa State University

Ames, Iowa

2011

Copyright © Ashutosh Shyam, 2011. All rights reserved

TABLE OF CONTENTS

LIST OF FIGURES	(iii)
LIST OF TABLES	(vi)
ABSTRACT	(vii)
CHAPTER 1. INTRODUCTIONS	1
1.1 Research Motivation	1
1.2 Operation Of Solar Cells	3
1.3 Properties Of A-Si:H &A-SiGe	3
1.4 Literature Review	9
1.5 Outline Of Research	21
CHAPTER 2. RESEARCH METHODOLOGY	22
2.1 Design Of Solar Cell Structure	22
2.2 Growth Mechanism Of Chemical Annealing	25
2.3 Fabrication Technique	29
CHAPTER 3. CHARACTERIZATION	35
3.1 Device Characterization	35
3.2 Film Characterization	46
CHAPTER 4. RESULTS	52
4.1 Amorphous Silicon Chemical Annealing	52
4.2 Amorphous Silicon Germanium Chemical Annealing	69
CHAPTER 5 CONCLUSIONS	91
REFERENCES	92
ACKNOWLEDGEMENTS	99

LIST OF FIGURES

Figure 1.1 Schematic representation of chemical annealing	2
Figure 1.2 Electrical equivalent of A-Si/ A-SiGe solar cell	3
Figure 1.3 Continuous random structure of a-Si	4
Figure 1.4 Electronic density of states in a-Si:H as per (a)[40],b[16].	5
Figure 1.5 Electronic density of states in a-Si:H as per defect pool model[30]	7
Figure 1.6 Optical absorption coefficient of a-Si:H [1]	8
Figure 1.7 Raman scattering data for a-Si:H film before and after H ₂ plasma treatment [41]	10
Figure 1.8 Effect of light soaking on CA vs NON CA[59]	13
Figure 1.9 Effect of pressure on various parameters [60]	14
Figure 1.10 (a) Photoconductivities of the various films deposited as function of Growth temp , for different dilution of GeH ₄ (b) Variation of optical band gaps is represented by with substrate temperature & (c) Photoconductivity with respect to optical band gaps for a-SiGe - samples corresponding to (a) and (b).	15
Figure 1.11 Variations of deposition rate, photoconductivity and dark conductivity with R.	16
Figure 1.12 Variation of Urbach energy with R.	16
Figure 1.13 Urbach energy of ECR fabricated film compared with glow discharge generated films	18
Figure 1.14 Effect of pressure on quality of the material [64]	19
Figure 1.15 Effect of temp on Urbach energy[64]	19
Figure 1.16 Properties of He dilution vs He and H dilution films	20
Figure 2.1 (a) Structure of typical a-Si solar cells (b) Band diagram of a-Si solar cell	22
Figure 2.2 Band diagram of a hole trap	23
Figure 2.3 Iv curve of a device with improper buffer layer	24
Figure 2.4 Band diagram of the a-SiGe I layer device followed by our group	24
Figure 2.5 Band diagram of the complete PIN a-SiGe device followed by our group	24
Figure 2.6 (a) Homogeneous growth chemistry of a-Si(b) Ill effect of SiH ₂	26
Figure 2.7 Design of VHF PECVD used	30
Figure 2.8 Schematic of sputter system [80]	33
Figure 2.9 Transmission vs wavelength plot for ITO	34
Figure 3.1 QE experimental setup	35
Figure 3.2 Lower vs higher bandgap material absorption energy curve	37
Figure 3.3 Norm QE plot at 0 & +.5 bias for various wavelengths for a high FF A-Si device	38
Figure 3.4 QE ratio plot for various wavelengths for a high quality A-Si device (FF~ 65%)	39
Figure 3.5 Simulated electric field profiles in p-i-n diode for varying values of the carrier band mobilities	40

Figure 3.6 Typical IV curve	42
Figure 3.7 Sample Capacitance voltage measurement	44
Figure 3.8 Basic principle of trap measurement using differential capacitance techniques	45
Figure 3.9 Capacitance measurements as a function of temperature and frequency	45
Figure 3.10 Raman spectrum for Crystalline, amorphous and mixed phase	48
Figure 3.11 Cr contacts evaporated on top of the film used for photo/ dark conductivity & activation energy measurement.	49
Figure 3.12 Plot of Ln (I) vs 1/T	50
Figure 4.1 Effect of varying growth time and annealing time	52
Figure 4.2 Penetration depth for H as function of Ion energy	53
Figure 4.3 Penetration depth for H as function of Ion energy	53
Figure 4.4 Damage due to 50eV Ar ions	54
Figure 4.5 Absorption energy plot for growth rate of 9.8 A/cycle and 17.6 A/cycle.	55
Figure 4.6 Effect of varying pressure on bandgap of the material	56
Figure 4.7 Raman data for CA device with H in annealing stage	56
Figure 4.8 Iv curve for 9A/cycle CA device	57
Figure 4.9 IV curve for NON CA sample	57
Figure 4.10 Plot of Voc for various CA and NON CA devices	58
Figure 4.11 Absorption energy plots for CA vs NON CA (Ar) and NON CA (H ₂)	58
Figure 4.12 Effect of light soaking on (a)Voc (b) J _{sc} degradation for CA and NON CA devices as a function of time of exposure (hrs)	59
Figure 4.13 Effect of light soaking on FF degradation for CA and NON CA devices as a function of time of exposure (hrs)	59
Figure 4.14 Absorption energy data for CA before and after light soaking	60
Figure 4.15 Absorption energy data for (a) NON CA before and after light soaking	60
Figure 4.16 Qe ratio (0/+5) data for CA before and after light soaking	61
Figure 4.17 Qe ratio (0/+5) data for NON CA (Ar) before and after light soaking	61
Figure 4.18 Absorption energy data for CA and NON CA device selected for hole mobility-lifetime product measurement	62
Figure 4.19 Simulation and measured Qe vs bias for 1.65 eV CA device at (a) 760 nm (b) 600 nm and (c) 680 nm	63
Figure 4.20 Simulation and measured Qe vs bias for NON CA (Ar) device at (a) 760 nm (b) 600 nm and (c) 680 nm	64
Figure 4.21 Plot of defect density for CA vs NON CA devices	65
Figure 4.22 Hydrogen content as a function of various CA and non CA parameters	65
Figure 4.23 FTIR data for various CA and non CA parameters	66

Figure 4.24 Absorption energy curves for CA(10 A/cycle) and NON CA films	67
Figure 4.25 band diagram for A-SiGe I layer fabrication in this research work	69
Figure 4.26 First non CA fabricated	70
Figure 4.27 Better quality non CA fabricated	70
Figure 4.28 Qe ratio for (i) first non CA device (ii) optimized non CA device	71
Figure 4.29 Effect of Hydrogen etching on device quality	71
Figure 4.30 Absorption energy curves for CA and non CA films	72
Figure 4.31 Back scattered image for CA vs NON CA	73
Figure 4.32 Effect of power on CA - absorption energy plot for 4.5 w Rf vs 2 W RF	73
Figure 4.33 Effect of dilutant gas – H ₂ vs H ₂ and Ar	74
Figure 4.34 Effect of pressure – 30 mtorr vs 50 mtorr	75
Figure 4.35 Effect of varying growth time – 15s vs 20 s.	76
Figure 4.36 IV curve for CA device	77
Figure 4.37 NON CA Iv curve	77
Figure 4.38 Voc as a function of various CA and non CA parameter	78
Figure 4.39 Effect of doubling Hydrogen dilution	78
Figure 4.40 absorption energy curve for case 1 , 2 & 3	79
Figure 4.41 Backscattered image comparing Ge content for Case 1 vs Case 3	80
Figure 4.42 Backscattered image comparing Ge content for Case 1 vs Case 2	80
Figure 4.43 Raman data for higher power (4W RF) film	81
Figure 4.44 Raman data for low power (2W RF) film	81
Figure 4.45 Best quality CA device till now	82
Figure 4.46 best quality NON CA till now	82
Figure 4.47 Absorption energy curve for CA vs NON CA	83
Figure 4.48 Simulation and measured Qe vs bias for 1.63 eV NON CA device at (a) 600 nm (b) 680 nm and (c) 760 nm	84
Figure 4.49 Simulation and measured Qe vs bias for 1.56 eV CA device at (a) 600 nm (b) 680 nm and (c) 760 nm	85
Figure 4.50 Density of states plot for CA and NON CA	85
Figure 4.51 Absorption energy curve for CA vs NON CA devices	86
Figure 4.52 Hydrogen content data for CA vs NON CA	86
Figure 4.53 FTIR raw data obtained –for various CA conditions and NON CA	87
Figure 4.54 Comparison of Absorption energy curves for Ca vs NON CA obtained by Spectrophotometry	89

LIST OF TABLES

Table 1.1 Electronic properties of A-SiGe vs A-Si	9
Table 4.1 Comparison of optical and electronic properties of CA and NON CA A-Si films	66
Table 4.2 Table for various films with different SiH₄, GeH₄, Rf power and their corresponding Ge content	79
Table 4.3 Comparison of optical and electronic properties of CA and NON CA A-SiGe films	88

ABSTRACT

Amorphous Silicon (a-Si:H) has been extensively used as a solar cell material because of its low cost and ease of fabrication. However, the material suffers from generally poorer quality and increase in defect states in response to illumination (Staebler-Wronski effect). For best devices, one also needs to control the bandgap of the material, which depends strongly upon localized Si-H bonding. Although many techniques have been developed to fabricate lower bandgap materials in a-Si:H, most of them lead to the lowering of bandgap at the expense of device /film quality. In this research, we pursue Chemical Annealing (or layer-by-layer growth followed by controlled Ar ion bombardment) as a technique which for fabricating low bandgap, amorphous Silicon materials and devices without adversely affecting the quality of the material. We explore the growth and properties of both a-Si:H and its alloy, a-(Si,Ge):H using chemical annealing.

In this work, chemical annealed (CA) and non chemical annealed (NON CA) A-Si:H and A-(Si,Ge):H devices were fabricated at VHF (48MHz) which leads to lower ion damage by Ar. Systematic experiments were carried out to produce high quality devices to study the role of chemical annealing in lowering the bandgap of the solar cells. Films were also fabricated to study electronic properties for various annealing conditions and also to highlight the relationship between hydrogen content and bandgap. Detailed measurements of fundamental properties of the materials and devices were made under various chemical annealing conditions. We also performed light soaking experiments to study the photo-induced instability of normal and chemically annealed devices. The results indicate that the stability of chemical annealed samples is better than continuously grown samples. All the studies convincingly prove that chemical annealing helps reduce the bandgap without adversely affecting material properties.

CHAPTER 1 INTRODUCTION

1.1 Research motivation

Hydrogenated amorphous silicon (a-Si:H) is used for a several applications such as thin film transistor[1][2][3][4], solar cells[1][2][5][6][7][8][9], LCD[3], photosensors [10], photoreceptors[11][12]. The advantages of A-Si is that it is cheaper to fabricate as compared to crystalline Silicon solar cells and also it has high absorption coefficient over visible region of solar spectrum as it acts like a direct bandgap material because the law of conservation of momentum is relaxed [13]. A-SiGe similarly provides us with the alternative of fabrication low bandgap solar cells, but it is affected by the presence of greater defect density.

Although A-Si offers such favorable properties, it suffers from the problem of light induced degradation, commonly known as Staebler-Wronski (S-W) effect [14] (named after the 2 scientists involved in its discovery and understanding). This effect has been seen to lead to severe degradation in photoconductivity, due to increase in defect densities; thus adversely affect solar cell properties [14]. The traditional approach has been to fabricate devices at higher temperature as this leads to cleavage of the weak Si-H and provides a more dense structure since at the high temperature, the growth inducing radicals are more mobile. However, the disadvantage of such high temperature fabrication is that it frequently leads to the creation of additional defect states by the cleavage of weak Si-H or Si-Si bonds [2].

We propose chemical annealing as a technique for reducing bandgap of material without adversely affecting device properties. Let us first briefly go through definition and advantages of chemical annealing.

(a) Chemical annealing

Very recently, a novel technique called “Chemical annealing (CA)” or “layer by layer deposition” [15] was introduced to remove the excess H and improve the stability of a-Si:H. The process essentially comprises of many repetitive cycles or layers. In each cycle

a layer of thin a-Si:H or (a-SiGe):H is grown and followed by an Argon Ion bombardment [15]. The thickness of the layer is restricted to 7-15 Å per cycle in order to ensure effective chemical annealing.

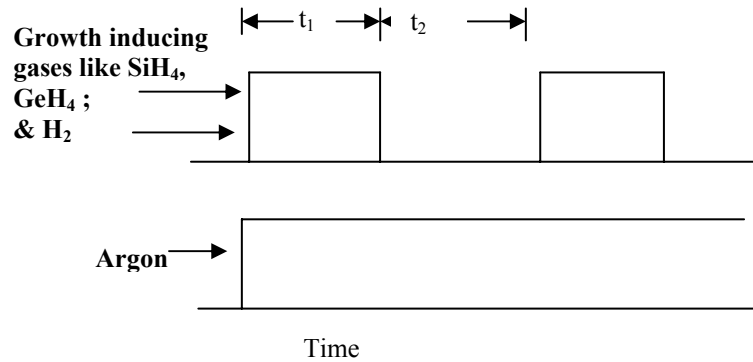


Figure 1.1 Schematic representation of chemical annealing- t_1 , t_2 are the growth and annealing time respectively

(I) Advantages of chemical annealing

- (i) In each cycle, growth of a thin layer of film is succeeded by ion bombardment [15] - which is believed to be a very successful technique for reducing hydrogen content.
- (ii) Among the existing technique for A-Si/A-SiGe bandgap engineering, it can considered to be the most efficient technique - the bandgap of a-Si:H and a-(Si,Ge):H is known to vary with the H content. This fact can be made use of in fabricating a-Si:H and a-(Si,Ge):H alloy with bandgap that can be varied via chemical annealing , which then can be used in fabricating tandem solar cells.
- (iii) The loose Si-H and Ge-H bonds are reduced significantly
- (iv) Stability of devices is improved greatly as it reduces Staebler – Wronski effect [15].

Before we go on to understand the effect of chemical annealing in details we should first try to understand the operation of a typical solar cell.

1.2 Operation of Solar Cell

The electrical equivalent of Solar cell is shown in Figure.1.2 below. In essence a simple thin film solar cell comprises of P and N doped semiconductor with an intrinsic layer in the middle or in other words, p-i-n diode. When light is shone on the device, electron hole pairs are generated in the intrinsic layer. The internal electric field plays an important role in carriers being collected [2] and can be attributed to space charge conditions- this is very important especially for Amorphous Si/A-SiGe where diffusion length cannot be relied on for carrier collection. The holes or the positively charged carriers are collected at the p region while the negatively charged electrons move towards and are collected at the n region. When a load is connected across the solar cell, the charges come out, giving rise to electric current. As can be seen from the Figure below, the two major sources of losses are – series resistance and shunt resistance. The series resistance affects the short circuit current, whereas the Shunt resistance affects open circuit voltage. The third source of loss is carrier collection losses under forward bias.

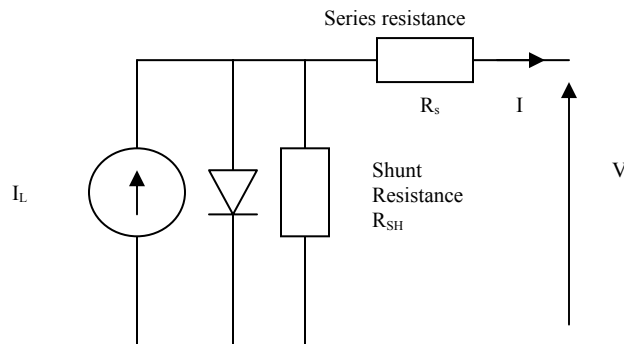


Figure 1.2 Electrical equivalent of A-Si/ A-SiGe solar cell

1.3 Fundamental properties of a-Si:H and A-(Si,Ge):H

(a) General properties

Fabrication techniques, such as plasma-enhanced chemical vapor deposition (PECVD), hot wire-chemical vapor deposition, photo assisted CVD, reactive sputtering can be used to produce amorphous Silicon [2]. The structural and electronic properties of A-Si has been studied extensively [2], with much understanding of how electronic properties relate

to local structural order [2]. By definition, Amorphous Silicon films containing about 4 to 40 atomic percentage of hydrogen are generally denoted as a-Si:H [2]. Unlike the crystallite silicon material, A-Si:H has only a short range order which means that all four covalent bonds of Si atoms might not be saturated [16]. Thus it has a continuous random network structure model [16], in which Si has unsaturated bonds as shown below [17].

Si atoms with unsaturated bonds occur as it releases the strain associated with the disordered structure [2]. Commonly known as dangling bonds, they act as recombination centers and thus lead to poor quality solar cells. Hydrogen passivation can be considered the best technique to reduce their concentration. The single electron of hydrogen atom can convert the unsaturated Si atoms to four fold coordinated ones .

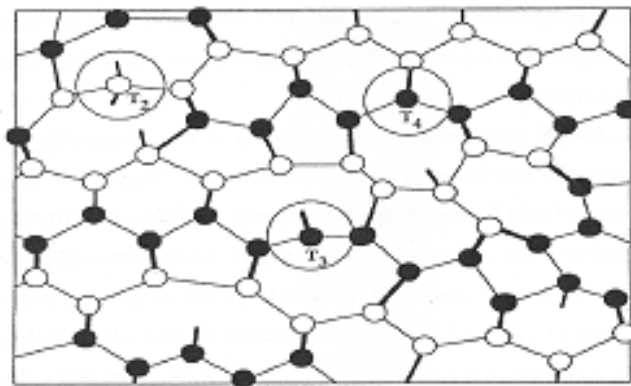


Figure 1.3 Continuous random structure of a-Si [17]

Thus Hydrogen Passivation is successful in removing dangling bonds [18]. It has been shown by other groups that dangling bond concentration can be reduced from 10^{22} to 10^{15} cm^{-3} [18] using this technique.

For complete understanding of the working of A-Si solar cells, it is important to determine the distribution of the trap states in the bandgap. Figure 1.4 shows a density of states curve for a undoped a-Si:H film [26][50]. Like Crystalline Silicon, the existence of extended valence and conduction band states is observed. However, the presence of short range order and distortion of the covalent bonds of fourfold co-ordinated neutral silicon atoms in amorphous structure gives rise to an exponential decrease of the density of states, also known as band tails [19],[20] and are given by

$$G_C = G_{C0} \exp [(E_C - E)/E_{urc}] \quad \dots\dots\dots 1$$

$$G_V = G_{V0} \exp [(E - E_V)/E_{urv}] \quad \dots\dots\dots 2$$

where G_C and G_V are density of states for conduction band tail states and valence band tail states respectively; and E_{urv} and E_{urc} are the measure of penetration of the conduction and valence band tails into the forbidden gap respectively, called the Urbach energy. For a good quality a-Si:H solar cells, the typical values of $E_{urv} = 42\text{-}45\text{meV}$ [21], [22], [23] and $E_{urc} = 26\text{meV}$ [24], which means that valence band tail extends deeper into the forbidden gap. Low Urbach energy means lesser disorder, which is a very important property of amorphous a-Si:H. It should be noted that a fraction of defect states also can be attributed to silicon atoms having three silicon neighbors and one hydrogen atom in tetrahedral configuration. These extra states change the Tauc's bandgap, depending on the hydrogen content- from about 1.5eV for pure A-Si to almost 2.0eV when 30 at. % H content is recorded [13]. Very close to the tail states exists several deep-level bands in the forbidden gap, believed to be related to dangling bonds [2].

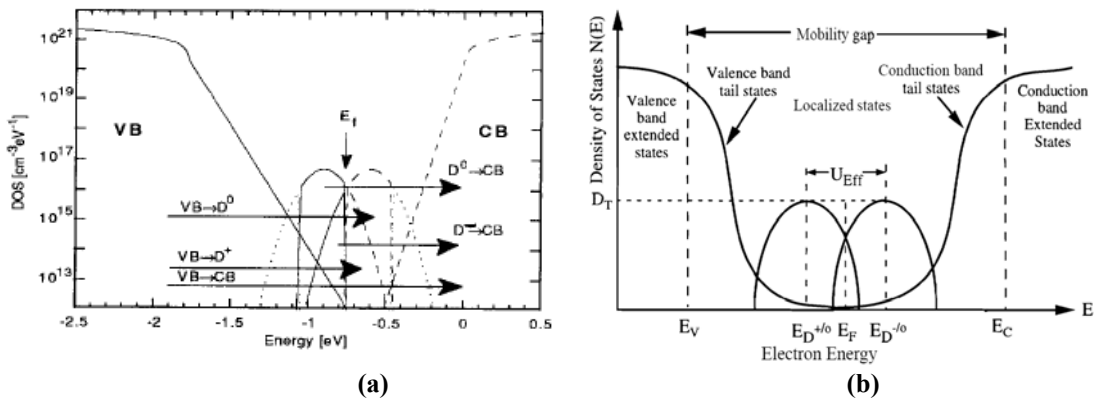


Figure 1.4 Electronic density of states in a-Si:H as per (a)[50],b[26].

The bandedge and midgap region of Density of state plot for Amorphous entails further deeper study. As we can see from Figure 3(b) that a boundary exists (known as mobility edge, as suggested by Mott et al [25]), which separates two regions ie high mobility region (or extended states), where electrons and holes are helped by band transport from localized region or low mobility region, where carriers undergo hopping conduction. The midgap region observed in Amorphous silicon region has been explained by Davis and Mott [26] by making use of “bands of compensated levels”[19] near the midgap, which

can be attributed to defects such as dangling bonds present in the material [19], which can be empty or positively charged (D^+), neutral (D^0) or negatively (D^-) charged. The D^0 and D^- energy levels are separated by a correlation energy, U_{eff} , which is attributed to the repulsion between electrons. Marshall and Owen's Amorphous Silicon density of state model [27] highlighted the presence of bands of donors and acceptors in the upper and lower halves of the mobility gap similar to Davis and Mott model [26], which facilitated derivation of "realistic gap state models" [19]. Characteristics of these states have been assessed from such experiments like photoluminescence [28], [29], electron spin resonance (ESR) [30], and optically detected magnetic resonance (ODMR) [31]. Some defect states are obtained during the growth of the film due to hydrogen evolution from films [32]. Others seem to be related to "microstructural imperfections" [19] such as polymer chains [33] with contaminants like oxygen, carbon and other dopants [34] [35]. Other defect levels may arise from foreign atoms and neighboring dangling bonds interactions, and weak bonds between Si and other atoms [19]. The sign of U_{eff} is still controversial and is still subject of lot of debate. Dersch et al. [22] has approximated it as 0.4 eV from ESR on undoped and doped a-Si:H samples, assuming a positive dangling bond [19]. Stutzmann [36] estimated it to be 0.2 eV by EDS and Photothermal Deflection Spectroscopy (PDS). Negative U_{eff} has been proposed by Elliot [37], [38], Adler [39] and also Bar-Yam [40], who established the value of it to be about -2eV based on detailed calculation [40] and claimed that this might not be observed during the ESR measurement. Furthermore, Stutzmann has observed isomorphic nature of negative U_{eff} model and the weak bond-dangling bond conversion model [41]. In the positive U_{eff} model, it has been shown that D^0 is about 1.0 ~ 1.25eV below conduction band, while D^- is about .25 ~ .45eV higher than D^0 level [19].

The thermal equilibrium model or otherwise known as defect pool model [40][42][43][44][45] has been developed to explain the increase in defect density due to doping [46] or light soaking or charge injection [47]. Unlike the aforementioned models, this model assumes that dangling bonds levels are associated with different types of dangling bonds, created in different energy ranges of defect pools. Winer [48] found that

the D^0 and D^- bands are positioned at σ_{DB}^2/E_{urv} and $2\sigma_{DB}^2/(E_{urv}-U_{eff})$ respectively below the D^+ level, where pool center is believed to be present [19] where σ_{DB} is standard deviation of dangling bond state, E_{urv} is Urbach energy of valence band tail. Thus each of 3 defects have two energy levels [49], which can make matters complicated. So for the purpose of simplicity, we will work with the simple Davis and Mott's model.

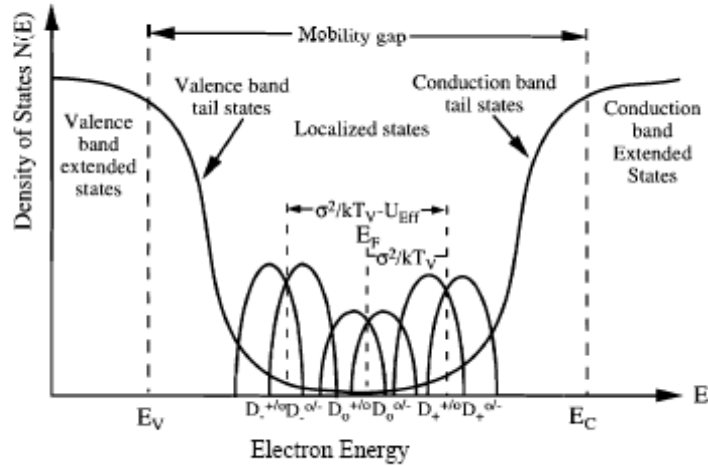


Figure 1.5 Electronic density of states in a-Si:H as per defect pool model [40][19]

Since crystalline silicon is an indirect bandgap material it exhibits low absorption in visible region as very few electronic states close to the band edge can participate in the absorption, in accordance with the momentum conservation law and also due to involvement of phonons. However, as against this, in amorphous Silicon due to presence of the tail states near the band edges which facilitate optical transitions, the law of conservation of momentum is relaxed with the result that optical absorption coefficient is much higher than that of C-Si [2].

Figure 1.6 shows a typical example of the absorption energy plot of an undoped a-Si:H. It can be broadly divided into three regions, which are – (i) region A - very commonly denoted as “Tauc region”, where the absorption is given by equation 3, and is due to the transfer of electron from the extended valence band and the conduction band:

$$\alpha \hbar\omega = B(\hbar\omega - E_{tauc})^2 \dots\dots\dots 3$$

where E_{tauc} is known as the Tauc gap, and is conventionally used for reporting the bandgap of amorphous semiconductors. (ii) Region B is defined as the “Urbach region” and mathematically denoted by the following equation:

$$\alpha = \alpha_0 \text{Exp}((h\nu - E_g)/E_{\text{urv}}) \quad \dots\dots\dots 4$$

where E_{urv} is called the Urbach energy. This region can be attributed to the transfer of electrons between the valence band tail state and an extended conduction band. (iii) Finally, region C can be said to be present because of mid-gap state absorption. More defective is the material, higher is the Urbach energy and higher is midgap state – absorption which automatically translates into higher midgap defect density. This has been made use of in our research as discussed in result section.

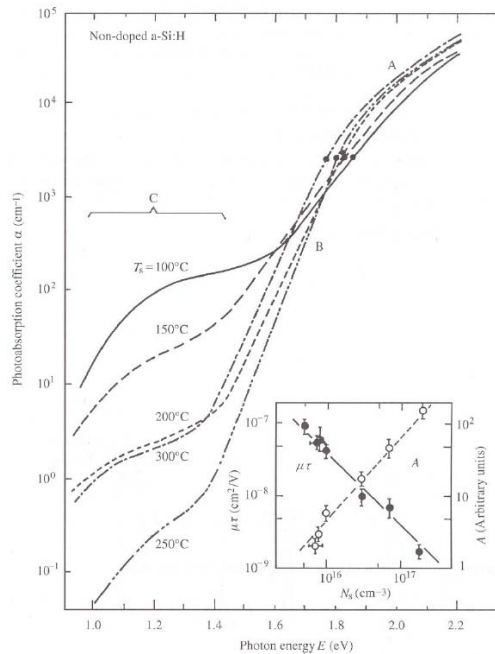


Figure 1.6 Optical absorption coefficient of a-Si:H [12]

Some prominent properties of device-quality a-Si:H are given[13] below:-

- (i) Bandgap: 1.62 to 1.8 eV
- (ii) Urbach energy: 42 to 45 meV
- (iii) Photoconductivity: 10^{-4} S/cm to 10^{-5} S/cm
- (iv) Dark conductivity: 10^{-10} S/cm to 10^{-11} S/cm

(v) $\mu\tau$ (mobility-lifetime product) for hole: $\geq 3-5 \times 10^{-8} \text{cm}^2/\text{V}$

For A-SiGe, the situation is similar to A-Si with the exception that material quality is even worse. The table 1.1 allows us to compare properties of a typical A-Si solar cell material with that of an A-SiGe and it can be seen that both Urbach energy and hole mobility lifetime product is higher for A-SiGe than that for A-Si, clearly indicating poor quality.

Table 1.1 Electronic properties of A-SiGe vs A-Si [50]

Properties	a-Si:H	a-SiGe:H
Band Gap	1.7-1.9eV	1.0-1.7eV
Urbach Energy	42-45meV	>45meV
Photoconductivity	10^{-4} s/cm to 10^{-5} s/cm	10^{-5} s/cm - 10^{-7} s/cm
Hole $\mu\tau$	$3-5 \times 10^{-8} \text{ cm}^2/\text{v}^{-1}$	$10^{-8} \text{ cm}^2/\text{v}^{-1}$ to $10^{-10} \text{ cm}^2/\text{v}^{-1}$

A-SiGe has poorer properties than A-Si as H has preferential tendency to attach itself to Si rather than Ge, leading to weaker Ge-H bonds. Besides Germynl radicals are bulkier than Silyl radicals, which impedes their mobility and thus promotes formation of voids. Also there is greater dihydride bond formation tendency for A-SiGe, which leads to worse electronic properties as well.

Before discussing my research, it would be worthwhile to go through research done by other group in this area. This would enable us to understand the importance of our work.

1.4 Literature survey

(a) Amorphous silicon Chemical annealing by other groups

First evidence for chemical annealing was provided by Hirose group, wherein it was proved that Chemical annealing using H plasma significantly improves microstructure of the film. Using the Raman scattering Figure, given below for a 2nm a-Si:H, it has been shown that post H₂ plasma treatment , intensity of SiH_x wagging mode is decreased ,

while that due to a-Si TO like phonon increased, thus proving hydrogen desorption from film during the plasma treatment which actually led to improvement of microstructure[51]

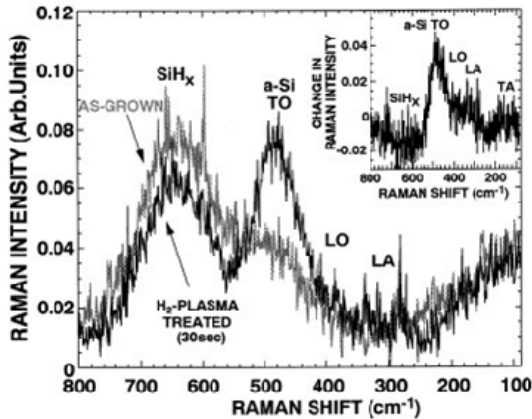


Figure 1.7 Raman scattering data for a-Si:H film before and after H₂ plasma treatment [51].

Thereafter, work on chemical annealing has been mainly restricted to Shimizu group. Futako et al [52] reported amorphous silicon materials with optical band gaps of 1.6 eV prepared using chemical annealing technique employing hydrogen and argon mixtures. As per them, Hydrogen CA has been observed to either increase the band gap of amorphous silicon through increased hydrogen bonding at low substrate temperature or to induce microcrystalline silicon formation at high substrate temperature. This explains why hydrogen CA has not been observed to result in amorphous silicon materials having an optical band gap less than that of standard 1.7 eV band-gap materials.

Later on Shimizu et al [53], [54] achieved bandgap below 1.6 eV by keeping H content below 3at.%. They maintained growth time and annealing time of 5 and 10 sec respectively, and temperature of 300-350° C. Although their device stability did improve quite a bit, Urbach energies were poor (58-62 meV) and defect densities were around the high 10^{16} cm^{-3} .

Soon after, Sato et al [55] achieved low bandgap of 1.58eV. Fabrication of the I layer was done by a (RF-PECVD) apparatus which had a microwave (MW) plasma generator to

provide a high-density, excited Ar. But the solar cells fabricated by his group had poor a FF of .57 and low Voc of .7 and Isc of 5 mA/cm².

So we can see that although the Shimizu group had successfully fabricated low bandgap a-Si solar cells, till date no good quality a-Si solar cell has been fabricated by the group. Thus the objective of our research is to decrease the bandgap without adversely affecting the solar cell quality.

One of the other aspects of chemical annealing is the ability to improve stability of the material. The Section below is dedicated to explaining the exact physics behind it with the assistance of several models proposed.

(I) Improvement of stability by chemical annealing

The instability of an a-Si:H can be attributed to its non-equilibrium state, so it is obvious that any thermal or optical external disturbance, will cause structural changes in the material [14]. When exposed to light, electron-hole pairs are created which recombine in the film, release energy and ultimately leads to breakage of weak Si-Si and /or Si-H bonds facilitating creation of defects, which in turn deteriorates the conductivity of the film [14]. The film degradation process can be explained by these models: (i) the Trap to dangling bond conversion model, suggested first by Adler and quantified later by Dalal [56], indicates when positively correlated dangling bonds (D^0) and negatively correlated charged defect states (D^- and D^+) capture an oppositely charged carriers it gets converted into a positively correlated dangling bond state, which causes an increase in D^0 states and promotes recombination [56] (2) Bond breaking-SJT model [41], suggests that the energy dissipated due to recombination of an electron-hole pair leads to breakage of weak Si-Si bonds and consequently increased density of midgap defect density[14]; (3) H Collision model [57] suggests that recombination of photogenerated carriers removes H from Si-H bonds creating concentration of Si

dangling-bond defects significantly [57]. When two free H atoms combine together to form a metastable two-H, the two dangling bonds from which H is emitted also become metastable. It is seen that during light soaking, defect density typically increases by an order from 10^{16} to about 10^{17} cm^{-3} [58]. This has been verified by Staebler and Wronski, who have also found revival of device quality being achieved by annealing at 180°C [14]. Other theories explaining this phenomenon exist as well. Some studies have identified the metastability in a-Si:H as arising from the breaking of weak silicon bonds [59], accompanied by structural rearrangements in the network, that can account for electron-spin resonance data, defect kinetics [60], charged metastable defects and hysteretic defect annealing [61], in contrast to the H-collision model [62] that has been proposed to explain metastability through the rupture of Si-H, followed by H-motion, leading to H-induced complexes in the network [62][63]. It has been recognized that H motion can occur by rupture and formation of silicon bonds [64] in the amorphous network, and the role of H has been implicated as the origin of metastability. Local H-motion and flipping of SiH bonds also leads to a metastable state that can account for infrared absorption changes on light soaking [65], in contrast to metastable changes in H-bonding where H bonds to weak silicon bonds.

For a-Si solar cells, clearly mid-gap defects created photo-generation are detrimental for the solar cell as they act as electron and hole recombination centers thereby adversely affecting their lifetime. It has also been seen to reduce the electric field in the middle region of the i-layer, which reduces the field assisted drift length or range and thus adversely affecting the collection of the carriers in i-layer [14].

With the target of improving stability of A-Si, several approaches have been tried, which includes the development of new fabrication materials, techniques and solar cell device structure. The new deposition methods that have been successful so far improving stability include remote ECR growth [66][67], hot wire growth [68], multichamber systems [69]. Dalal et al. reported that compared to the glow

discharge techniques, ECR process does a better job in improving A-Si:H solar cell stability [67].

It has been shown by our group that the stability of graded bandgap I layer structure solar cell is far superior when compared to that of a-Si:H solar cell with no grading [70]. Other approaches towards improving the stability of a-Si:H solar cells include use of “blocking/insulator layers, grading or P+ multilayered, i/n interface grading, tailoring of the i-layer”[13] [71], and tandem solar cells[72]. Researchers have extensively studied various deposition materials to improve stability - High Hydrogen dilution [73], He-dilution [74], deuterium dilution [75], and SiF₄ or SiH₂Cl₂ [76] have been successful in meeting this goal.

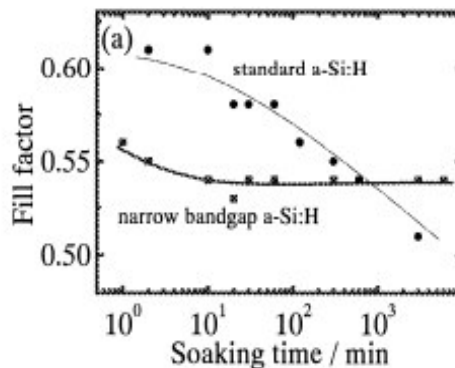


Figure 1.8 Effect of light soaking on CA vs NON CA [77]

However, chemical annealing so far has turned out to be a very attractive method for improving material stability. The basic objective of chemical annealing is to cause sufficient ion bombardment so as to remove loosely Si-H bonds, which are very vulnerable under light soaking and give rise to dangling bonds easily. Again, since the Hydrogen content is reduced, it allows us to reduce bandgap as well. The success of chemical annealing in improving stability has been shown by Shimizu et al [77], when they compared the Stability of p-i-n solar cell based on Ar CA was with standard a-Si:H solar cell fabricated from SiH₄ without H₂ dilution. Measurement found that in the beginning the standard solar cell has a higher FF, but after a light soaking of ~700 minutes, the FF of the standard one drops below that of

the CA one [77]. However, the FF of CA devices was low, ~55% range, implying high defect density.

So, it allows us to obtain low bandgap material which is less susceptible to light induced degradation. Thus, chemical annealing helps us in improving stability of material.

(b) *Past Amorphous SiGe research*

Extensive research has been done in the area of A-SiGe films as well as devices. It is well known that a-SiGe is more defective than a-Si.

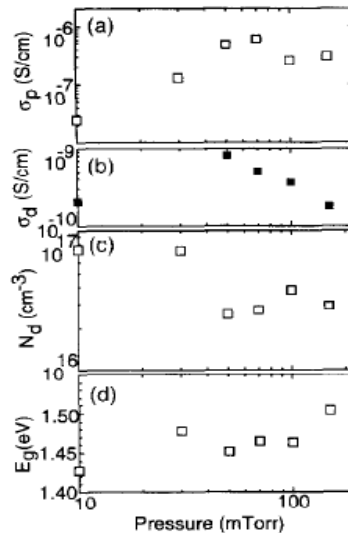


Figure 1.9 Effect of pressure on various parameters [78]

The importance of H₂ dilution has been shown by lot of groups. Ganguly et al [78] has shown that hydrogen-dilution technique can be applied to improve the quality of a-SiGe:H down to < 1.4eV . This method has played an important role in development of high quality a-SiGe:H layers in stable, triple junction solar cells by facilitating gas phase reaction with unwanted Germane-related higher order radicals thus preventing their contribution to film growth and hence improving the quality of a-SiGe:H. Detailed study of plasma chemistry revealed the fact that germane is strongly depleted when added to Silane and discharged at usual powers. The group also did an experiment with varying pressure to see the affect of pressure on material properties.

As we can see from Figure 1.10, photoconductivity increases and the defect density decreases as the pressure increases. Not much variation is however seen in the dark conductivity and optical band gap. At pressures above 50 m Torr the photoconductivity and the defect density saturate are seen to saturate [78].

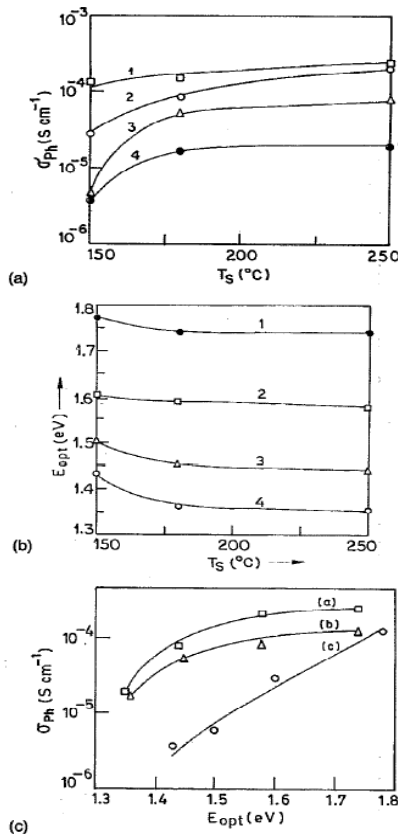


Figure 1.10 (a) Photoconductivities of the various films deposited as function of Growth temperature, for different dilution of GeH_4 ; Curves 1, 2, 3, and 4 are flow rates of 0%, 6%, 20%, and 30%, respectively of GeH_4 . (b) Changing optical band gaps vs substrate temperature for 1, 2, 3 & 4 (c) Varying Photoconductivity vs optical band gaps for a-SiGe -samples corresponding to (a) and (b). a, b, and c correspond to substrate Temperatures of 250, 180, and 150 C respectively [69].

Another work by Swati Ray et al [79] has shown the effect of various deposition conditions such as low flow rate, high Hydrogen dilution, use of He, He/H ratio to see its effect. The most prominent effect studied by her group is the effect of lowering temperature. If we reduce temp below 250C, then voids are formed because mobility of heavy GeH_3 is adversely affected. On the other hand too high temp, will lead to weakening of Ge-H bond and also lead to very poor quality material. The data presented

by the group leads us to believe that deterioration of film qualities due to decrease of substrate temperature can be checked if low flow rate of source gases and hydrogen/helium dilution are used to deposit the film.

Yet another work by Swati Ray et al [80] highlights the importance of Helium dilution. As seen in Figure below, photoconductivity for curve 1 goes up by 2 orders from 8×10^{-7} to about 4×10^{-5} S cm with the increase of R defined as the flow rate of diluent gas (He or H₂)/flow rate of source gas mixture (SiH₄+GeH₄) from 0 to 2. Beyond R = 8, σ_{ph} decreases. Initial increase of photoconductivity with R as seen in curve 1 is not observed for hydrogen dilution case. Curve 2 (hydrogen dilution case) shows that σ_{ph} increases with R from 0 to 10 and after that σ_{ph} decreases. $\sigma_{ph}/\sigma_{dark}$ versus R plots follow the same trend of σ_{ph} versus R.

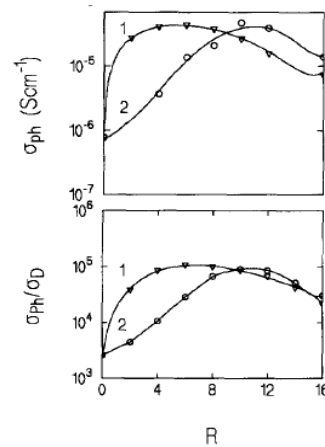


Figure 1.11 Study of change in deposition rate, photoconductivity and dark conductivity with R. Curve 1 and 2 correspond to helium and hydrogen dilution, respectively [80].

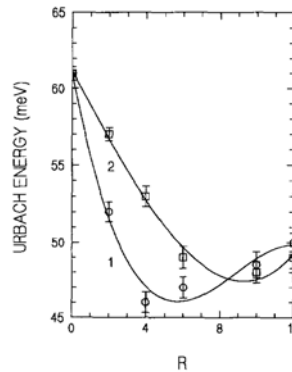


Figure 1.12 Study of change in Urbach energy with R. Curve 1 and 2 correspond to helium and hydrogen dilution, respectively [80].

The important conclusions drawn by the group are:-

(i) With the increase in hydrogen dilution, concentration of metastable hydrogen species is enhanced which are responsible for increased germane dissociation for the same germane flow rate. As a result, germanium radical flux towards the film being grown is enhanced facilitating enhanced germanium incorporation in the film.

(ii) Higher deposition rate of helium diluted a-SiGe films can be said to be because the helium atoms provide more energy and momentum to the growth inducing radicals as compared to equal amount of hydrogen which results in higher growth rate by increasing total flux of radicals towards the substrate. It has also been observed that highly energetic helium atoms can supply more energy to the growing surface directly by a physical process unlike H₂. Smaller dilution of Helium can lead to same growth rate as a Higher Hydrogen dilution, without adversely affecting film quality as revealed by the optimized photoconductivity and dark conductivity.

(iii) Large concentrations of diluted gas (compared to growth inducing gas) reduce the concentration of Si and Ge related plasma precursors and homogenizes it, which plays an important role in reducing defect density. Hydrogen dilution does a very good job at it - the defect density is reduced from $\sim 10^{17}$ to $10^{16} \text{ cm}^{-3} \text{ eV}^{-1}$ for an optical gap 1.5 eV, but it suffers from lower growth rate. On the other hand, He gas dilution enhances the defect density of the materials, due to the greater ion bombardment at the surface of the films. However, this work [80] shows that optimum helium dilution under suitable deposition conditions can reduce the defect density and E_{urv} to the about of $10^{15} \text{ cm}^{-3} \text{ eV}^{-1}$ and 46 meV, respectively, which is comparable to that for hydrogen diluted a-SiGe:H films. So using inert gas dilution, and proper optimization, high quality a-SiGe:H material can be produced at high deposition rate.

Key results obtained by the group using He dilution are summarized below -

- (i) Defect density of $6.72 * 10^{15} \text{ cm}^{-3} \text{ eV}^{-1}$
- (ii) Urbach energy of $46 \pm 1.5 \text{ meV}$
- (iii) Band gap of 1.5 eV.

Sanyo also did extensive research in this area [50]. Owing to the superior properties of VHF- PECVD, they used it extensively for their research. The pressure was 150mT and deposition took place at 230C. The deposition rate was however not that fast- just 1 to 2 A/s. The Hydrogen content was comparable to that obtained by Guha et al – around 10%. Urbach energy was however in excess of 50 meV. Photo conductivity / dark conductivity ratio was about $6 \cdot 10^4$. They managed to fabricate tandem (a-Si/a-SiGe) solar cells with efficiency in excess of 9%.

(I) Work done by our group

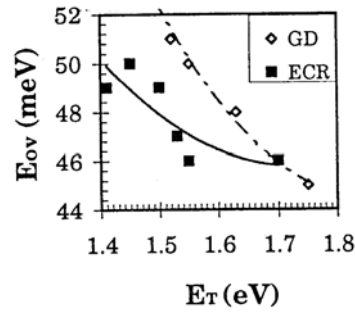


Figure 1.13 Urbach energy of ECR fabricated film compared with glow discharge generated films [81]

Extensive work in the area of A-SiGe has been done by our group as well in the area of A-SiGe. Kaushal et al [81] had made good quality a-SiGe using ECR techniques. The films were grown using a remote ECR low pressure plasma comprising of Helium. The He ions and radicals stream towards the substrate, and react with SiH_4 and GeH_4 to produce films.

Typical dilution ratio of Helium to growth inducing gases like Silane and Germane was 15:1. and the growth rates maintained between 1-1.5 A/sec. The films were grown at temperatures of 350 C, and pressure of 10 mT.

It was shown that ECR fabricated films had superior properties as compared to glow discharge generated films.

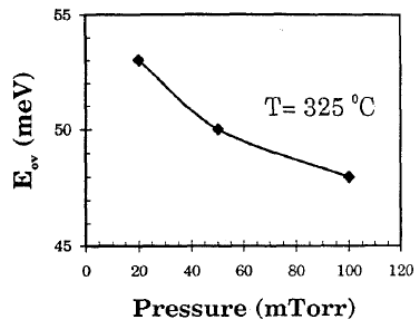


Figure 1.14 Effect of pressure on quality of the material [81]

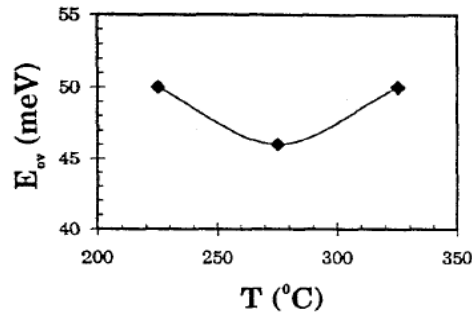


Figure 1.15 Effect of temp on Urbach energy [81]

It was observed that the improvement in the ECR fabricated film is a direct result of higher ion bombardment during growth. The Figures above some of the above parameters studied and it corroborates nicely with the current research. It is noteworthy that Urbach energy is lowest for about 275C and it increases with either increase or decrease the temp. Thus good quality A-SiGe can be grown only at that temperature; if we deviate from it then we will suffer as far device quality is concerned [81].

A detailed study on the effect of Ion bombardment on A-SiGe quality had been done by Matthew Ring [82]. He and other research groups [83], [84] suggested that although ion bombardment is beneficial to the deposition of amorphous semiconductors, as increased ion bombardment energy improves the material to a certain extent, excess of it can however harm material property. In this regard, it is much like substrate temperature. In the high ion bombardment conditions used in rf-PECVD reactors, Ring and other researchers observed, created better microstructure at low substrate temperatures, and enhanced photoconductivity in a-SiGe:H alloys [85]. The effect of very high ion bombardment was seen studied for A-SiGe[86],

wherein while on one hand ,lower ion energies caused significant improvements in material properties including photoconductivity, very high ion energies (Ar ions) on the other hand led to fabrication of materials having very high midgap defect states and Urbach energies [85].

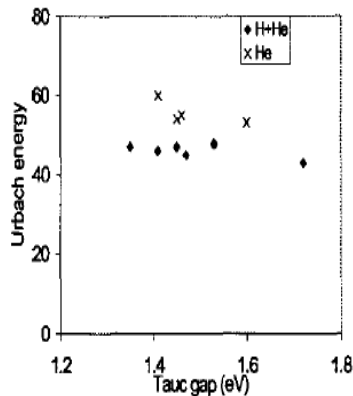


Figure 1.16 Properties of He dilution vs He and H dilution films [87]

In another work done by Yong Liu et al [87] the importance of inert gases and their advantages over Hydrogen dilution is discussed. One of the principal disadvantages of H dilution is however the lowering of the growth rate. As indicated by Yong Liu et al [87], high hydrogen dilution leads to low growth rates, typically – 1Å/sec. To facilitate higher growth rate of a-(Si,Ge):H devices, without adversely affecting material quality is a very desirable solar cell material attribute. It was shown that this can be successfully done in an ECR plasma deposition using a combination of He and H₂ dilution. The reason He does the job very well is that is the same as discussed by Swati Ray group [80] - the gases are dissociated more efficiently and more efficient ion bombardment of the surface is facilitated, allowing for a easier movement of Germyl radical on the surface. It is our proposal that Ar being heavier than H, will do a better job at providing ion bombardment. Hydrogen on the other hand improves material quality by etching off weakly bonded H atoms replacing it with densely packed microstructure.

Other major contribution has been optimization of device structure which has been discussed in details in subsequent chapter.

1.5 Outline of Research work

As we can see that although the principle of chemical annealing has been investigated and its success in reducing bandgap and improving light induced stability been demonstrated , so far good quality low bandgap A-Si / a-SiGe material is yet to be fabricated. The methodology adopted by us is as follows:-

1. Investigate the parameters affecting bandgap- growth per cycle, Ion bombardment, which can be varied by varying pressure).
2. Investigate the effect of ion bombardment on device quality- pressure
3. Confirm drop in bandgap through various film and device measurement.
4. Investigate the relationship between bandgap and Hydrogen content for CA and NON CA devices
5. Investigate material properties for devices and films – namely electron and hole mobility lifetime product, Urbach energy, light and dark conductivity etc
6. Adopt the successful techniques for A-Si to A-SiGe
7. Perform the aforementioned set of investigations for A-SiGe

CHAPTER 2 RESEARCH METHODOLOGY

In this chapter, we start with the detailed discussion of the solar cell structure used for our experiments. The basic structure of solar cell has remained the same for all solar cells (p-i-n) used in our research, the only variation being in the growth parameters used for chemical annealing. Separate I layer structure used for A-SiGe solar cells along with fabrication technique used namely PECVD, ITO sputtering has been discussed in details.

2.1 Design of Solar cell structure

(a) *A-Si solar cell design*

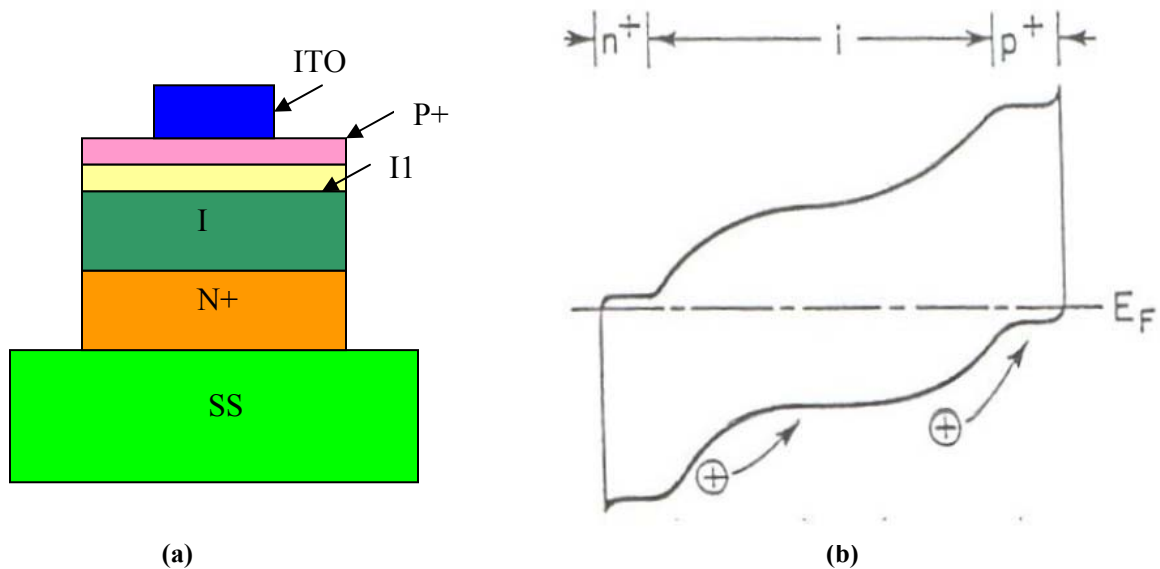


Figure 2.1 (a) Structure of a typical a-Si solar cells (b) band diagram of a-Si solar cells [13]

The structure of the device used in this research is shown in Fig. 2.1(a). The devices are fabricated on stainless steel substrates. First, an N + layer comprising of an a- Si:H layer doped with phosphorus is grown (it can be about 200-300 nm thick).

Next, the I layer is deposited, for a-Si:H solar cell in the presence of Hydrogen , Silane (and /or Germane for A-SiGe) and Argon .Trimethyl Borane (TMB) is used to compensating for oxygen contamination present in the reactor. The typical I layer thickness is 200-300 nm. Thicker I layer (> 500 nm) is fabricated if hole mobility – lifetime product is to be measured .The I layer is followed by a i_1 buffer layer of graded gap a-(Si ,C), which provides the bandgap matching between I and p^+ layer, and prevents

B diffusion from P+. The i1 buffer layer is then followed by a thin (~20nm) a-(Si,C) p layer- which acts as a window layer and an ITO contact (70 nm) on top.

(b) *A-SiGe I layer design*

In case of A-SiGe solar cells , there is no variation as far as P+ , N+ or I1 is concerned, however taking into consideration the poor quality of the A-SiGe it is essential to have a sophisticated graded I layer structure for having good quality solar cells.

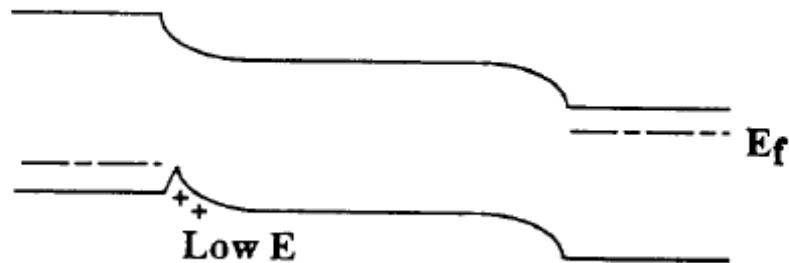


Figure 2.2 Band diagram of a hole trap [89]

It has been shown by our group before that typical bandgap design of Guha et al [88] can lead to problems in device quality. The idea behind the graded band gap structure is to help in hole collection. So the design initially consists of a graded buffer layer between p and I or in other words a-Si:H going to a-(Si,Ge):H. Thereafter, the grading is reversed to facilitate a “field assist for holes” [89], increasing the bandgap as we head towards the n layer. However, work done by our group has proved that this design is not desirable. It is better if P+ (a-Si,C) layer should be succeeded by a buffer layer , whose bandgap varies smoothly from P+ to a-(Si,Ge):H[89] , otherwise it can facilitate hole trapping at either the p-buffer or buffer-I interfaces as exhibited by the band diagram of the cell under forward bias in Figure 2.2, where it is shown how a hole can be trapped due to an abrupt hole affinity mismatch in the valence band ,which is commonly seen between different alloys like a-(Si,C):H and a-Si:H[89]

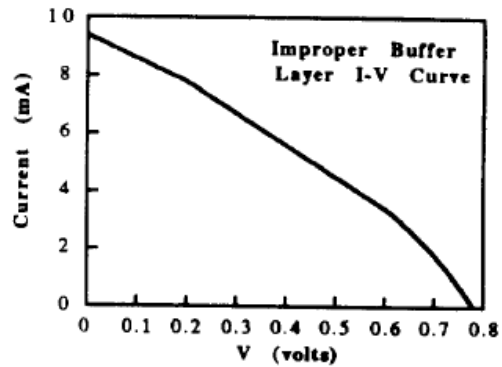


Figure 2.3 IV curve of a device with improper buffer layer [89]

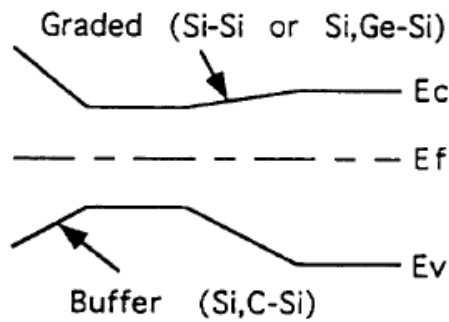


Figure 2.4 Band diagram of the a-SiGe I layer device followed by our group [89]

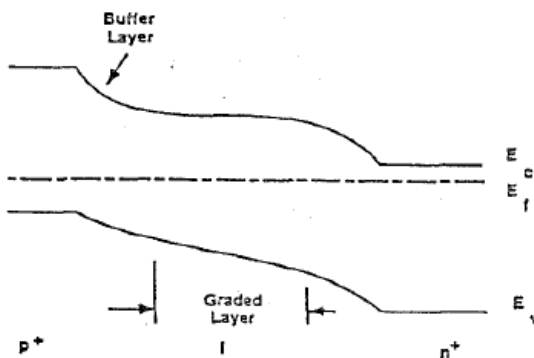


Figure 2.5 Band diagram of the complete PIN a-SiGe device followed by our group [90]

The band diagram shown above is the one that leads to high quality solar cell devices fabricated by our group. Consequently, this is the one followed in my research.

A major problem with graded gaps is that with increasing Ge content, both conduction and valence bands may shift relative to the bands in Si due to which we may have a band

structure in which while holes will receive a field assist, while electrons will face a field retardation. To overcome this problem, a graded ppm TMB doping of the I layer is carried out while bandgap is being graded. This on one hand decreased the retarding field for electrons due to the bandgap grading, and on the other hand created an additional electric field aiding hole collection [91]. In earlier work by our group [91], it has been observed addition of ppm B grading improves both the voltage and the fill factor significantly.

Before proceeding on to what growth parameters we need to optimize for successful chemical annealing, we need a sound understanding of growth chemistry, which will allow us to appreciate better the ill-effects of SiH_2 and how chemical annealing helps us in eliminating it.

2.2 Growth mechanism of chemical annealing

(a) Growth chemistry for A-Si chemical annealing

Earlier on, the model for a-Si:H growth called MGP model had been proposed by A Matsuda [92], Perrin [93] and Gallagher [94], as per which the surface diffusion of radicals like SiH_3 controls the growth of a-Si:H -which first finds an open site, bonds to it, causes expulsion of H by breaking Si-H bonds and thereafter causes cross-linking of neighboring Si atoms. However, fallacy of this model was its inability to explain why Si-H bond should break from such a surface-bonded Silyl radical at typical growth temperatures, as given the high bond energy of the surface bonded radical ($\sim 2.5\text{eV}$), it should be very stable. The standard model also fails to answer questions such as why bombardment with H ions helps to improve the material, and why low-pressure growth improves the properties of a-(Si,Ge) [95]

An improvement over this model was proposed by Dalal et al [96] as per which a-Si:H growth proceeds through 3 steps. These steps are:

- (1) Removal of surface H;
- (2) Insertion of a SiH_3 radical into the open bonds &

(3) Removal of inter-atomic H and cross-linking of Si. The whole process is shown in Fig. 2.6 (a).

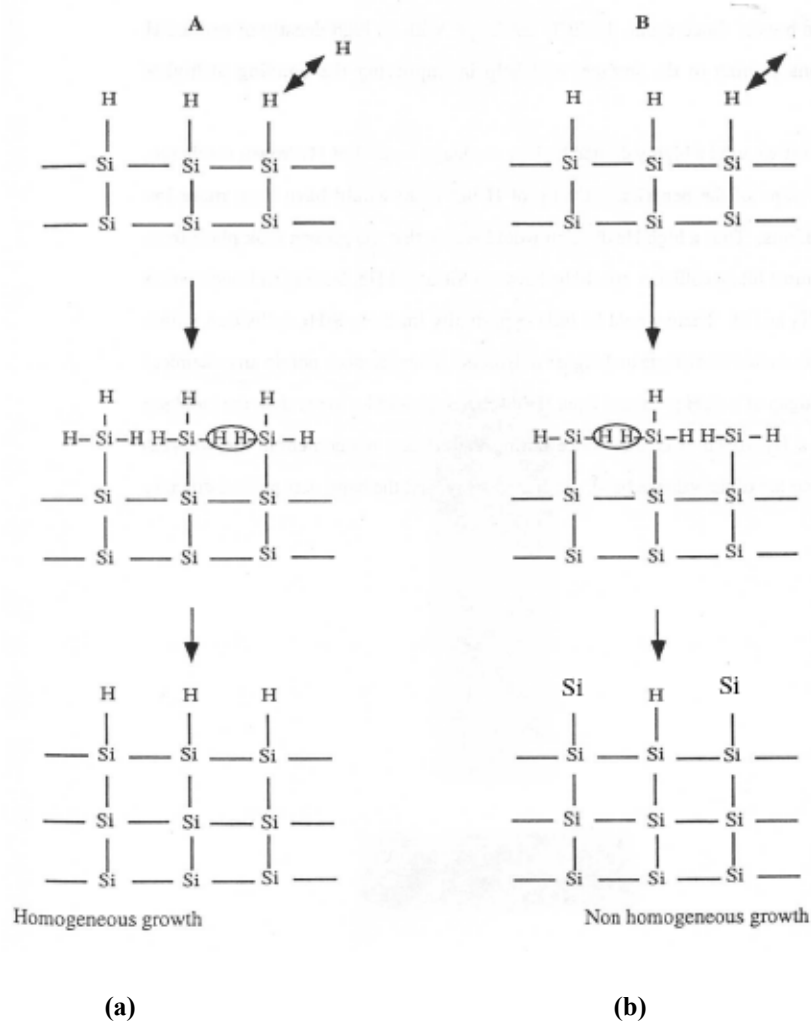
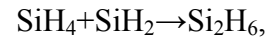


Figure 2.6 (a) Homogeneous growth chemistry of a-Si (b) III effect of SiH₂ [97]

The presence of H serves to promote the growth of a homogeneous material. High concentration of H radicals leads to homogenization of the growing surface by first bonding itself to the surface dangling bond, and thereafter creates an active site by removing the bonded Hydrogen which is true for all the sites irrespective of which radical (SiH₂ or SiH₃) was bonded at the site [97]. The following section explains in detail how is SiH₂ radical formed during fabrication process and more importantly, why is it undesirable to have them during growth process along with a detailed growth mechanism.

(I) Effects of SiH₂

Impact of high energy electrons (having energy above 9.47eV) with Silane molecules produces the short lived radicals like SiH₂, which in turn gives rise to higher-order Silane-related species in the following way:



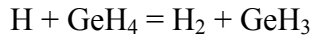
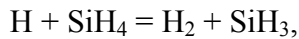
The effect of SiH₂ on the growth of a-Si:H can be shown in Fig. 2.6(b). For a homogeneous process shown in Figure 2.6(a), which occurs in the presence of SiH₃ radicals, H first removes the surface H leaving open sites, SiH₃ radicals then attach themselves to the open sites, followed by the breakage of adjacent Si-H bond by ion or thermal energy (H atoms release as a result form molecule to go to a lower energy state and is thus removed), and finally cross-linking of Si. A homogenous surface thus forms wherein every dangling bond has been passivated by H- which will facilitate the formation of high quality solar cell material. While in process B, Presence of both the SiH₃ and SiH₂ radicals promote the formation of dangling bonds. When a layer is to be grown on top of this layer, the dangling bonds can accept other radicals, while the passivated bond(s) cannot if the attached H is not removed and thus will be buried within the material [98].

Chemical annealing has been shown to remove the excess H content in the film during the deposition through ion bombardment. It essentially consists of growing a thin film, typically 7-15 Å thick, then subjecting it to ion bombardment, and then repeating it to obtain the desired thickness. During the ion treatment period, the highly energetic ions are supposed to break the weak Si-H bonds, which in turn reduces the micro-voids induced by the excess H and improves the stability of a-Si:H for future application. The most important aspect is that it can be used to alter

the bandgap of the material as it allows us to reduce the Hydrogen content of the material .

(b) Growth chemistry for a-SiGe and Importance of Hydrogen dilution

For the growth of a-(Si,Ge):H, the two primary precursors, Silane and Germane, dissociate at very different rates [81]. It is thus crucial that the chemical reaction are carried out such that extra energy be imparted to the surface to facilitate better movement of radicals, thus leading to superior film quality. Usage of high Hydrogen dilution can facilitate this by causing the following chemical reactions:-



Excess of H will promote the creation of Silyl and Germyl radicals causing a “homogeneous insertion reaction” [81].

Another potential problem is the varying Germyl and Silyl radicals mobilities on the surface. Ion bombardment, either with H or with an inert gases such as He, Ar is commonly used approach to tackle this problem, thus leading to better quality films. Highly diluted H plasmas, causes high ion bombardment energies and consequently to the growth of high quality a-(Si,Ge) films. Presence of high concentrations of H prevents the reactions formation of higher order radicals, which facilitates the formation of non homogeneous films. An interesting aspect of the growth chemistry deals with the relationship between bandgap and Ge content. It has been shown that the bandgap of a-(Si,Ge) films depends not only on the Ge content, but also on processes taking place during growth. Excess H etching during growth can lead to a widening of the gap, thereby requiring more Ge to achieve a given bandgap which implies degradation of film properties. To prevent this, H-induced etching during growth must be limited. An inert gas ion bombardment allows both increased surface mobility and reduced etching, thereby leading to a lower gap but not at the expense of material quality for a given Ge concentration [81]. This clearly is advantageous for us as far growing devices and films with chemical annealing, wherein we will grow material in the presence of inert gases.

2.3 Fabrication technique

(a) Sample preparation

All devices are deposited on 1.5 inch by 1.5 inch stainless steel. However, prior to deposition of device, it has to undergo a thorough standard cleaning procedure- which involves 3 steps :-

- (i) Acetone cleaning- This involves heating the SS in an boiling acetone bath and ensures all surface and organic contaminants are eliminated
- (ii) Cleaning in a boiling mixture of Ammonium Hydroxide and Hydrogen Peroxide (NH_4OH and H_2O_2)
- (iii) Ultrasonication with methanol solution

Thereafter they are stored in a methanol solution and blown with a Nitrogen blast prior to loading in the reactor, design of which will be discussed in the next part.

(b) Reactor design

The PECVD reactor used for fabrication of films and devices was a VHF PECVD shown in Figure 2.7 below. As can be seen that this reactor has a horizontal orientation, which means that the electrode that causes the plasma is parallel to the surface of the substrate and is at a 90 degree angle to the ground. The gas flow to the chamber is arranged such that it flows from behind the substrate holder. This arrangement enjoys the advantage that nothing falls into the vacuum pump lines, thereby protecting the rotary and turbo pump . Also, since the electrode and shutter is not aligned above the sample, it is unlikely that foreign particulates will fall on the substrate or electrode during a deposition. This explains the rational behind a top loading substrate holder (comprising of heating elements) being used in our setup [99].

Ideally, we would like to always keep the reactor at high vacuum and move the sample around through a series of interlocks as in a load lock system. This is not however necessary if care is taken to thoroughly purge out the chamber after loading in samples.

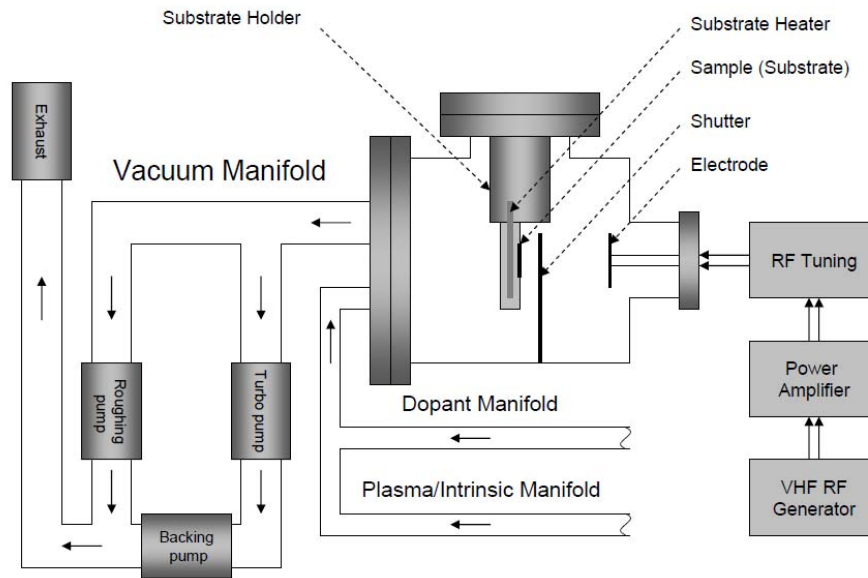


Figure 2.7 Design of VHF PECVD used in our research [99]

In our system after loading the samples, we first take the system down to a medium vacuum level of about 1 Torr using a rotary vane pump. Better known as a roughing pump due to the pressure region it works in, this pump can quickly bring the chamber from atmospheric pressure to medium vacuum levels. This pump is connected directly to the Chamber. But Roughing pump by itself is not enough since the film deposition requires ultra high vacuum so we make use of Turbo molecular pump, which can quickly bring pressures down to ultra high vacuum (base pressure of 10^{-7} torr) from medium vacuum. Not only that it maintains this pressure for several hours with negligible pressure deviation – which is crucial for our research. The turbo pump however cannot be exposed to atmospheric pressure exhaust pressure, it needs an intermediary rotary vane pump, also known as a Backing pump- which also removes all gases drawn in by the turbo pump thus protecting it [99].

For measuring the pressure and ensuring that pumps are operating as per expectation, a set of pressure measuring gauges are employed. A Pressure transducer can be used for measuring pressure beyond 1 mtorr to a maximum of 1 torr- this is used just after purging out the chamber after loading the sample in and also while performing film/ device

deposition using Plasma. However, for greater accuracy at high vacuum, Ion gauge is used – which allows us to detect any kind of chamber leakages.

In addition to the gas removal system, gas flows into the chamber is also an important aspect of the reactor. Gas cylinders storing hydrogen, helium, Silane, methane, TMB and Phosphine are the source of gases. Pressure is brought down from about 1000 psi higher to a sufficiently lower level depending on the gas. Thereafter, solid metal tubings transports gases to a set of Mass flow controllers (MFCs) which control how much gases reach the reactor depending on what gas flow has been set up by the user. Reactor gases are passed through three major gas lines- intrinsic line, plasma line, and dopant line gases. Needless to say, the dopant line is kept completely separate from intrinsic and plasma line as they can ruin the I layer due to cross contamination. However, the intrinsic and plasma lines are kept in series- we cannot switch on the intrinsic valve without switching on the plasma line. The plasma line only comprises of H₂ and Ar, while intrinsic line comprises of all other non dopant gases. MFC s placed next to the flow controller panel allow the user to regulate how much of each type of gas is to be flown. Besides this, we also have 2 other gas lines which supply (i) N₂ used during purging of chamber and (ii) O₂ /N₂ flow, which is used for initiating Oxygen plasma necessary for combating boron contamination due to Diborane [99].

For initiating plasma , 3-7 Watts of RF signal is applied to a 3 inch diameter electrode aligned opposite to the substrate, held on to a substrate holder. It is electrically insulated and is connected to a power amplifier by a coaxial cable. A signal generator is also connected to the power amplifier, which decides the frequency of the signal. In our reactor we make use of Very high frequencies (VHF) – the advantage of which is discussed in the next section [99].

The reactor also has a shutter which lies between substrate and electrode, ensuring no deposition while plasma is being ignited or being allowed to stabilize. There are two

separate thermocouples for measuring the temperature of the system. The heater automatically adjusts to hold a consistent temperature [99].

(I) Importance of VHF PECVD

Ion energy is very important parameter affecting growth of films / devices. In the 1930s J.K. Robertson showed that sputtering works better at high frequency discharge than a DC discharge. Ever since, there has been a lot of work done in High frequency discharges particularly for deposition of amorphous silicon.

Before understanding how VHF aids in amorphous silicon deposition, here is a brief overview of plasma conditions in our VHF PECVD system. Ours is a capacitively coupled plasma discharges. It consists of a chamber where plasma is obtained when the discharge is ignited between two electrodes. The plasma comprises of the glow space or the bulk and dark spaces known as the sheaths. In most system Plasma uses RF power at around 13.56 MHz, applied at one electrode while the other is generally grounded. It is seen that most of the voltage drops across the dark space due to presence of space charges (and thus following Gauss's theorem)[100]. However, the VHF (very high frequency) is preferred in our setup of PECVD as it possesses the following advantage:-

- (i) Lower ion energy- just enough to remove excess H, but not enough to damage lattice
- (ii) Higher ion flux density leading to higher deposition rate [100]
- (iii) More efficient power coupling leads to higher electron densities [100]
- (iv) Prevents plasma non uniformities like the skin effect and edge effect [100]

Electrons being lighter than ions have higher mobility than ions and are thus more easily collected on an electrode during the positive cycle, leading to depletion of electrons from dark spaces and an increase in glow space potential with respect to the electrodes. The potential acquired by the glow space is so large that during most

of the RF cycle no electrons can leave it, leading to what is better known as negative “self bias”. But on the other hand, the heavier positively charged ions, reach the electrode after many cycles which leads them to having a time averaged energy. So we can conclude that higher frequency not only leads to lower ion energy but also thinner sheaths [100].

Another advantage of VHF is the increased deposition rate. This is a consequence of increasing electron density with increasing frequency, as power is better coupled into the plasma at higher frequencies. The higher electron density leads to higher density of radicals and ions, thus increasing the deposition rate. So it is not surprising that increasing frequency from 13.56 Hz to about 48 Mhz (VHF range) can easily lead to a significant increase in growth rate [100].

(c) ITO Sputtering

The Magnetron sputtering system enables us to deposit a transparent conducting oxide namely Tin doped Indium oxide. A schematic of the apparatus used for sputtering is shown below. We now have capability of sputtering both by using DC and RF. RF sputtering is however preferred.

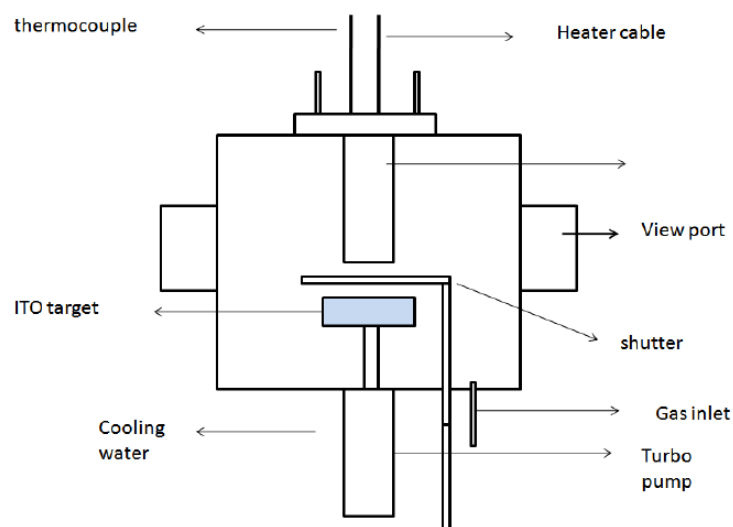


Figure 2.8 Schematic of sputter system [100]

Ito Calibration is done by depositing about 800 nm of film on pre cleaned glass substrate. The calibration procedure involves measuring transmission data as a function of wavelength and measuring sheet resistance of the film.

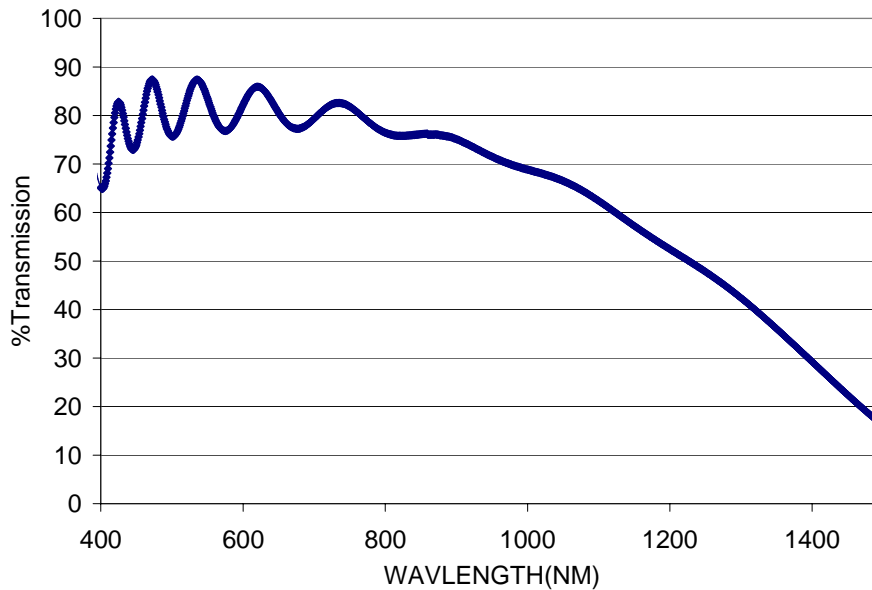


Figure 2.9 Transmission vs wavelength plot for ITO

Typical plot of Transmission vs wavelength for an optimized ITO is shown above – it can be seen that close to 600nm, the transmission comes close to about 90%. Furthermore, for high quality ITO, beside high transmission, low sheet resistance and resistivity is also an important criteria. Typically, for best quality ITO films, resistivity as low as $2.5 \times 10^{-4} \text{ S cm}^{-1}$ is found. Needless to say, low sheet resistance is desirable as it leads to lower series resistance in solar cells. In this regard, it will be worthwhile to mention, that depositing Al bus bars and annealing it at 200C for 30 minutes (for ensuring ohmic contacts) does help us in further lowering series resistance (by about 40%) and typically for a-Si/ a-SiGe solar cells it pushes up the FF by 4-5 % as well.

CHAPTER 3 CHARACTERIZATION

3.1 Device characterization

(a) Quantum Efficiency

External quantum efficiency (EQE) is given by the ratio of number of carriers collected to the number of incident photons per unit area, while internal quantum efficiency (IQE) is known as ratio of the number of carriers collected to the number of photons absorbed (after considering reflection losses). A monochromator is employed to shine light of different wavelengths on the sample. Due to higher absorption coefficient, shorter wavelengths get absorbed at a very shallow depth (approx. 100 nm), while the longer wavelengths penetrate deeper and generates carriers at the deep into the intrinsic layer [100]. The QE setup used in our lab is shown in Figure below.

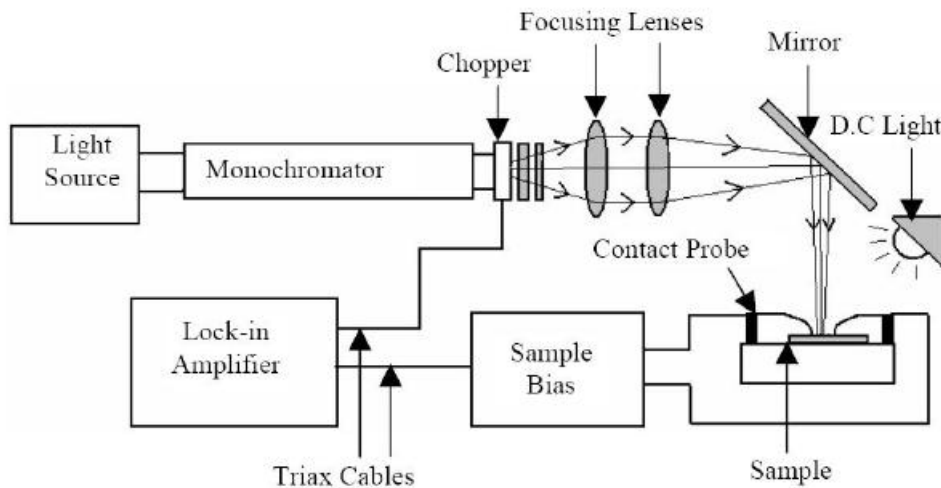


Figure 3.1 QE experimental Setup [100]

We employ the dual beam technique [100] - wherein DC light is shone on the samples so as to fill the midgap states with photogenerated carriers, and fix the quasi fermi levels. Light from a monochromatic source passes through a chopper rotating at a frequency of 13.5 Hz, which turns it into AC beam, and then focused on the sample using a couple of lenses and finally, reflected from a mirror onto the sample. The current generated from the sample is converted into a voltage signal, and fed into a phase lock amplifier (PLA), programmed to lock in on a frequency of 13.5 Hz. Thus the PLA eliminates noise due to

other electronic instruments and improves the sensitivity of the system [100]. Thus we vary wavelength from 400 nm to upto 1600 nm and record the voltage response .Filters are used at 700nm and 900nm to minimize noise from the “lower harmonics”[100]. A commercial photodiode, whose QE is already known is selected as the reference and its voltage response is recorded as a function of wavelength, just like we do for the device under test [100]. With the knowledge of these parameters, QE of the Device can be calculated using the following equation:-

$$QE_D = QE_{ref} \frac{A_{ref}}{A_D} * \frac{V_D}{V_{ref}} \dots\dots\dots 5$$

where A_{ref} and A_D refer to the area of the reference cell and Device under test and V_{ref} & V_D refer to the signal measured across the reference cell and Device.

(I) Absorption coefficient , Urbach energy and midgap defect density measurement using Quantum efficiency

The main focus of our research has been to observe the variation in absorption coefficient energy curves with change in various growth parameters. We have calculated Absorption coefficient (α) from QE data taken at a reverse bias of -1 V, which ensures that all the carriers generated are collected. Thus electric field is high enough to say that range (S_n) which is product of electric field (ϵ), mobility (μ) and carrier lifetime(τ) is pretty high. QE for a solar cell having I layer thickness t is given by the equation-

$$QE(\lambda, V) = \int_0^t \alpha(\lambda) \cdot e^{-\alpha x} \cdot e^{-\int_0^x \frac{1}{\mu \epsilon} (y) dy} \cdot dx \dots\dots\dots 6$$

For constant electric field, then the equation reduces to

$$QE(\lambda) = \frac{\alpha S_n}{1 + \alpha S_n} [1 - \exp(-\frac{t}{S_n} (1 + \alpha S_n))] \dots\dots\dots 7$$

Since range (given by S_n) is sufficiently high for high reverse bias, the equation reduces to

$$QE = (1 - \exp(-\alpha t)) \dots\dots\dots 8$$

which gives us

$$\alpha = -\text{Log}_e (1 - QE) / t \dots\dots\dots 9$$

However, this equation does not take into account reflection losses. If we take that into account equation 9 changes into

$$\alpha = -\text{Log}_e (1 - QE / (1 - R)) / t \dots\dots\dots 10$$

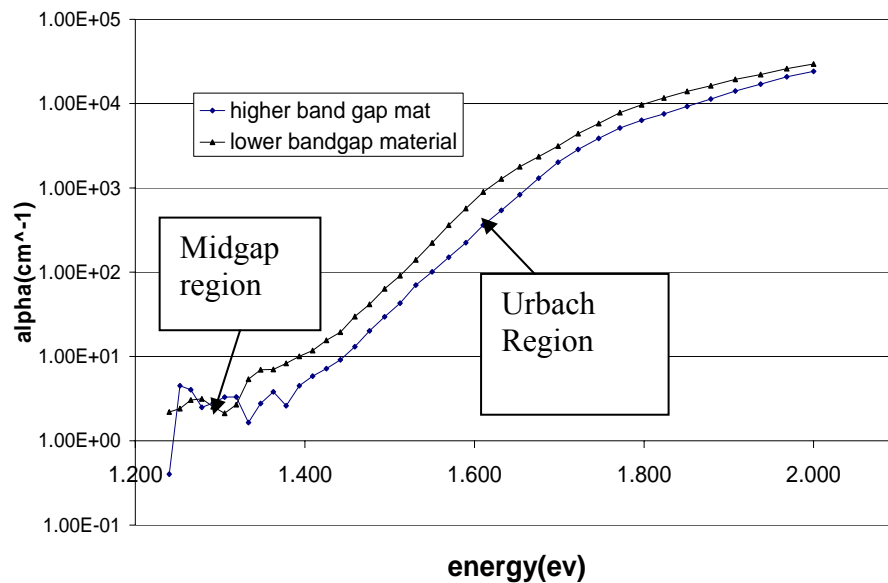


Figure 3.2 Lower vs higher bandgap material absorption energy curve

This relationship neglects the absorption due to p+ (which is low as p+ is extremely thin). For the comparison of bandgap between two materials, we plot the absorption energy curve for the corresponding materials and the material whose absorption E curve is on the left is lower bandgap. A plot showing a higher bandgap and lower bandgap material is shown above. After we subtract the midgap absorption from absorption curve, Inverse of the slope of the curve gives us the Urbach energy, which is a measure of the quality of the film. The midgap region, where the absorption curve saturates gives us an idea of the defect density present in the material. In many literatures [101] it has been suggested that, the absorption

coefficient corresponding to the midgap region when multiplied with a calibration factor ($\sim 1 \cdot 10^{16}$) gives us the total midgap defect density present in the material. It has been observed that an increase in Urbach energy, E_{uv} , increases the midgap defect density, implying that E_{uv} is closely related to the midgap defect density

(II) QE Ratio

A very important parameter used in analyzing solar cell quality from QE curve is QE ratio. The quality of a solar cell is recognized from not only the QE plot but also the QE ratio between the Normalized QE at 0 bias and a given positive bias (+.5V is commonly selected for most analysis.)

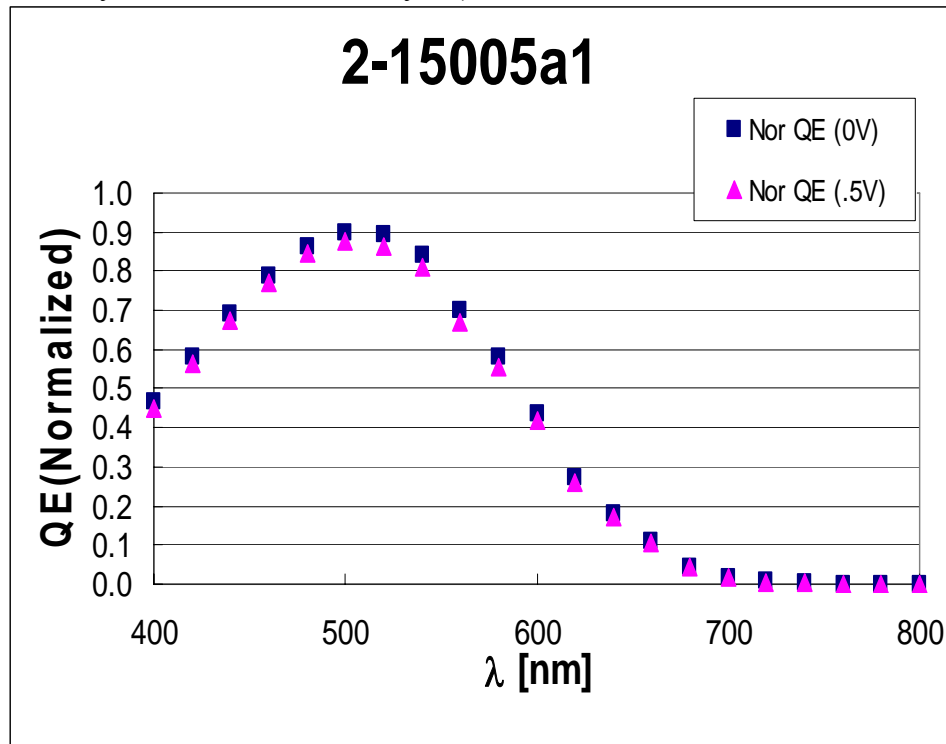


Figure 3.3 Norm QE plot at 0 bias and +.5 bias for various wavelengths for a high quality A-Si device (FF~ 65%)

It can be seen that QE ratio data can be dissected into 3 main regions- (a) close to p-I interface region (corresponding to lower wavelength~ 400 nm) (b) Bulk I layer (~ 600 nm) and (c) closer to n-I interface(~ 800 nm), as shown in the Figure below.

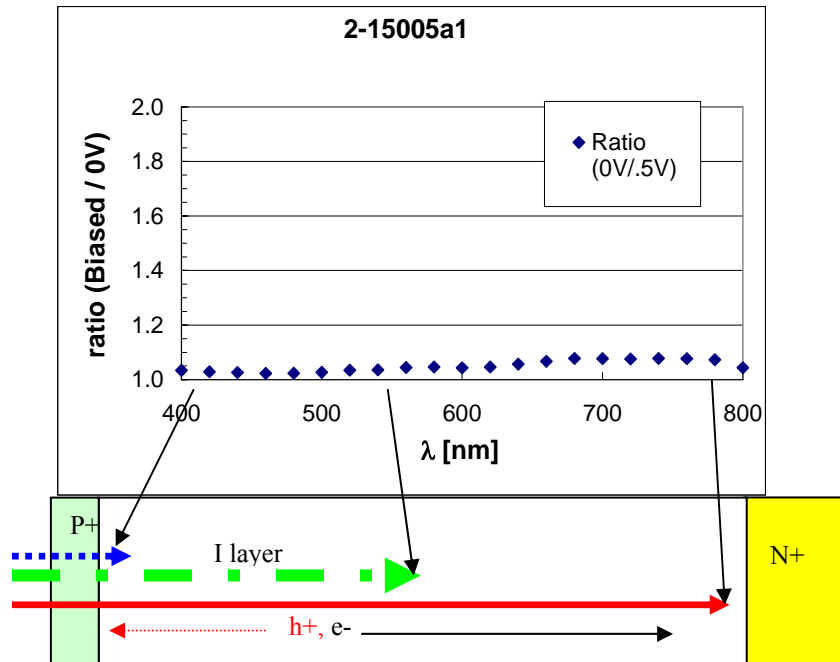


Figure 3.4 QE ratio plot for various wavelengths for a high quality A-Si device (FF~ 65%)

It is known that in a solar cell, minority carrier collection is of top concern as they recombine faster and thus decide the quality of the material. Due to non uniform distribution of traps, it is seen that holes are always the minority carriers in A-Si and A-SiGe. Another point to be noted is that the reason positive bias is applied to reduce the built in electric field and see how collection of minority carriers are affected- for a given wavelength, in a good quality material with or without bias minority carrier collection should not be affected. With these points in mind if the QE ratio plot is seen, it can be seen that at lower wavelength(~ 400 nm), QE ratio will be close to 1 even if quality of cell may not be that good because the holes will be easily collected being close to p-I interface (unless the material has become p type due to excessive TMB flow, in which case electrons will become the minority carriers). The real test of the quality of material is when the holes are generated far away from p-I interface, which happens for higher wavelengths ie 600 nm or above. If the material is of high quality, then it will be seen that QE ratio will be close to 1 even for wavelengths beyond 600 nm, otherwise it will climb up steadily with increasing wavelength.

(III) Hole $\mu\tau$ product

The importance of minority carrier has been highlighted in the previous section. An important property of the minority carrier, which is hole for A-Si and A-SiGe is to know their mobility lifetime product, indicated by $\mu\tau$. This parameter plays a decisive role in determining quality of solar cell. Larger is this parameter, easier it will be for the holes to drift into the I layer without recombining and be ultimately collected at the p+. Mathematically, it has been seen that QE is dependent on the hole range, $\mu\tau\alpha$, as per equation 6. With the knowledge of QE values, absorption coefficient and the electric field, the $\mu\tau$ product can be obtained from equation 6.

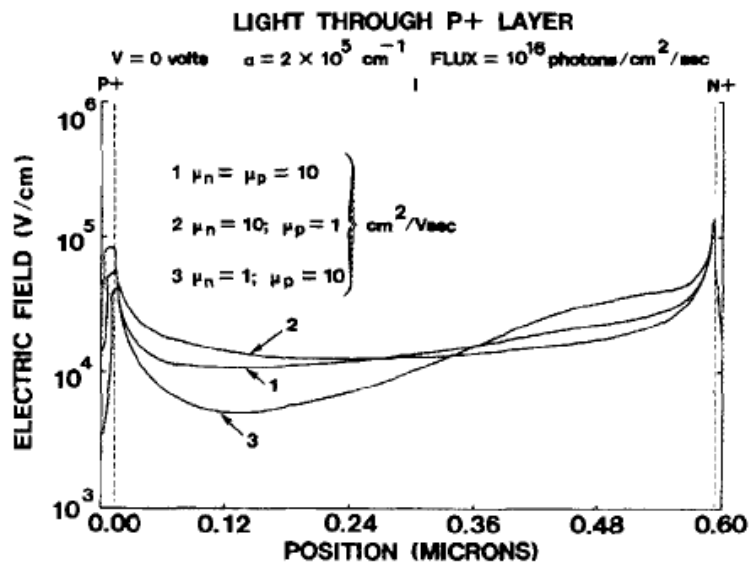


Figure 3.5 Simulated electric field profiles in p-i-n diode for varying values of the carrier band mobilities [102].

Various techniques exist currently for obtaining electric field profile. Hack and Shur utilized a computational model for profiling the electric field [102], which included an interface boundary condition, and called for defect density profile being numerically integrated over a range of energy [102]. The output is the electric field profile as a function of distance. As shown in the Figure above, the electric field is high near the interface and reduces quickly as we head towards middle. Since the electric field in the bulk of the I-layer plays a major role in carrier collection, Greg

Baldwin used a simplified model, so that no boundary condition is required, and electric field can be directly calculated from voltage equation [103]. Figure 3.5 gives a simulated electrical field profiles in p-i-n diode based on Hack and Shur model [102]. In spite of the accuracy of these models, they are not suitable for $\mu\tau$ product calculation, and since no direct relationship exists between E field and distance, the calculation can become very arduous task. So to simplify matters, Dalal and Alvarez [104] used a uniform electric field approximation by dividing the sum of the applied and built in voltage by the thickness of i-layer /2. Since most of the electric field drop happens in the p-I and n-I interface it is not incorrect to say that the potential drop in most of I layer is about $\frac{1}{2}$ Voc. This approximation has been successfully used by others including Crandall et al [105].

The measurement technique adopted is fairly simple and easy. For a given device (made .5 micron or thicker in thickness for greater accuracy), QE vs applied bias for several wavelengths is measured. It is observed that with increasing reverse bias, the QE increases, while under forward bias, it is seen to decrease. With the assumption that $\mu\tau$ is unaffected by bias voltage and wavelength (which is not hypothetical), it can be said that change in QE is coming from change in applied electric field. Given a wavelength, under different bias, the data set of measured QE vs bias is thus obtained. Now, by inserting the different applied electric field (due to varying applied bias) into equation 6, we can obtain the data set of simulated QE vs bias if the $\mu\tau$ is known. With some trial and error, a suitable $\mu\tau$ value can be chosen to ensure that the measured data matches with the simulated data, and this value is reported as the right value. In this measurement, long wavelengths lying between 600nm-800nm should be selected. As mentioned in the previous sections, for the short wavelength, most of the photons are absorbed near the p-i interface, and hence no information of the bulk I layer is obtained. It is crucial to note that the $\mu\tau$ product to be reported must simultaneously satisfy the simulated vs measured QE data for the three wavelengths selected in our analysis- 600, 680 and 760 nm.

(b) Light Current Voltage measurement

The standard way of gauging the solar cell performance is to observe the current voltage characteristics under light illumination. A typical current-voltage current of a solar cell under AM 1.5 light intensity is shown in Figure 3.6.

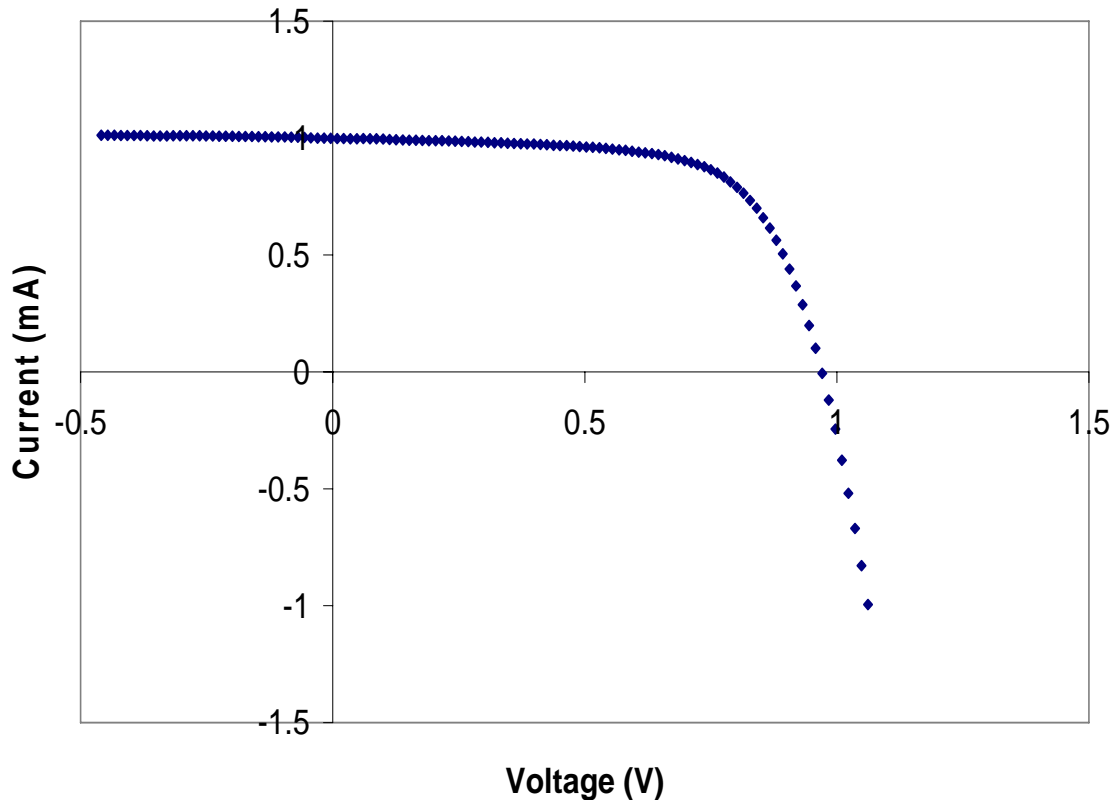


Figure 3.6 Typical IV curve for a solar cell .

The equivalent circuit shown in Figure 1.2 leads to the following relationship :-

$$J(V) = J_s \left[e^{\frac{qV}{AKT}} - 1 \right] - J_L(V) \quad \dots\dots\dots 11$$

where $J(V)$ is the current J at voltage V , J_s is the reverse saturation current, q is the charge of an electron, A is the diode ideality factor, K is Boltzman's constant, T is the temperature and J_L is the light generated current .

The first quantity of interest is the short circuit current J_{sc} , which is the current of the cell under illumination for short circuit condition.

The second quantity of interest is the open-circuit voltage V_{oc} , which can happen when R_L is infinite or in other words, open circuit. Mathematically V_{oc} is given by

$$V_{oc} = \frac{AKT}{q} \ln\left(\frac{J_L}{J_s} + 1\right) \quad \dots\dots\dots 12$$

The third parameter is fill factor (FF), which is nothing else but the ratio between the existing optimum output power P_{max} ($= I_m V_m$) and the ideal optimum output power P ($= I_{sc} V_{oc}$). Mathematically it is given by,

$$FF = \frac{V_m I_m}{(I_{sc} V_{oc})} \quad \dots\dots\dots 13$$

Clearly higher FF is desirable as it indicates high quality solar cell material and optimum solar cell design – loss of light generated carriers in I layers and interfaces have been minimized and ohmic losses have been reduced as well. A typical high quality A-Si solar cell has FF of 65-70%

If V_{oc} , I_{sc} , and FF is known, the solar cell efficiency η can be calculated. It is given by the ratio of maximum power that can be obtained from the cell to the total power shone on the sample (typically 100 mW/cm^2 for AM 1.5 spectrum). The equation is

$$\eta = \frac{FF \cdot V_{oc} \cdot I_{sc}}{P_{in}} \quad \dots\dots\dots 14$$

where P_{in} is the total incident power of the photons.

(c) Defect density measurement from CV

We know that Capacitance is related to Applied Voltage V_{ap} for PN junction as

$$C/A = \frac{1}{2} [2q\epsilon / (V_0 + V_{ap}) N_{scr}]^{1/2} \quad \dots\dots\dots 15$$

It is possible to calculate charge in the region, N_{scr} by plotting $(A/C)^2$ vs Voltage and determining the slope of two regions as shown in the Figure .

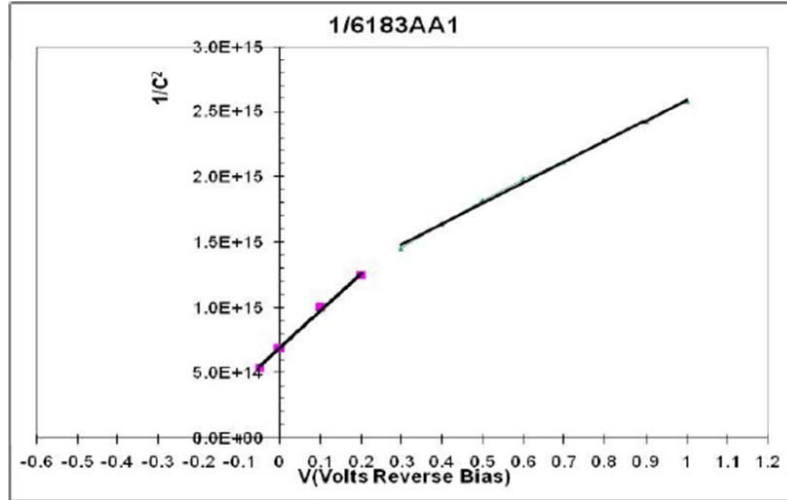


Figure 3.7 Sample Capacitance vs voltage measurement [106]

It has been shown that, assuming homogenous trap densities, the measured defect density would change as a function of position. When measuring traps near the junction, we observe the tail states near the conduction band or valence band. On the other hand, at higher reverse bias, we get to measure deeper traps. Measurements were made at low frequencies and high temperatures to facilitate measurement of deep traps [106].

(d) Defect density measurement from C-F measurement

Capacitance - frequency measurements facilitate a detailed study of defect profiles, as shown by Walter [107]. So as part of our research, we measured C vs freq at low temperature (room temperature) and at high temperature (~ 150C) and Calculated N_t using the following equation

$$N_T(E_{\omega}) = - \frac{U_d^2}{w[qU_d - (E_{fpo} - E_{\omega})]} \frac{dC}{d\omega} \frac{1}{kT} \dots\dots\dots 16$$

where U_d is the built in voltage, w is the width of the i-layer, k is Boltzmann's constant and T is the temperature in degrees Kelvin. E_{ω} is the energy at which traps can respond to a given frequency. Once we obtain Density of states as a function of Trap level with respect to conduction band and obtain the total defect density by fitting a Gaussian and then calculating the area of complete Gaussian distribution [106].

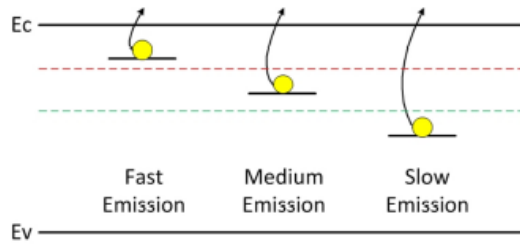


Figure 3.8 Traps closer to conduction or valence band emit electrons or holes much faster than that deep inside- basic principle of trap measurement using differential capacitance techniques. At high frequency measurements, traps above the red line, which emitting carriers very easily will be detected, while using the lower frequency we reach out to the traps below green line and thus detect both the fast emitting and medium emitting traps[106].

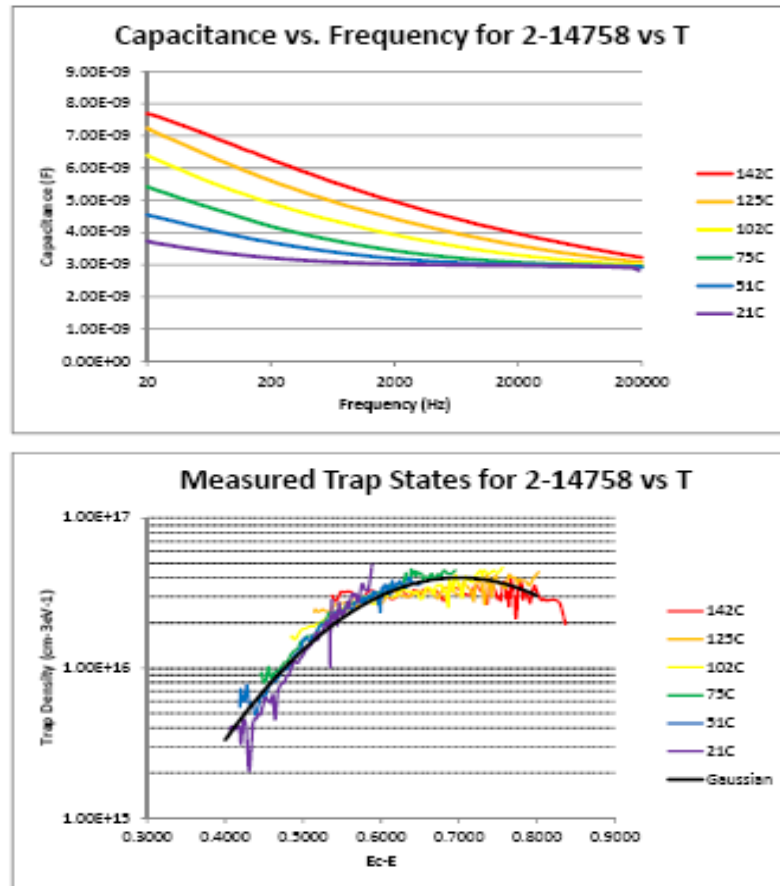


Figure3.9. The top graph is the variation of Capacitance vs Freq as a function of temp & frequency, while in the bottom, the calculated trap densities are fitted to a Gaussian profile [106]

3.2 Film characterization

(a) Thickness and absorption coefficient measurement

From the transmission vs. wavelength spectra, the interference pattern can be used to determine the thickness of the film by comparing the positions of adjacent peaks or valleys and using the equation given below.

$$t = \frac{\lambda_1 \lambda_2 \cdot m}{(\lambda_1 - \lambda_2) \cdot n} \quad \dots\dots\dots 17$$

Where n = refractive index of the material, m = 1/2 for adjacent peaks or valleys and 1/4 for peak to valley. Using the measured absorbance, reflection we can calculate absorption coefficient using the following relationship:-

$$\alpha(\lambda) = \frac{\ln(1 - R(\lambda)) + 2.303A(\lambda)}{t} \quad \dots\dots\dots 18$$

(b) Fourier-transform infrared spectroscopy measurement

Fourier-transform infrared spectroscopy is a useful measurement allowing us to analyze the microstructure, and the type of bonds present of materials. In our research, it is used here to determine the H content and the silicon-hydrogen bonding configurations. When photons in the infrared region having wavelengths around 4 to 40 μm are incident on a hydrogenated Silicon film, they may undergo absorption at the band features by phonons, free charge carriers or impurities, which results in rotational and vibration transitions of the molecules, which can be picked up through FTIR measurements. Double-side polished Si wafers are generally used for FTIR analysis, which has an advantage of being transparent in IR regime.

The most widely accepted method of calculating hydrogen content has been suggested by Brodsky, Cardona and Cuomo [108], as per which hydrogen content in a-Si:H is given by:-

$$N_H = A \int \frac{\alpha(\omega)}{\omega} d\omega \quad \dots\dots\dots 19$$

Where A is an experimentally determined constant $\sim 1.6 \cdot 10^{19} \text{ (cm}^{-1}\text{)}$, $\alpha(\omega)$ is the absorption coefficient at angular frequency ω . The integral extends over the whole 640 cm^{-1} absorption peak.

(c) *Raman spectroscopy*

Raman spectroscopy is a non destructive technique for determining the crystallinity of the material. It essentially involves shining a laser beam on the sample and analyzing the scattered beam obtained from the sample. Most of the scattered light has the same frequency as the incident light (known as Rayleigh scattering). However, another type of scattering involves Phonons or lattice vibration quanta. The other type of scattering involves creation or annihilation of phonons by incident photon. This is the type of scattering that facilitates Raman analysis [100]. The energy and momentum conservation equations for such a process are shown as below in the following equation-

$$\hbar\omega_i = \hbar\omega_s \pm \hbar\omega_p \quad \dots\dots\dots 20$$

where i, s and p refer to incident, scattered photon and phonon respectively.

In the equations shown above, the minus sign refers to a process that creates a phonon and is called Stokes scattering; the plus sign to a process that destroys a phonon and is called Anti Stokes scattering.

Photon momentum is very small compared to phonon Brillouin zone width. Hence Raman scattering is restricted to a very narrow band of allowed frequencies at the center of Brillouin zone by the law of conservation of momentum [109]. For crystalline Silicon, there is only one active phonon mode at 520 cm^{-1} and hence only one peak at this value in the Raman Spectrum [109]. Amorphous silicon has a much broader spectrum which is essentially centered around 480 cm^{-1} . The reason for this is that in Amorphous material laws of conservation of momentum is more relaxed, with the result that several that several allowed phonon vibration modes exist. Thus, we can see that from the position

and the shape of Raman peak we can determine whether the material is crystalline, amorphous or mixed phases.

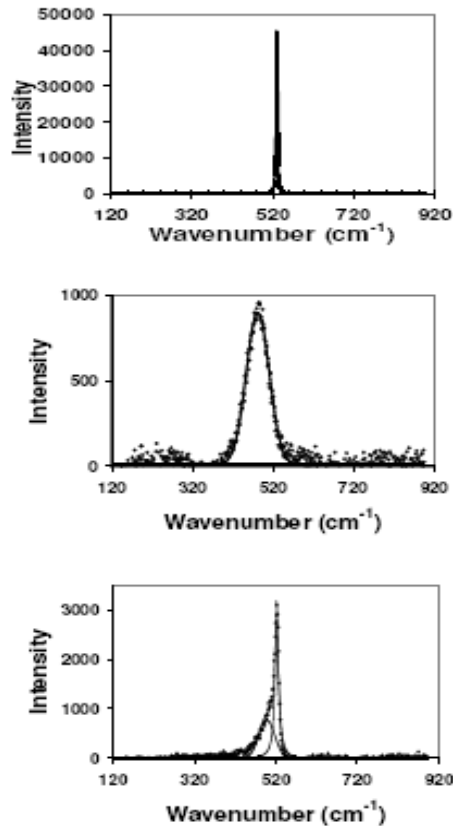


Figure 3.10 Raman Spectrum for Crystalline, amorphous and mixed phase [13]

Another important piece of information which can be obtained from Raman spectra is extent of crystallinity which can be obtained from Full width at half maximum (FWHM). The Percent crystallinity can be obtained from the FWHM of amorphous and crystalline phase.

(d) Photo and dark conductivity

The light and dark conductivity measurement gives us an idea of the quality of the material. High light conductivity indicates high quality photovoltaic material, while dark conductivity gives us an idea about bandgap of the material. Higher dark conductivity implies lower bandgap.

These measurements are conducted in an apparatus consisting of probes placed in a light impervious box. Two spring loaded probes are placed on contacts. Coplanar Cr contacts are deposited by evaporation, on which Ag paint has been applied. Width /Length (W/L) ratio showed in Figure 3.10 should be maintained above 20 so that fringe effect becomes negligibly small.

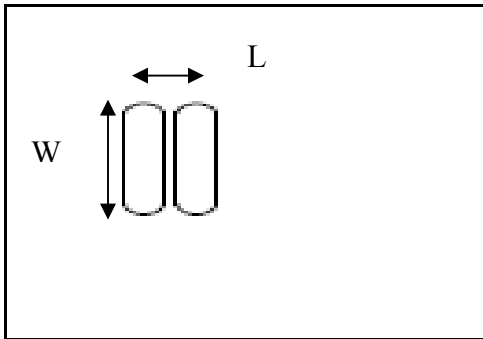


Figure 3.11 Cr contacts evaporated on top of the film used for photo/ dark conductivity and activation energy measurement. The W (width)/L (length) ratio is about 24 for all the samples measured.

After application of Ag paint, it is air dried for 5-10 minutes and then baked in a furnace for about 30 minutes. The probes are connected to Keithley 617 electrometer and a Keithley 230 voltage source to supply 100V bias between two contacts. The photo current is measured by turning on a quartz lamp directly above the sample that has a calibrated such that 100 mW/cm^2 is incident upon the sample, the standard AM 1.5 illumination. Dark conductivity is measured after switching off the light and allowing the sample to remain inside the chamber for 30 minutes.

The conductivity is then calculated using the following equation-

$$\sigma_{L,D} = \frac{W \cdot I}{L \cdot V \cdot t} \quad \dots\dots\dots 21$$

Where W/L is width / length ratio indicated in the Figure above, I is current measured, V is applied voltage, t is the thickness of the film.

(e) Activation energy

The conductivity of a semiconductor depends on the carrier concentration, which has an exponential dependence on temperature. Mathematically, we can write down the relationship as –

$$\sigma = \sigma_0 e^{-E_a/(K.T)} \dots\dots\dots 22$$

Where E_a = activation energy, K = Boltzmann’s constant, T = temperature (K), σ_0 is the pre-exponential factor. For amorphous I layer material, E_a tells us about the position of Fermi level wrt to Conduction band.

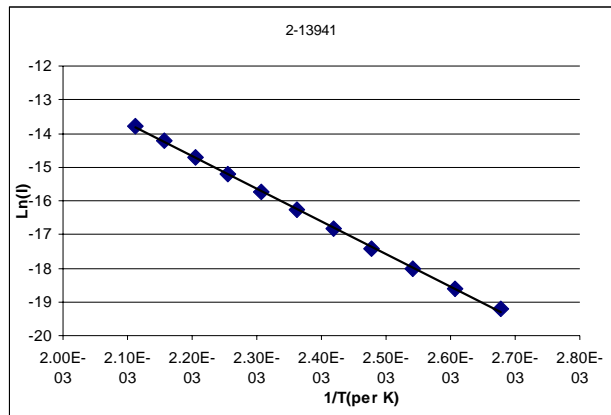


Figure 3.12 Plot of Ln (I) vs inverse of temperature.

When measuring this parameter, the sample is placed on a heated aluminum block and a spring-loaded contact is placed on each side of the coplanar contacts described earlier. The sample is then sealed in a light impervious box and heated to ~ 200°C. Current measurements, while applying a bias of about 100V, are taken from 200°C to 100°C in 10 degree decrements and then Ln (I) is plotted vs. 1/T as shown in the above Figure. This plot is then modeled by linear regression and the slope of that line multiplied by K to determine the activation energy. Typically amorphous I layer samples exhibit Activation energy values of about half the Tauc’s gap. If the sample has been unintentionally doped with oxygen or due to PH₃ cross contamination, then the activation energy will come out to be abnormally low.

(f) Energy dispersive Spectroscopy

A very useful tool in tracking Ge content of films is Energy dispersive spectroscopy (EDS). The EDS setup comprises of (a) the beam source, (b) X-ray detector(c) the pulse processor, and finally (d) the analyzer. It is a variant of X-ray fluorescence spectroscopy whose basic operating principle is characterization of matter by its interaction with electromagnetic radiation . The setup analyzes X-rays emitted by the material when it is bombarded with charged particles. It takes advantage of a very basic principle that each element has a unique atomic structure allowing X-rays that are characteristic of an element's atomic structure to be identified uniquely from one another.

To stimulate the release of characteristic X-rays from a given material, a high-energy beam of charged particles (electrons), or a beam of X-rays, is focused into the sample being studied. When an atom is in unexcited state, electrons are in discrete energy state and are bound to the nucleus. However, when the atom is hit with a high energy beam, the electrons are ejected from their shells and the vacancies in the inner shells are filled by an outer, higher energy shell electron and the difference in energy between the two energy levels involved is released in the form of X –ray – which can be detected by EDS spectrometer. Since the X ray emitted depends on the difference in energy between the energy shells and atomic structure, they can be regarded to be the signature of the atoms present in the material.

In addition to EDS, back scattered electron (BS) imaging is also a very useful tool in detecting qualitatively the composition of the material. It is well known that BS image can be lighter or darker depending on whether the material is heavier or lighter, which will depend on the amount of bulkier element present in the given sample.

The equipment used was an FEI Quanta-250 SEM with field-emission gun, located in Materials Analysis and Research (MARL). Images were collected with FEI's solid-state BSE. An IXRF EDS system was used for the x-ray analysis. Most of the spectra were collected at 7.5 kV accelerating voltage to avoid penetrating the SiGe layer to the steel below.

CHAPTER 4 RESULTS

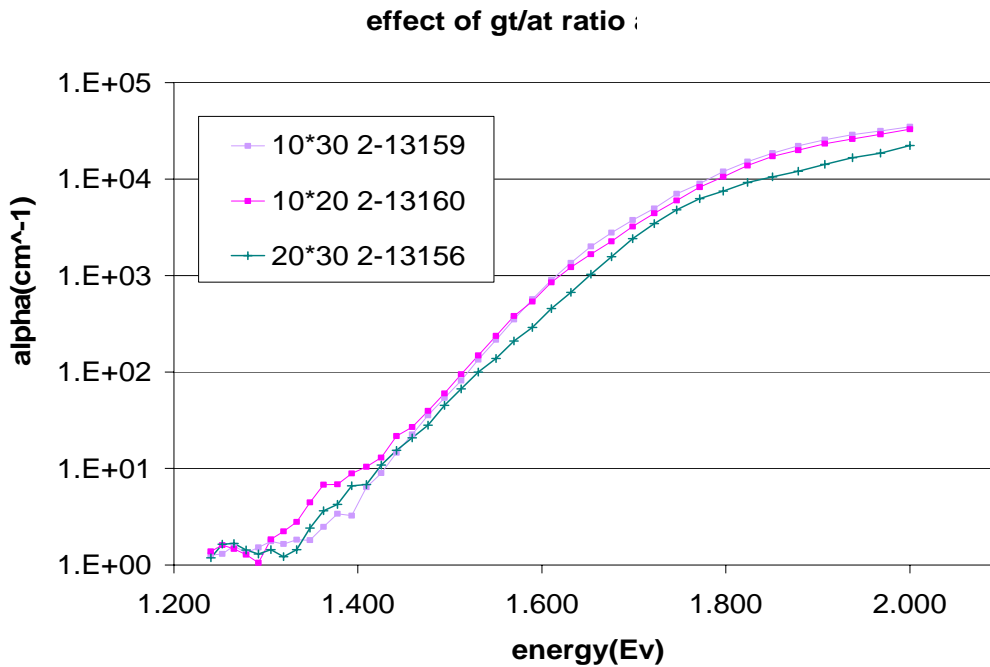
4.1 A-Si chemical annealing*(a) Device Results*

Figure 4.1 Effect of varying growth time (gt) and annealing time (at)- left hand side is growth time and Rhs is annealing time

During the course of our research, we had observed that the most important parameter that facilitates effective chemical annealing (CA) and lowering of bandgap- is low growth per cycle (between 7 – 15 Å/cycle). This is essential as Ar being bulkier than H, cannot penetrate deep into the lattice, so for proper ion bombardment it was essential to keep growth rate lower and thus film thickness. If we were however to adopt higher Ion energies , Ar will be able to penetrate thicker films but it will come at the expense of device quality[110] .Series of experiments were done to vary the growth per cycle- like reducing growth time and lower pressure . A series of SRIM simulations shows us the depth upto which Ar and H can penetrate.

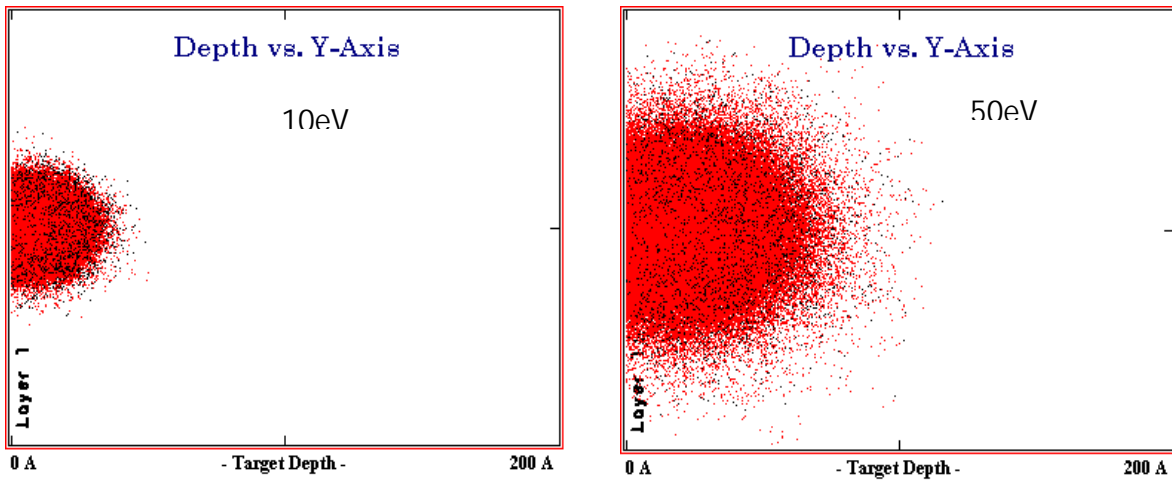


Figure 4.2 Penetration depth for H as function of Ion energy

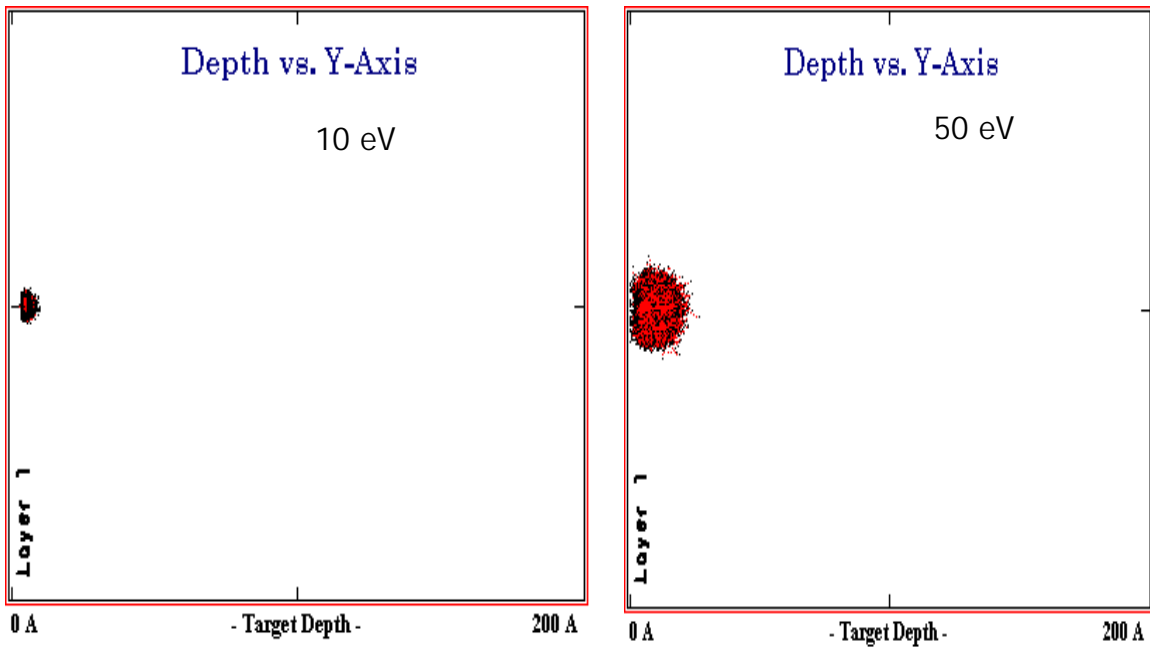


Figure 4.3 Penetration depth for H as function of Ion energy

From Figures shown above it is clear that while H can penetrate deeper as Ion energy is increased from 10 eV to 50 eV, for Ar annealing depth of penetration is not much even at high ion energy. However, damage cause by Ar annealing is very significant as shown by the graph for collision events shown in the next page for 50eV Ar ion energy.

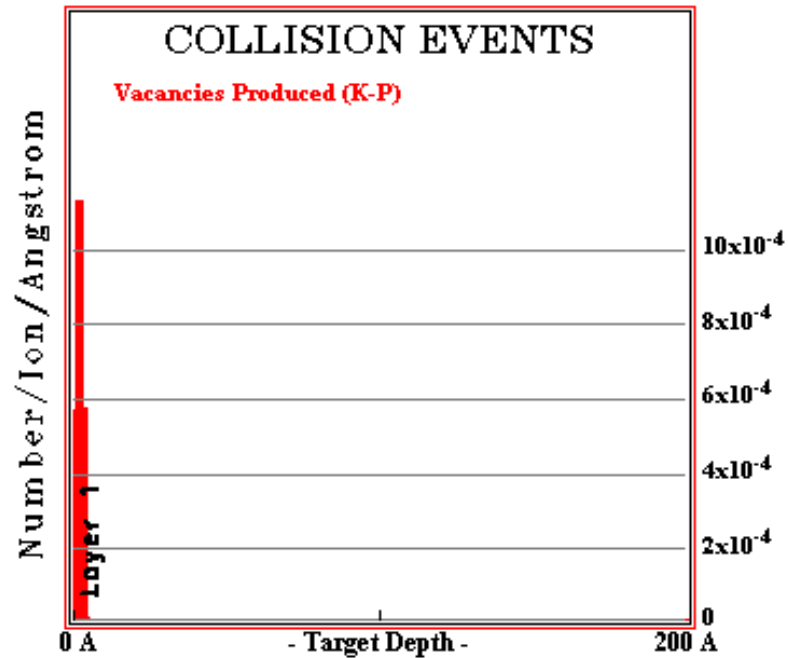


Figure 4.4 Lattice Damage due to 50eV Ar ions

The pressure variation was done so as to change the ion energy and flux impinging on the surface. A lower pressure results in both higher ion energy and higher flux of ions impinging on the surface, and thus we could vary the amount and energy of ion bombardment.

The following parameters were adopted Chemical annealing:-

- (i) During the growth cycle, Silane and Argon (Silane -3-5 sccm, Ar - 35-40 sccm) was allowed to flow
- (ii) During anneal cycle, only Ar was allowed to flow
- (iii) Two types of temperatures were studied - 300 °C and 250 °C
- (iv) Comparisons was made with continuous grown devices – (a) Non CA H₂ in which case no Ar was allowed to flow and (b) NON CA Ar in which only Ar was allowed to flow .

From here onwards, we will discuss various treatments done as part of chemical annealing and their effects on bandgap and device quality using mostly absorption energy curves.

(I) Effect of varying growth time (varying growth per cycle)

As shown in Figure 4.1 above, when growth time was reduced from 20 s to 10 s, there was a lateral shift in absorption energy curve towards left, signaling a decrease in bandgap. This agrees with the simulation shown above- since Ar is bulky, it is crucial to keep the growth per cycle low so that Ar can penetrate fully inside the material and cause sufficient ion bombardment to lower the Hydrogen content.

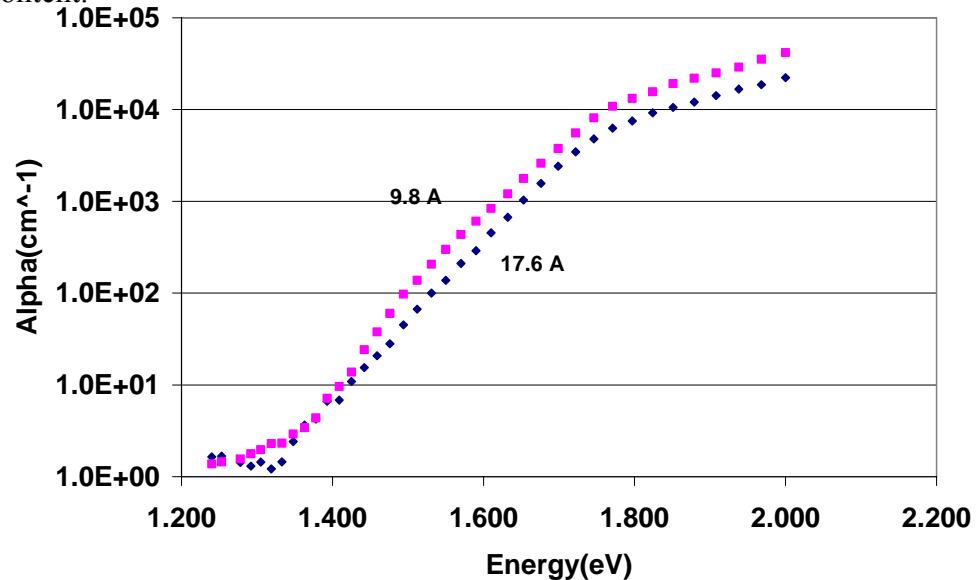


Figure 4.5 Absorption energy plot for growth rate of 9.8 Å/cycle and 17.6 Å/cycle.

The above mentioned fact can be also verified separately when absorption curves of two devices grown at 9.8 and 17.6 Å/cycle is compared. The lateral shift towards left in curve for lower growth per cycle signals drop in bandgap.

(II) Effect of lowering pressure

It is evident from the Figure below that lower pressure leads to better ion bombardment and thus lower bandgap. However, too low pressure (15 mtorr) can lead to poor device quality by causing too much ion bombardment. Clearly for 15 mtorr, midgap defect state density is increased as the absorption energy curves corresponding to it has a much higher shoulder than that for 30 mtorr or 50 mtorr

device. Thus, the need for the right pressure is highlighted so that bandgap can be lowered without adversely affecting device properties.

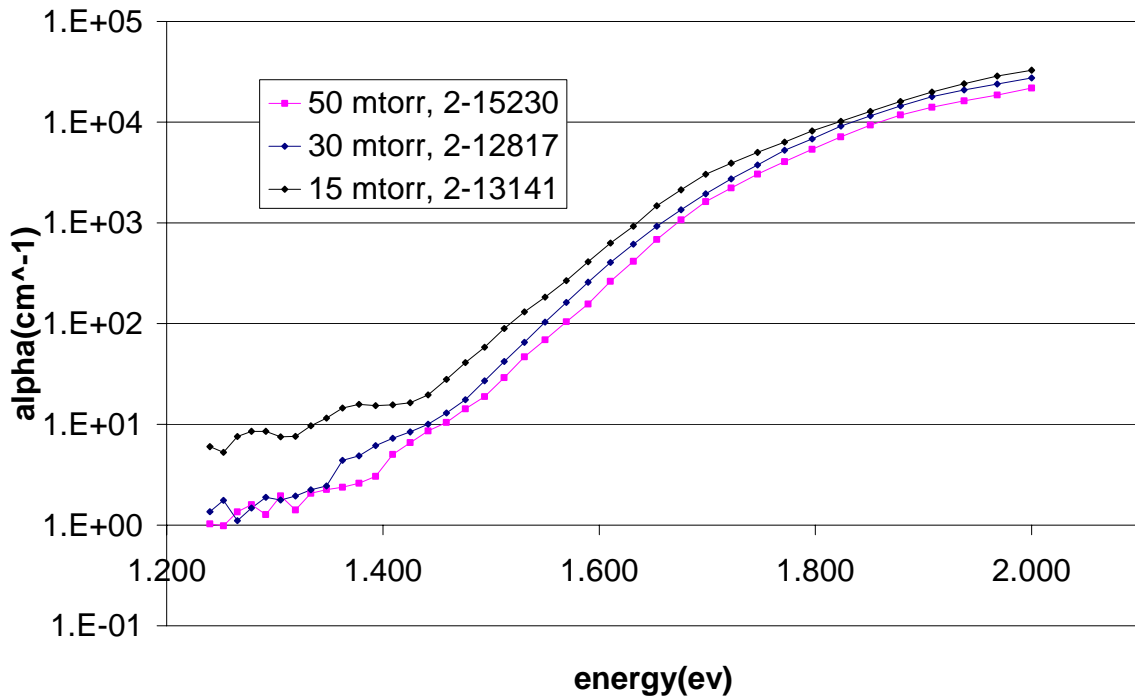


Figure 4.6 Effect of varying pressure on the bandgap of the material

(III) Effect of addition of H in annealing cycle

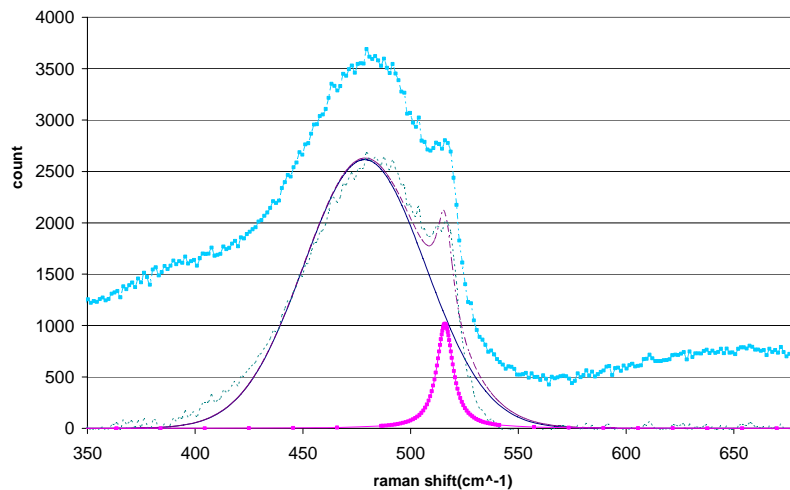


Figure 4.7 Raman data for CA device with H in annealing stage

As indicated by Shimizu et al [52], we observed that use of H in annealing and growth stage leads to crystallization. This was seen when CA device was fabricated

using H in annealing as well as growth cycle at 300C. The crystallinity is evident from the Raman peak seen around 520 cm^{-1} .

(IV) Final results

Two devices, fabricated at 325C are shown below– one CA device fabricated at 9 A/cycle microns and other non CA(H₂) with I layer thickness of about .26 and .41 microns respectively. Their IV s are shown below:-

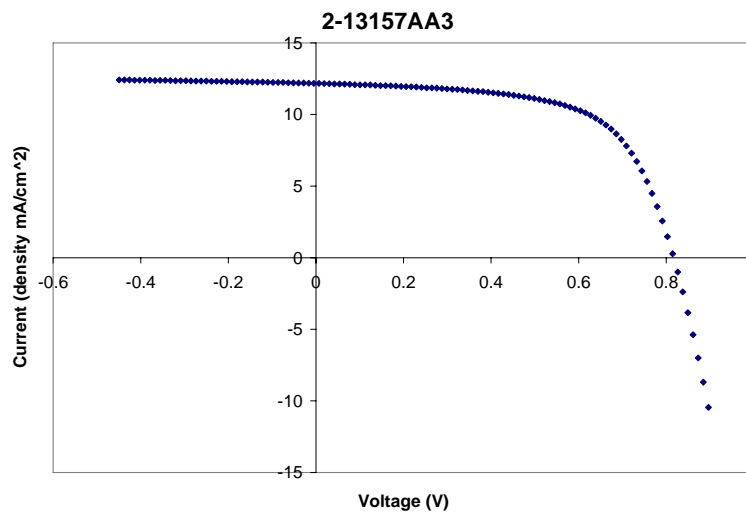


Figure 4.8 Iv curve for 9A/cycle CA device - Voc= 0.82V, Jsc = 12.2 mA/cm², FF = 65%,

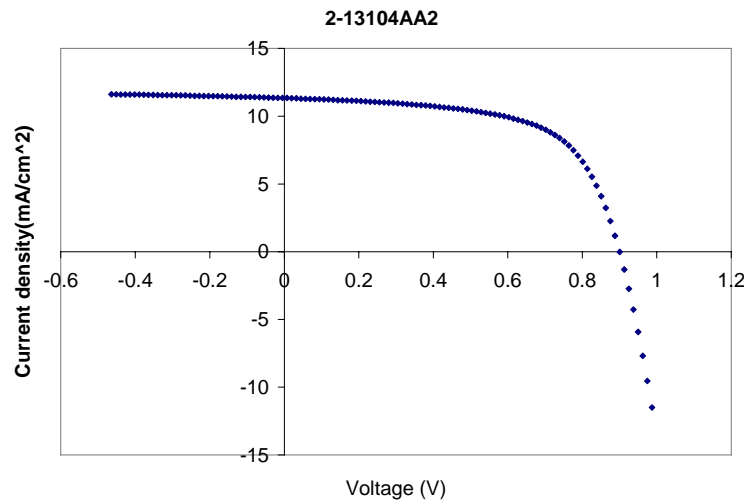


Figure 4.9 IV curve for NON CA sample -Voc =0.91V, Jsc = 11.4 mA/cm² FF = 63%

The non CA had been fabricated under continuous flow of SiH₄ and H₂, while CA using flow of SiH₄ and Ar only. The fact that both of them have high FF indicates

the chemical annealing is not adversely affecting material property. Again since the Voc has dropped from .91 to .82, and current density gone up (I layer thickness being the same), we can conclude that bandgap has dropped

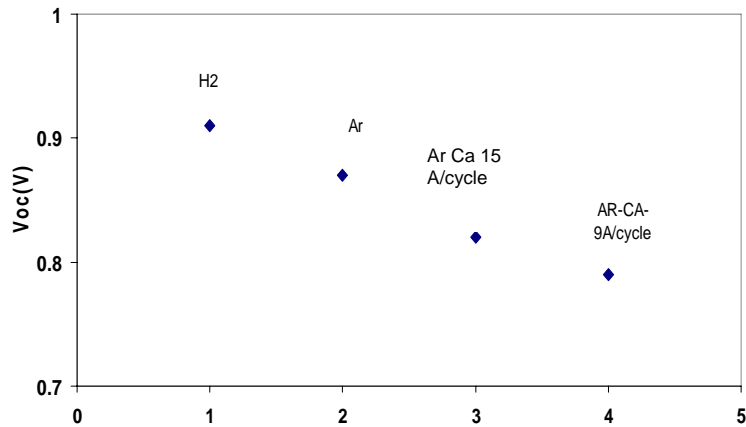


Figure 4.10 Plot of Voc for various CA and NON CA devices

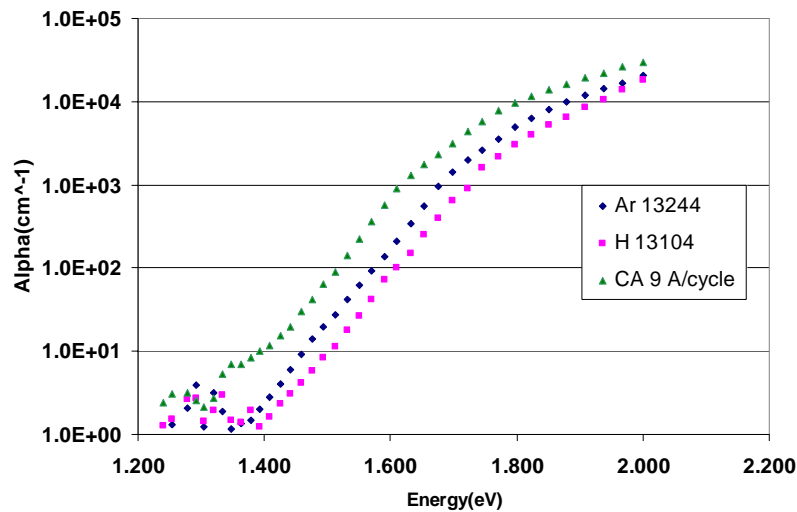


Figure 4.11 Absorption energy plots for CA vs NON CA (Ar) and NON CA (H₂)

From part (a) we can see that 9A/cycle CA has the lowest bandgap compared to H₂ NON Ca (H 13104) and Ar NON Ca (Ar 13244). Also we see that Urbach energy, which is obtained from the slope of the absorption energy and is an indication of the quality of the material is almost the same for all materials (almost 45 meV). So we have managed to decrease the bandgap, as suggested by the drop in Voc, which is a good indicator of bandgap without adversely affecting device quality.

(V) Light soaking studies

Two devices were subjected to light soaking – one CA and other NON CA (Ar). Both the devices were fabricated at 325C, CA had a bandgap of about 1.62 eV, NON CA (Ar) had a bandgap of about 1.7 eV. As expected CA device showed better stability than NON CA indicating that CA device has lower loose Si-H bond content than NON CA, as indicated by FF, Voc and J_{sc} degradation data.

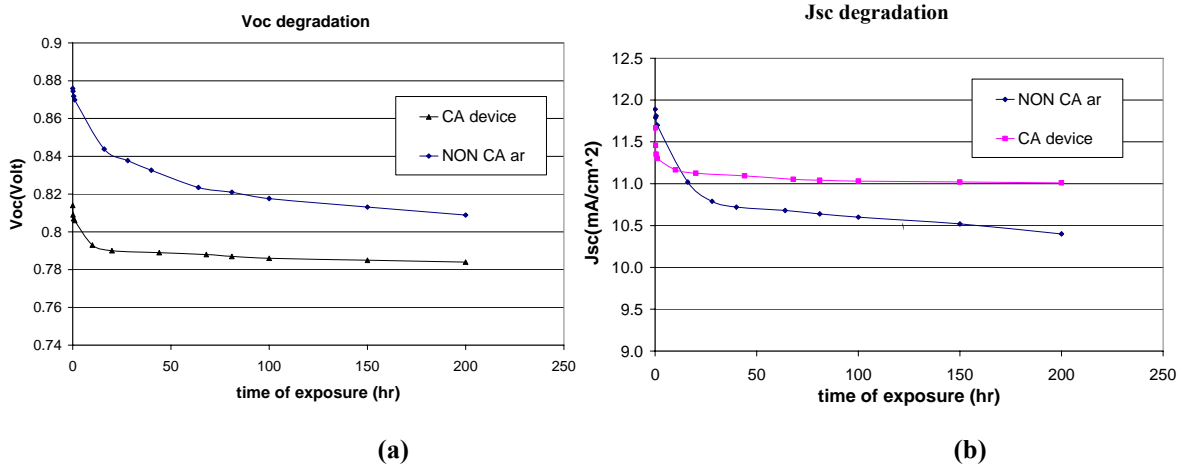


Figure 4.12 Effect of light soaking on (a)Voc (b) J_{sc} degradation for CA and NON CA devices as a function of time of exposure (hrs)

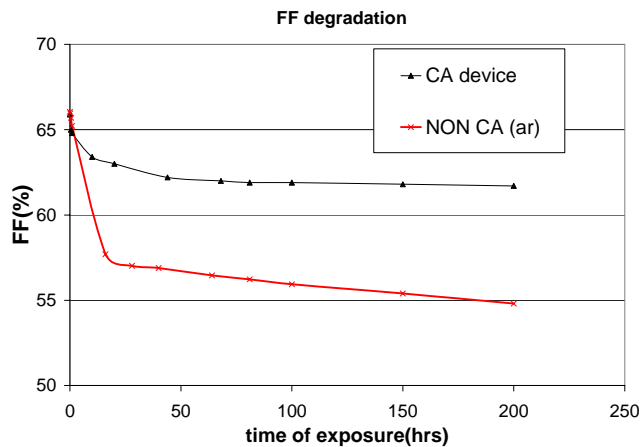


Figure 4.13 Effect of light soaking on FF degradation for CA and NON CA devices as a function of time of exposure (hrs)

This data is further validated by the changes in absorption curve shoulder and QE ratio before and after light soaking. Clearly for CA devices, there is very little

change in absorption curve shoulder before and after light soaking whereas for NON CA devices, a very prominent increase in absorption shoulder is seen, indicating a significant increase in defect density.

CA device before and after light soaking

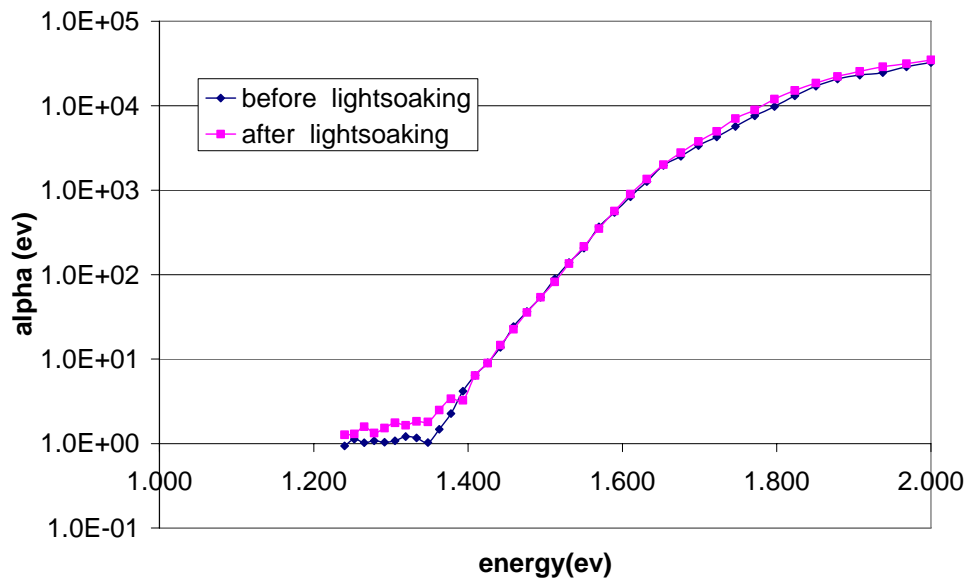


Figure 4.14 Absorption energy data for CA before and after light soaking
NON CA AR light soaking data

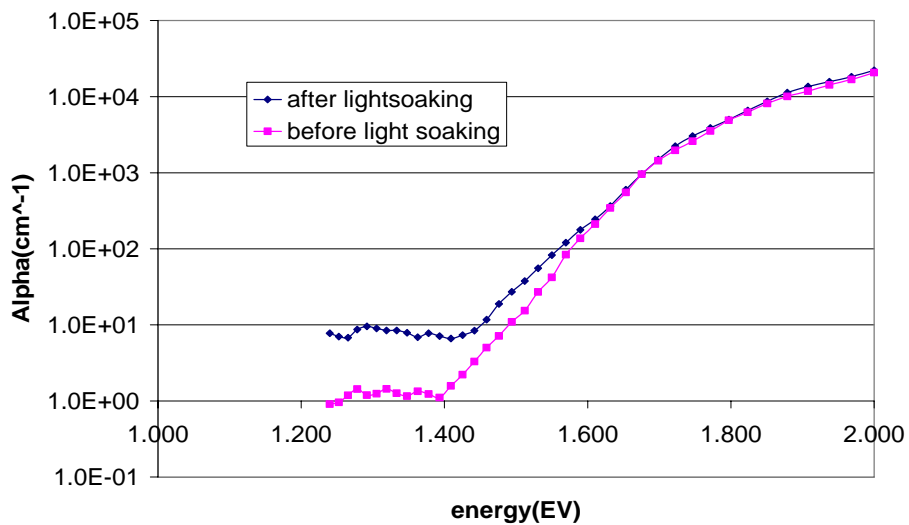


Figure 4.15 Absorption energy data for (a) NON CA before and after light soaking

qe before and after lightsoaking_CA

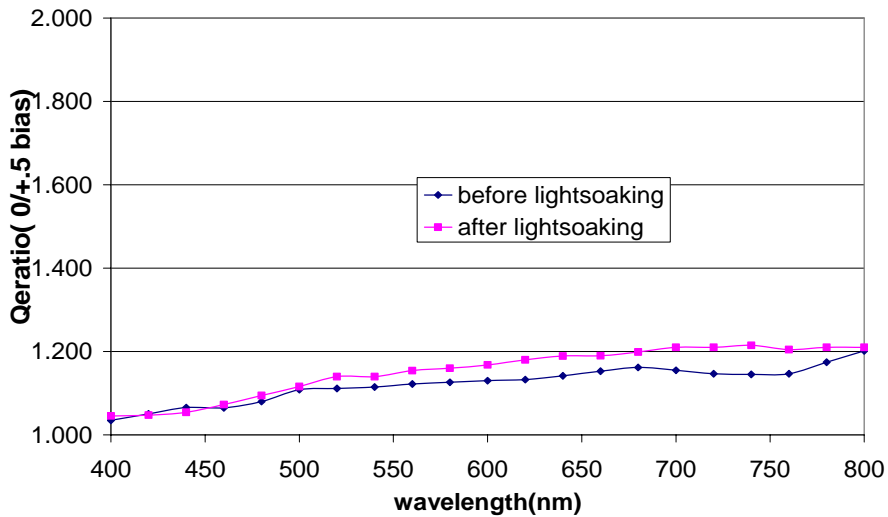


Figure 4.16 QE ratio (0/+5) data for CA before and after light soaking

qe before and after lightsoaking_non CA

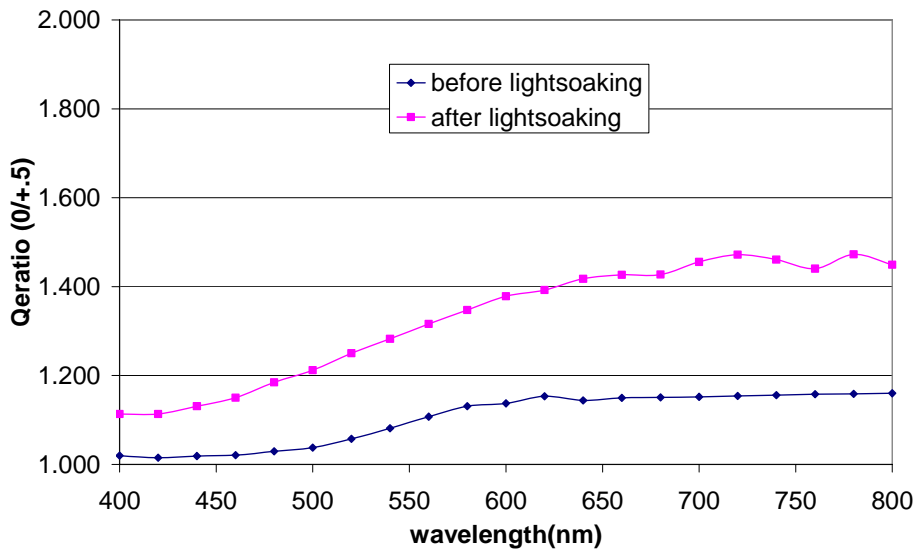


Figure 4.17 QE ratio (0/+5) data for NON CA (Ar) before and after light soaking

It is seen that there is very little change in QE ratio for the CA device before and after light soaking whereas for NON CA big change in QE ratio is observed. This again agrees very well with subgap data shown above. The data set shown above indicates the success of chemical annealing in improving stability of material

(VI) Hole mobility lifetime product for CA vs Non CA devices

To find out more about quality of CA devices, we decided to fabricate .5 micron thick devices to accurately estimate hole mobility lifetime product. These devices were also used for defect density estimation. It was found that NON CA (Ar) and 1.65 eV CA device had almost identical Urbach energy (45 meV) and identical hole mobility lifetime product.- $3.6 \times 10^{-8} \text{ cm}^2/\text{V}$, indicating high quality

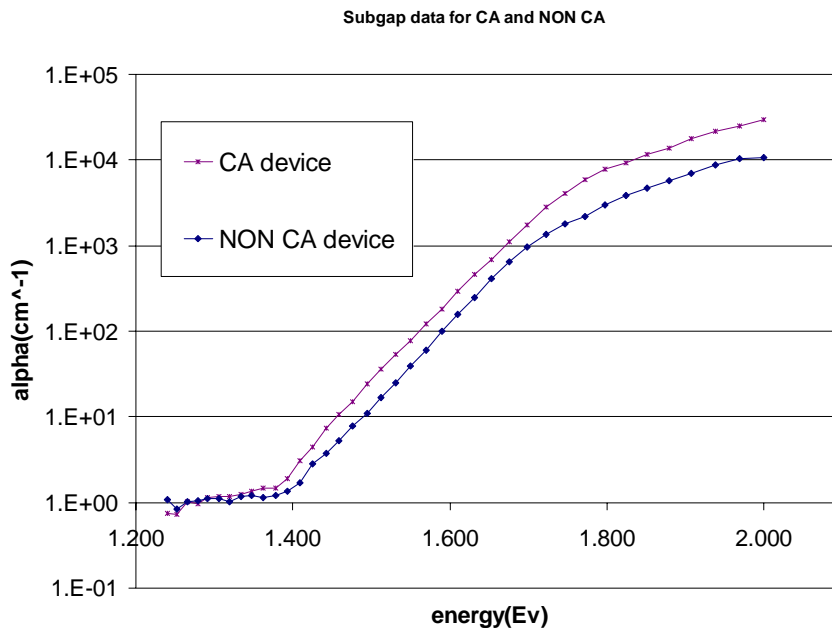


Figure 4.18 Absorption energy data for CA and NON CA device selected for hole mobility lifetime product measurement

As explained above, for the purpose of calculating hole mobility product , we assumed that built in electric field is approximately $V_{oc}/(2 \cdot \text{thickness})$. The reason for 2 in denominator is that Electric field is not uniformly distributed throughout the device, but shows most of its drop in p-I and n-I interface as shown in Figure 3.5. Using an iterative method, we can approximate the hole mobility lifetime product value that allows calculated Quantum efficiency vs bias voltage to match with measured one for 3 different wavelengths- 600 nm, 680 nm and 760 nm

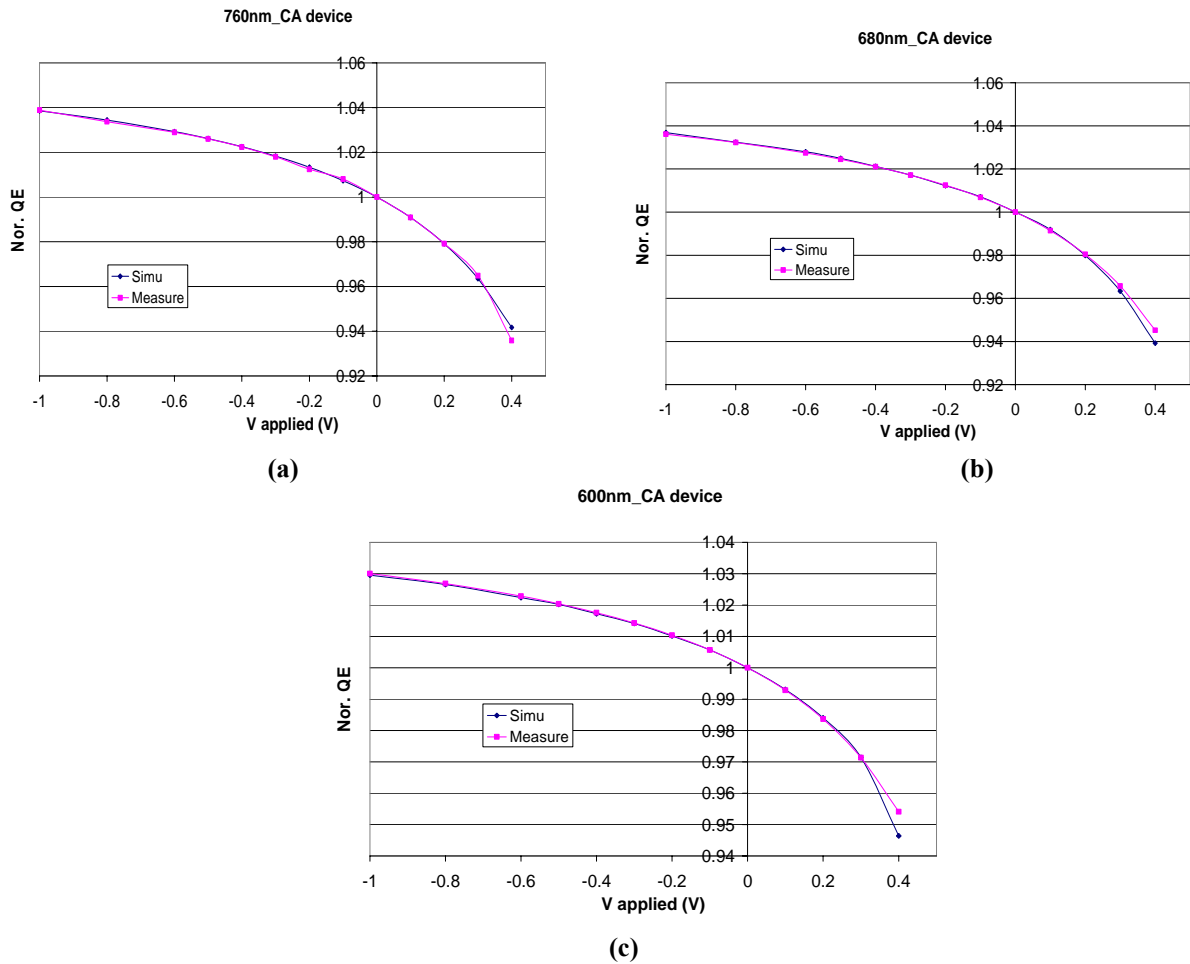


Figure 4.19 Simulation and measured QE vs bias for 1.65 eV CA device at (a) 760 nm (b) 600 nm and (c) 680 nm

It was observed that all the curves show a good fit with measured data in all three cases for hole mobility-lifetime product value of $3.6 \cdot 10^{-8} \text{ cm}^2/\text{V}$

Similarly for NON CA device it was seen that the best possible fit was observed for all the three wavelengths is about $3.6 \cdot 10^{-8} \text{ cm}^2/\text{V}$. So it is proved that CA and NON CA devices have similar quality.

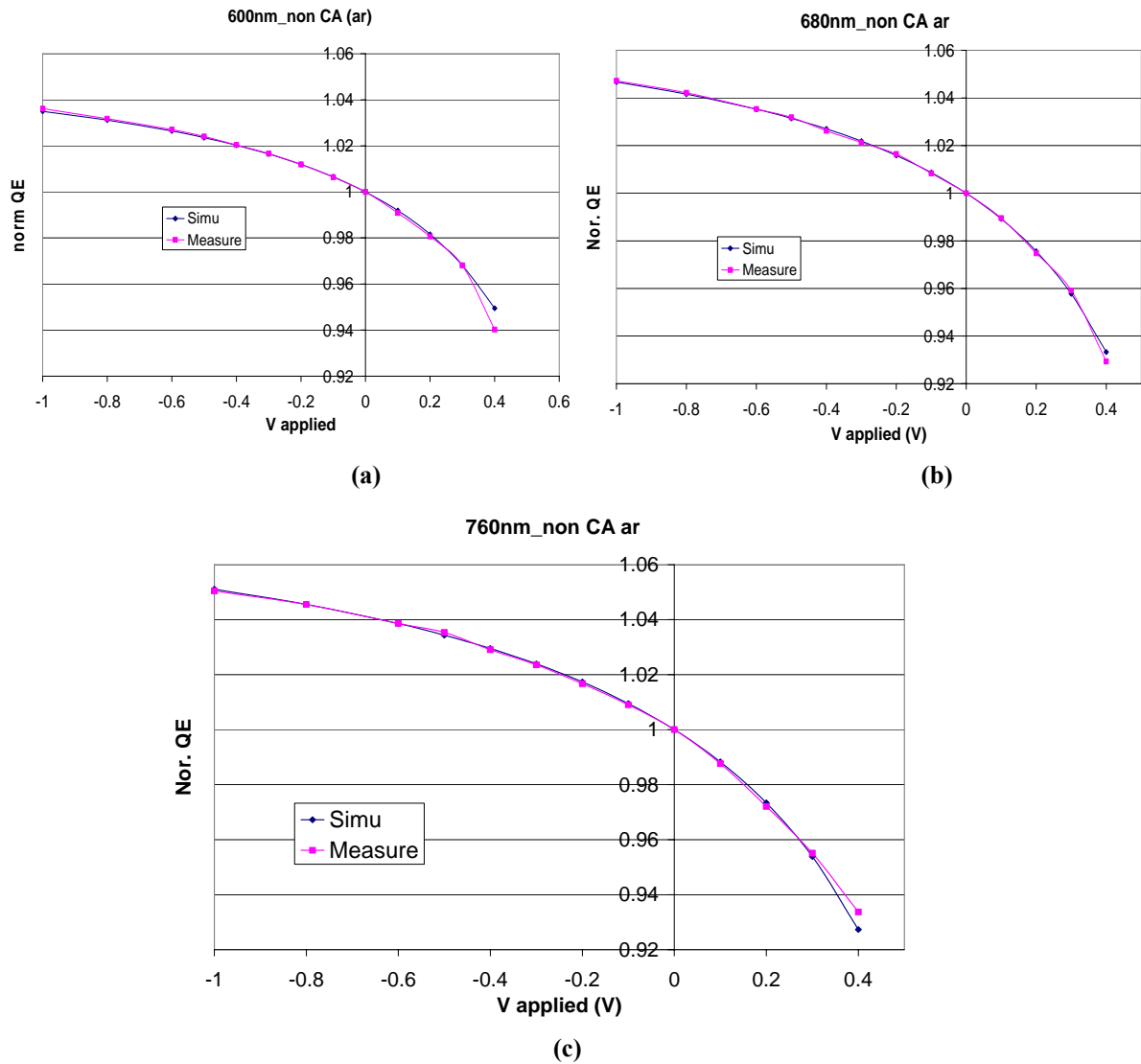


Figure 4.20 Simulation and measured QE vs bias for NON CA (Ar) device at (a) 760 nm (b) 600 nm and (c) 680 nm

(VII) Defect density plot and calculation

We also plotted density of states as function of trap energy level (E_t) relative to conduction band for CA and non CA device and found that they have similar quality. The integrated defect density for both the cases has been calculated to be close to about $7 \cdot 10^{15} \text{ cm}^{-3}$, which agrees very well with that obtained from CV analysis at 20Hz, 150C ($\sim 7.6 \cdot 10^{15} \text{ cm}^{-3}$). From the Absorption energy data shown

in Figure 4.18, it can be seen that CA and NON CA absorption have identical absorption shoulder, indicating that they have same defect density or in other words same quality- thus indicating success of chemical annealing.

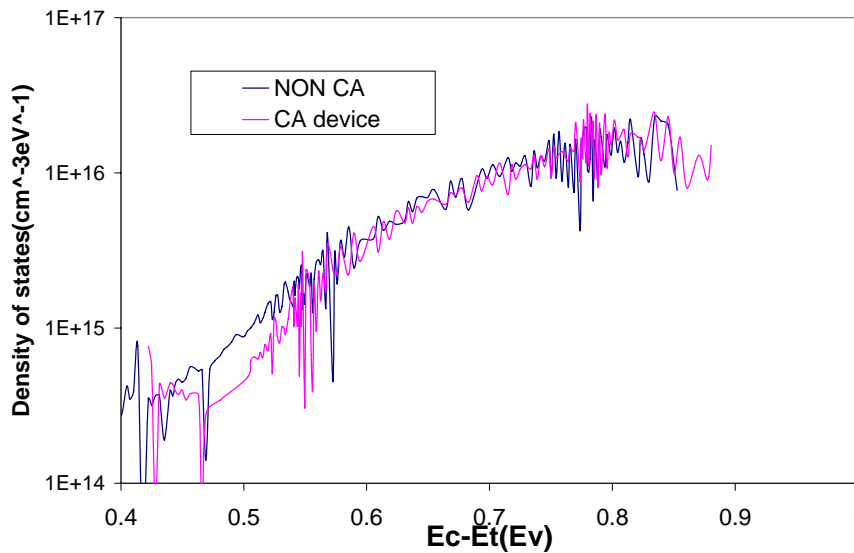


Figure 4.21 Plot of defect density for CA vs NON CA devices

(b) *Film Results*

(I) H content data obtained by FTIR

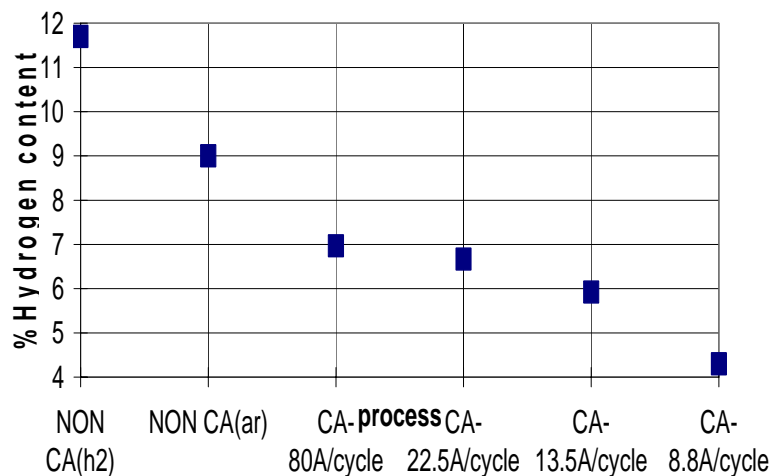


Figure 4.22 Hydrogen content as a function of various CA and non CA parameters

We had been postulating that chemical annealing reduces the bandgap by reducing the Hydrogen content. Thus non CA should have most Hydrogen content and CA

process should have lower Hydrogen content. It has been observed that NON CA (H_2) has highest Hydrogen content of about 12 at % , followed by NON CA (Ar) at 9 at % and the lowest Hydrogen content (~ 4 at%) being obtained for the lowest growth per cycle (8.8A/cycle). The CA follows expected trend of lower growth per cycle leading to lower H content.

comparison of CA vs nonCA

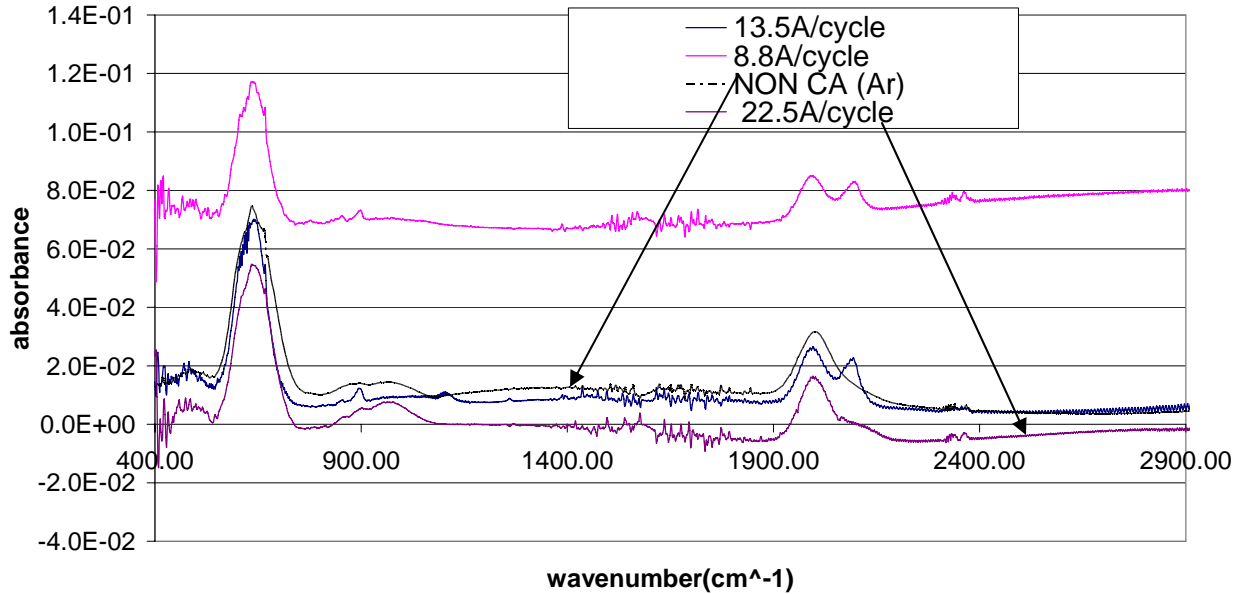


Figure 4.23 FTIR data for various CA and non CA parameters

(II) Electronic and optical properties of Film grown on Glass

Table 4.1 Comparison of optical and electronic properties of A-Si CA and NON CA A-Si films

Sample type	PC (1/Ωcm)	DC (1/Ωcm)	Activation Energy(eV)	Urbach energy (meV)	Thickness (μm)	Tauc (eV)
CA, 10 A/cycle	4.91E-05	7.01E-10	.822	45	.63	1.66
NON CA (Ar)	4.95E-05	1.62E-10	.844	45	.72	1.73
CA,20 A/cycle	5E-5	1.75E-10	.837	45	.63	1.74

For the completion of our study of A-Si we decided to grow CA and NON CA (Ar) films to compare their electronic properties and compare their bandgaps. It is clear for CA film of 10 A/cycle and 20A/cycle growth the electronic properties are comparable with that of NON CA (Ar), while at the same time bandgap of lower growth per cycle CA film is lower than that of NON CA although fabricated at the same temperature of 300C, which is evident from Absorption energy curve for CA vs NON CA obtained spectrophotometrically. It is also seen that the bandgap of higher growth per cycle CA film is almost same as that for NON CA (Ar), once again highlighting the fact that higher growth per cycle is ineffective in causing sufficient Ar ion bombardment and does not thus affect the bandgap.

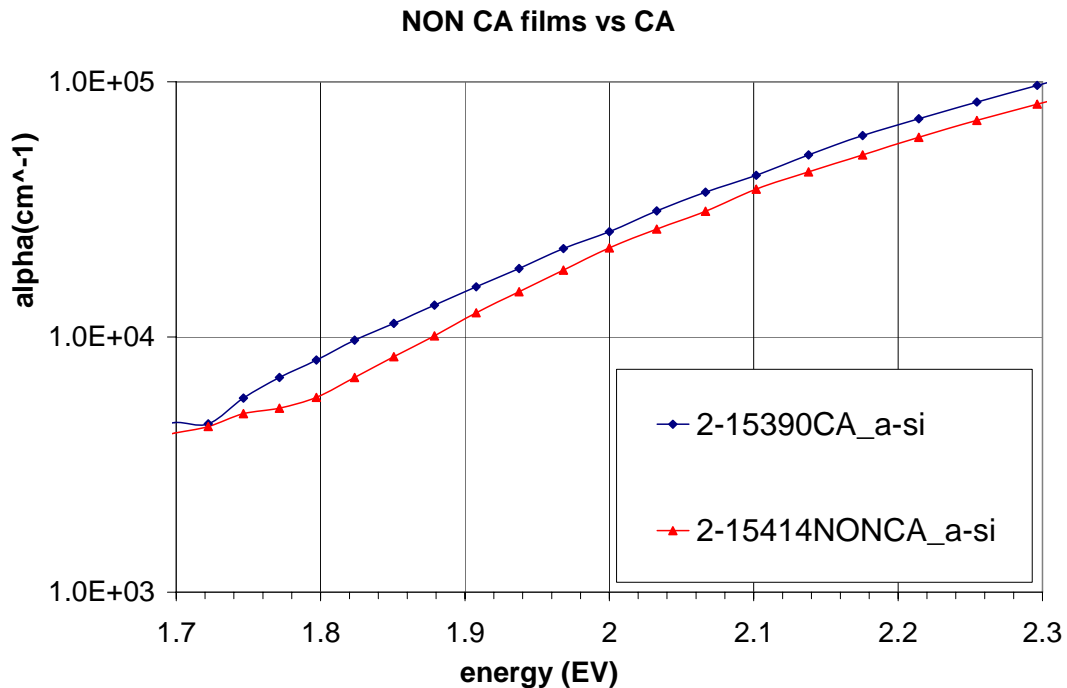


Figure 4.24 Absorption energy curves for CA(10 A/cycle) and NON CA films

We can thus see that we have successfully demonstrated the success of chemical annealing in achieving its desired goals- lowering bandgap without affecting device quality. All the major accomplishments of this treatment on Amorphous Silicon is summarized in the next subsection.

(c) Summary for A-Si chemical annealing

We can summarize the above results and parameters for chemical annealing as following for obtaining best possible results:-

(i) The most important parameter is low growth per cycle- any parameters that lead to this (like low growth time) will lower bandgap.

(ii) Optimum pressure is a must- Too high pressure can lead to inadequate bombardment, whereas too low pressure can lead to degradation of solar cell by causing excess bombardment.

(iii) We should not use any H_2 in annealing stage as it will interfere adversely with chemical annealing process and may even lead to crystallinity

(iv) Hydrogen content data obtained from FTIR confirms that chemical annealing treatment leading to lower growth per cycle, will lead to lower Hydrogen content and consequently lower bandgap

(v) Hole lifetime-mobility product data for devices, Urbach energy and other electronic properties of film convincingly proves that CA and NON CA materials have the same electronic properties.

(vi) Light soaking analysis proves that CA has better stability than NON CA- This is clearly proved from FF, Voc degradation data and ably supported by subgap measurements.

With the knowledge of successful technique of chemical annealing for A-Si, wherein we try to reduce bandgap without adversely affecting device quality, attempt will be made to emulate these for A-SiGe. The next section will deal with application of these techniques to Amorphous Si Germanium and highlight the challenges faced and their solutions devised.

4.2 A-SiGe chemical annealing Results

(a) Device Results

(I) Optimization of NON CA devices

Since a-SiGe is more defective than a-Si, so a very sophisticated bandstructure is necessary to obtain high quality a-SiGe devices. It was essential to have high quality NON CA before moving on to CA devices. The following band diagram was adopted by me for my research. This has been shown extensively by previous work of our group to lead towards high quality devices .

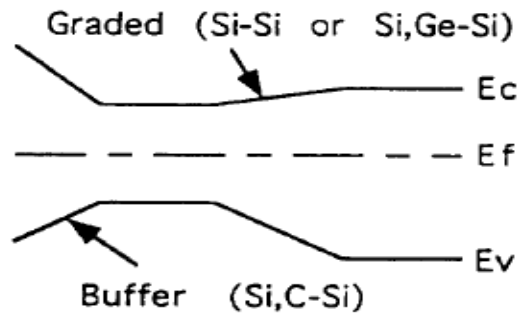


Figure 4.25 Band diagram for A-SiGe I layer fabrication in this research work [79]

The first non CA device had a very poor FF : 46% , high Rs of 112 ohm and also very serious hole collection problem as reflected by the high QE ratio (0 /.3) at higher wavelength . After a series of runs, we managed to optimized it and obtain a FF of 58.3%. The problem of hole collection was solved by increasing TMB flow during I layer fabrication and high Series resistance (Rs) problem was solved by using more heavily doped N+ and P+ for higher conductivity . All the devices had the same gas flow composition for the I layer- 30 Sccm H₂, 4 Sccm SiH₄, .4 sccm GeH₄. The improvement in hole collection at higher wavelength is evident from QE ratio shown below , which explains the increase in FF from 46 % to 58%. Further improvement in device property was obtained when effect of cross contamination due to previously deposited N+ layer on the electronic properties of current I layer was negated.

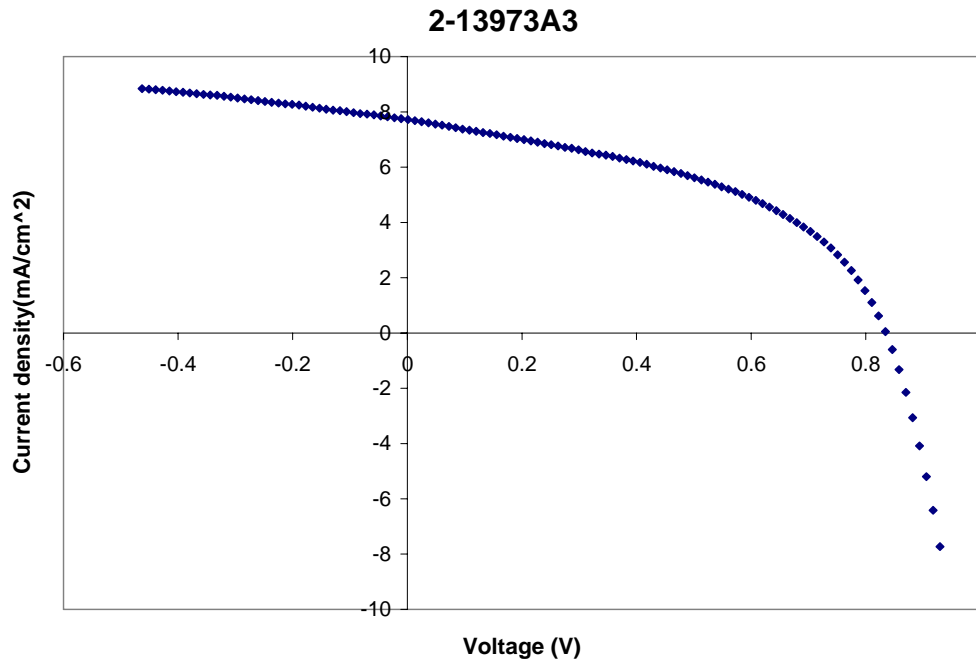


Figure 4.26 First non CA -I layer thickness = .26 micron, FF=46 %, Voc=.845V, Rs = 113 ohm

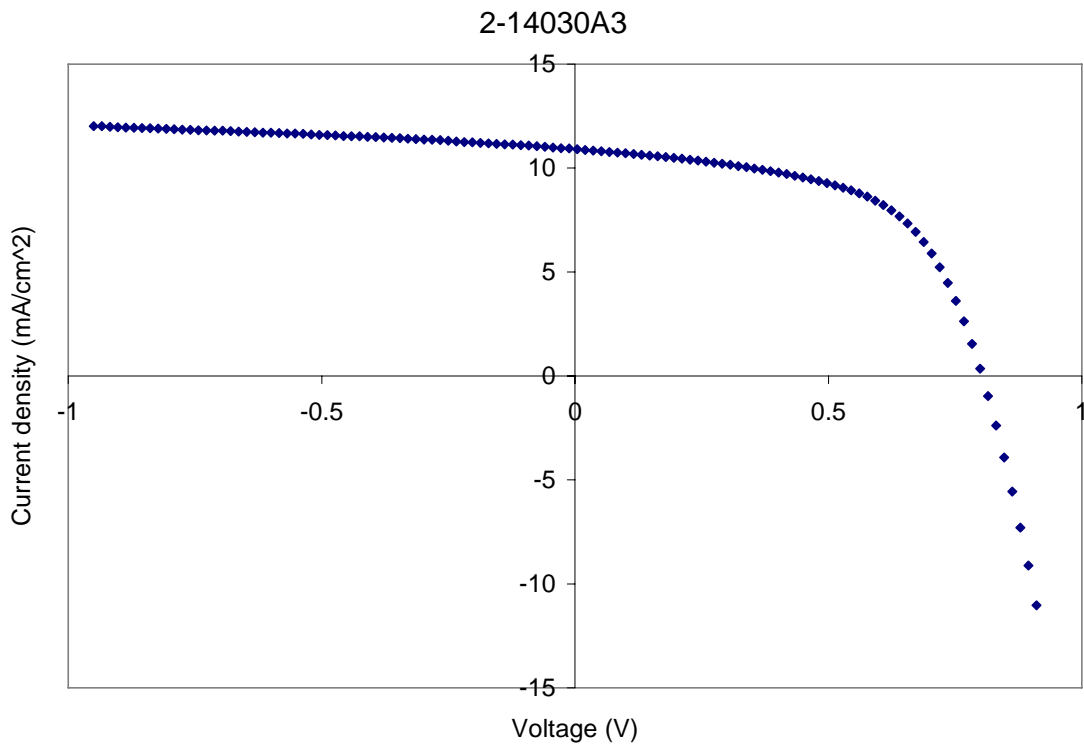


Figure 4.27 Better quality non CA - I layer thickness = .26 micron, Voc=.815, FF=58.3 %,Rs=84 ohm

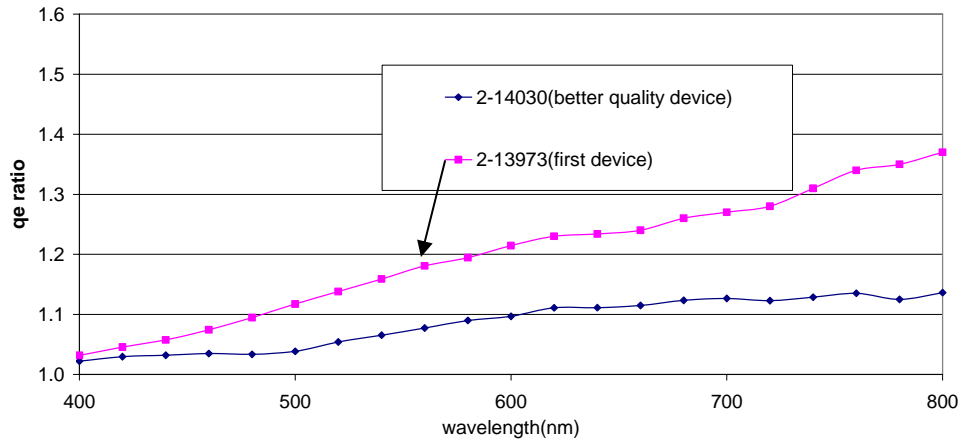


Figure 4.28 QE ratio for first non CA device and an optimized non CA device

This problem is serious for devices because the P+, I and N+ layer are grown in the same chamber. A good approach discussed by another group is to use Hydrogen plasma having high RF power to first etch away the N+ grown on the chamber wall and then deposit a new Intrinsic layer. The effect of this treatment was that hole collection problem was significantly improved as shown in Figure shown below and consequently FF shot up from about 54% to about 60%. Hereafter, Hydrogen etching after depositing N+ has become a mandatory practice as it has been seen to reduce cross contamination due to PH_3 significantly

effect of Hydrogen etching

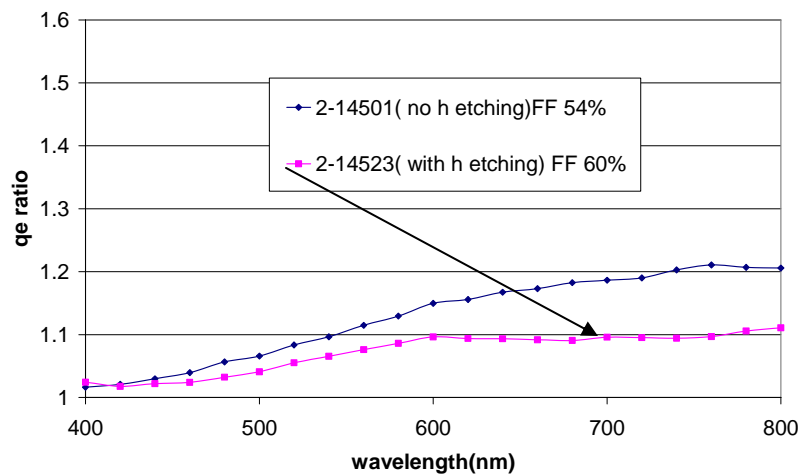


Figure 4.29 Effect of Hydrogen etching on device quality

(II) Initial problems with CA film and devices - trend of reverse band gap

After optimizing non CA, when we started making CA films we noticed a strange trend- CA was having higher bandgap than non CA. The same trend was seen when we made devices. This made no sense as till now for a-Si this was never noticed. Absorption energy curves for films showing the anomalous characteristics is shown below.

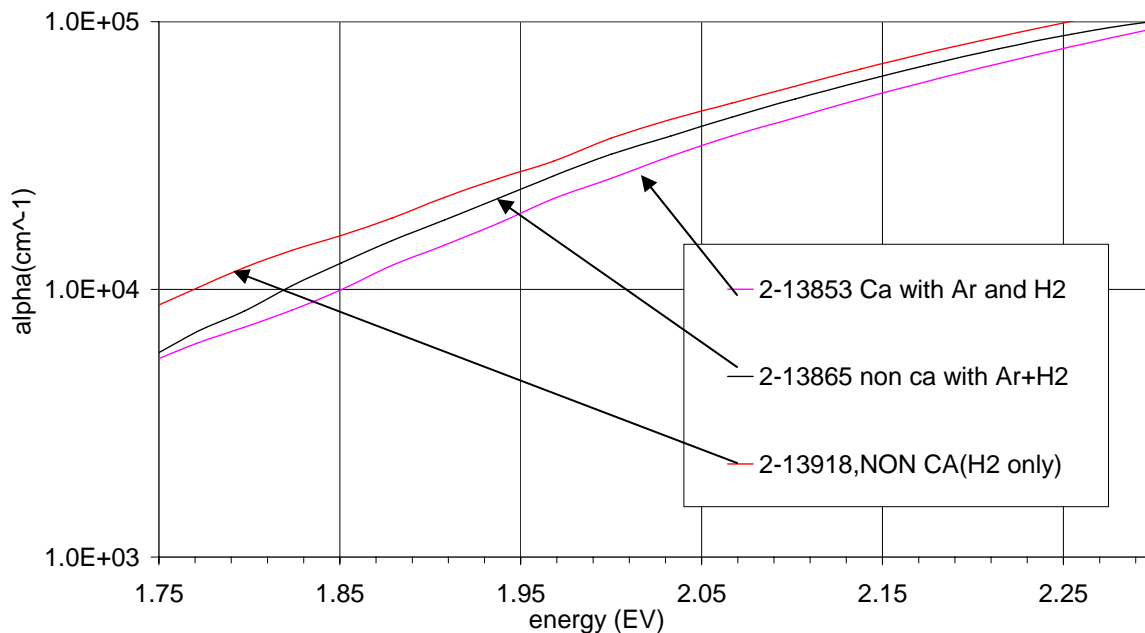


Figure 4.30 absorption energy curves for CA and non CA films

2-13853 and 2-13865 were made using identical gas composition of Ar and H₂ at 4 Rf W power and pressure of 50 mtorr. The other non CA (2-13918) was made using 60 sccm of H₂ and in the absence of Ar. There could be two reasons for such a trend- either chemical annealing was not successful or else SiGe composition was not identical in CA and non CA. We did an EDS experiment just to verify this as it seemed unlikely that CA was not able to lower H content. The EDS data told us something very unexpected.

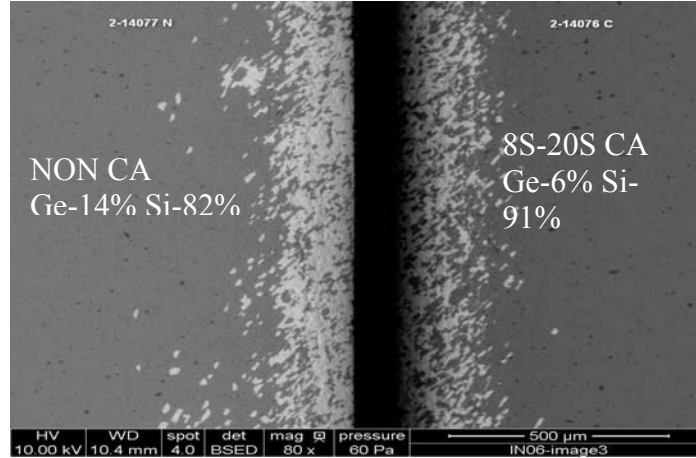


Figure 4.31 Back scattered image for CA vs NON CA

The EDS data told us that the Ge content in non CA was higher than NON CA. The back scattered image shown above verified this fact- the non CA was lighter than the CA , which can happen only if its effective mass is more than CA (as only then it would reflect more). The problem was solved when we did a CA device at 2 W RF with 20 s growth time. The reason for choosing 20 s as growth time was to maintain same growth per ($\sim 12 \text{ \AA} / \text{cycle}$) as 4.5 W RF CA, so that chemical annealing would not play any role in affecting the bandgap. The absorption energy curve for the devices are shown below

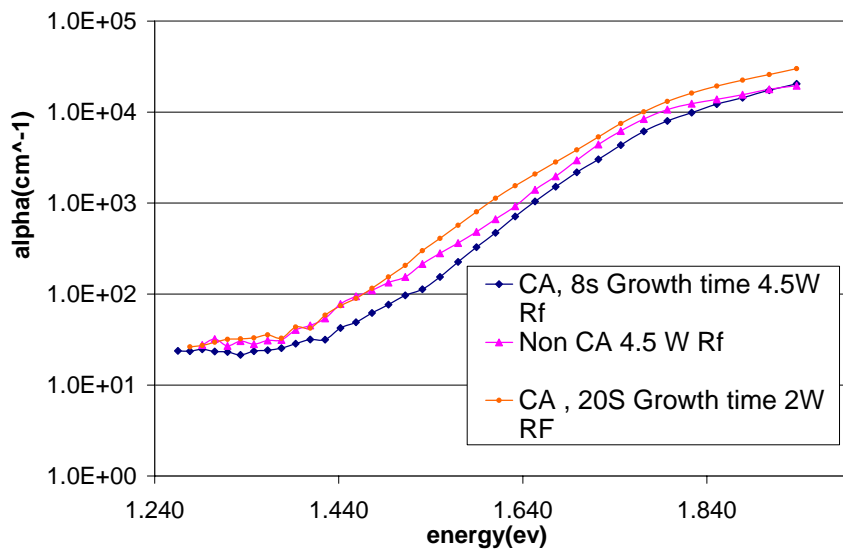


Figure 4.32 Effect of power on CA - absorption energy plot for 4.5 w Rf vs 2 W RF

The data shown above told us that in 4.5 W RF CA device, Ar during the annealing stage was etching away Ge. So when we reduced Rf power to 2W, the etching was reduced significantly and the absorp. energy curve shifted towards left of NON CA.

(III) Effect of varying dilutant gas composition

In the CA film data shown above, we saw that H₂ NON CA (2-13918) had lower bandgap than H₂ & Ar non CA (2-13853). This trend was also seen for devices, and can be explained on the basis of EDS data shown below. This actually matches the observation made by other group [60].

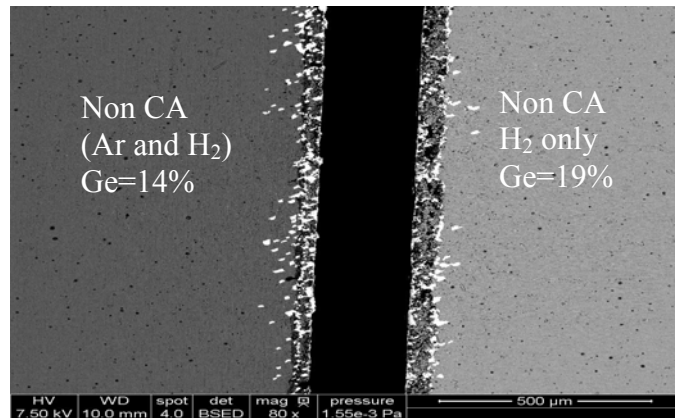


Figure 4.33 Effect of dilutant gas – H₂ vs H₂ and Ar

The EDS data confirms that only H₂, when used as a dilutant leads to greater Ge content as against Ar and H₂ when used as a dilutant. The significance of this experiment is that it is shown that we need to compare CA and NON CA having identical dilutant gas composition; otherwise we might be picking up effects due to non identical SiGe composition. Hence forth, unlike A-Si chemical annealing we cannot compare bandgap of CA device with that of NON CA (H₂).

(IV) Effect of pressure

Just like for A-Si, when pressure was lowered from 50 mtorr to 30 mtorr, due to enhanced ion bombardment a lateral shift in absorption curve was seen as shown in

the Figure above. However, the device quality also suffered due to increased midgap defect state density due to excessive ion bombardment, which is being highlighted by the elevated absorption shoulder for 30 mtorr device.

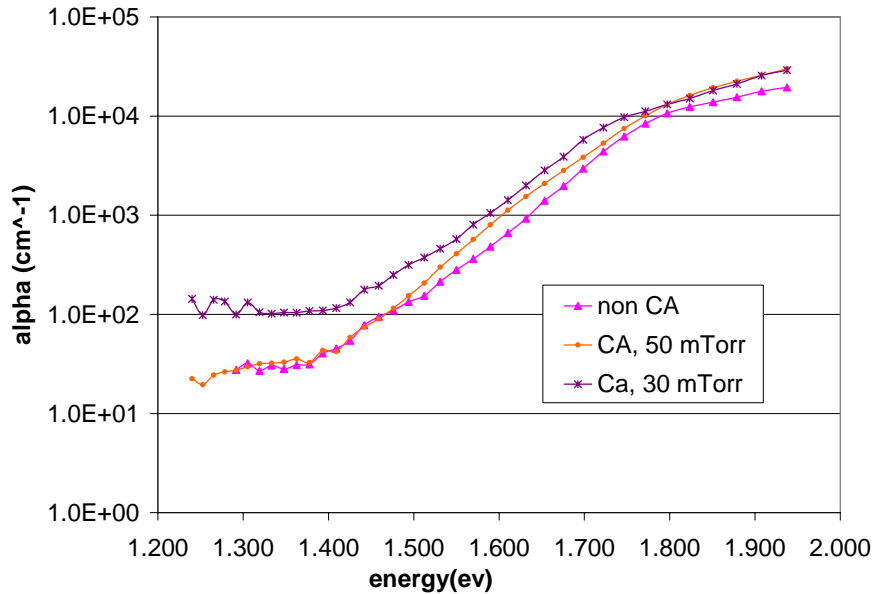


Figure 4.34 Effect of pressure – 30 mtorr vs 50 mtorr

(V) Effect of lower growth per cycle.

We had seen for A-Si that low growth per cycle is favored as Ar is a big atom and cannot penetrate deep into thick layers grown in each cycle, thus hindering effective ion bombardment and leading to ineffective chemical annealing. Same trend is seen for A-SiGe- when growth time is reduced from 20 s to 15s (keeping all other parameters the same), a lateral shift in the absorption Energy curve towards the left is seen signaling lowering of bandgap. The reason is obvious- reduction in growth per layer led to better ion bombardment of the film by allowing Ar to penetrate deeper and thus led to a drop in Bandgap by lowering the Hydrogen content.

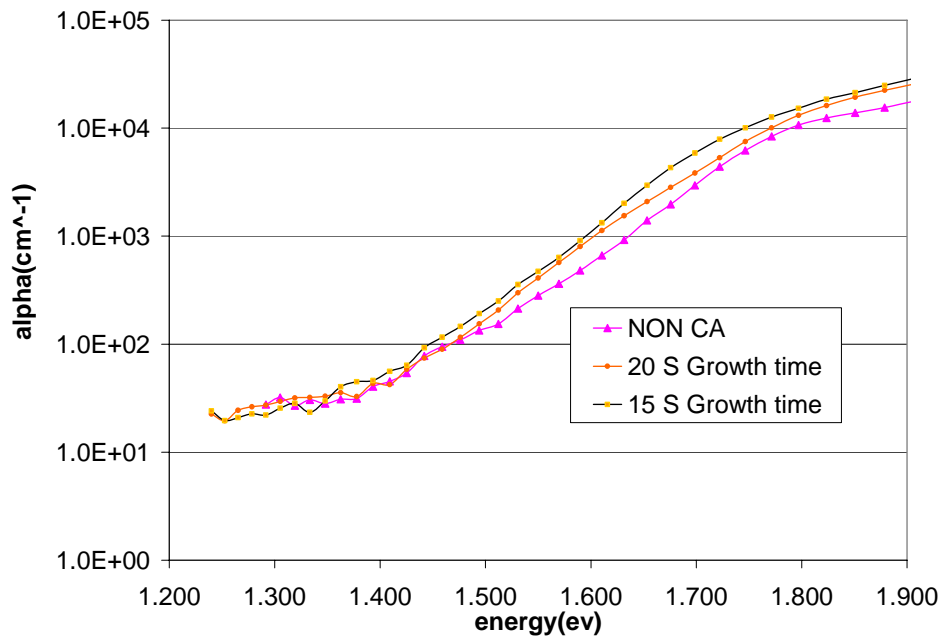


Figure 4.35 Effect of varying growth time – 15s vs 20 s.

(VI) Effect of increased hydrogen dilution

Till now the experiments had been done on CA and NON CA devices with 30 sccm H₂ flow and the typical FF for the best CA and NON CA device with this hydrogen flow was ~ 60%. These IVs have been shown below in Figure 4.36, 4.37 wherein, two device are compared – one CA and other NON CA at the same temperature of 275 C (pressure being 50 mtorr). For both the cases – gas flows were identical – 30 Scm H₂, 23 Scm Ar, 4sccm SiH₄, .4sccm Geh₄. Also shown is plot of Voc for various CA and NON CA parameters – the drop in Voc did not come at the expense of device quality, which clearly demonstrates the success of chemical annealing. However, even now the quality of device was not optimized as indicated by the high absorption shoulder (~ 30 cm⁻¹). So an attempt was made to improve quality by (~) doubling hydrogen dilution to push up the H₂:SiH₄ ratio of 7.5 to about 15. When absorption curves of two NON CA devices fabricated under higher and lower hydrogen dilution were compared (fig 4.39), the former showed a lower absorption shoulder indicating high quality, which is in agreement with similar studies reported

by Ganguly et al [65]. High hydrogen dilution may lead to a more ordered film structure and thus improves device quality.

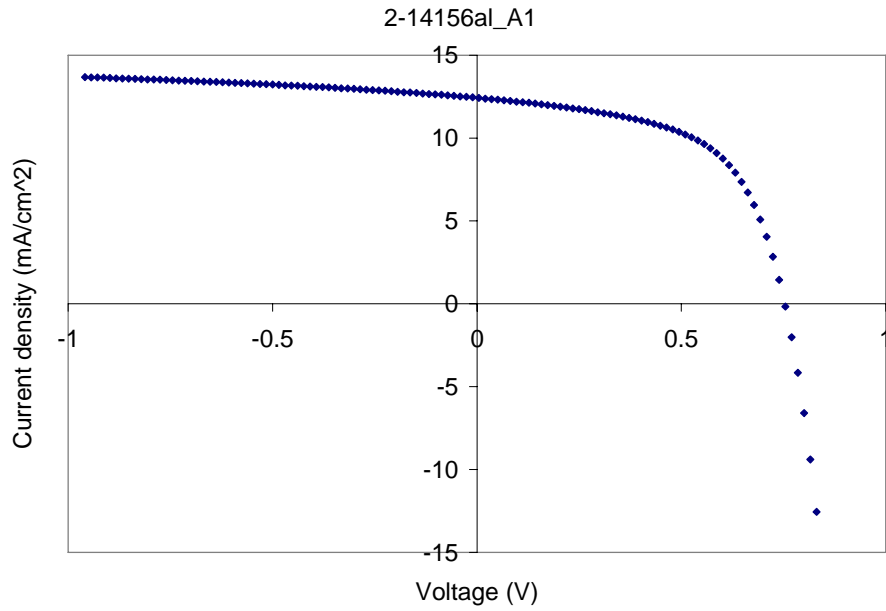


Figure 4.36 Iv for CA- I layer thickness =.28 micron, $J_{sc}=12.7 \text{ mA/cm}^2$, $V_{oc}=.79$, $FF=58.9$

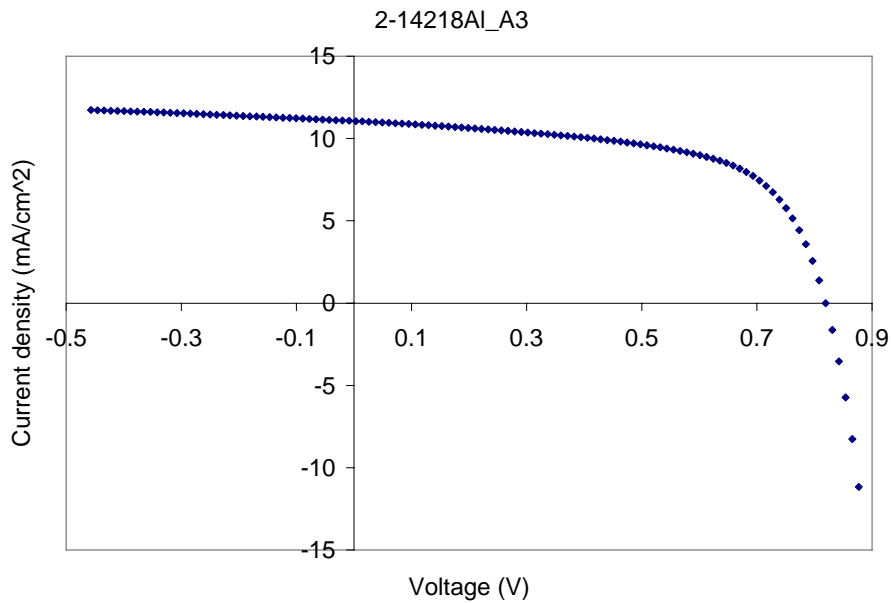


Figure 4.37 Iv for NON CA I layer thickness =.25 micron, $J_{sc}=11.27 \text{ mA/cm}^2$, $V_{oc}=.82$, $FF= 60\%$

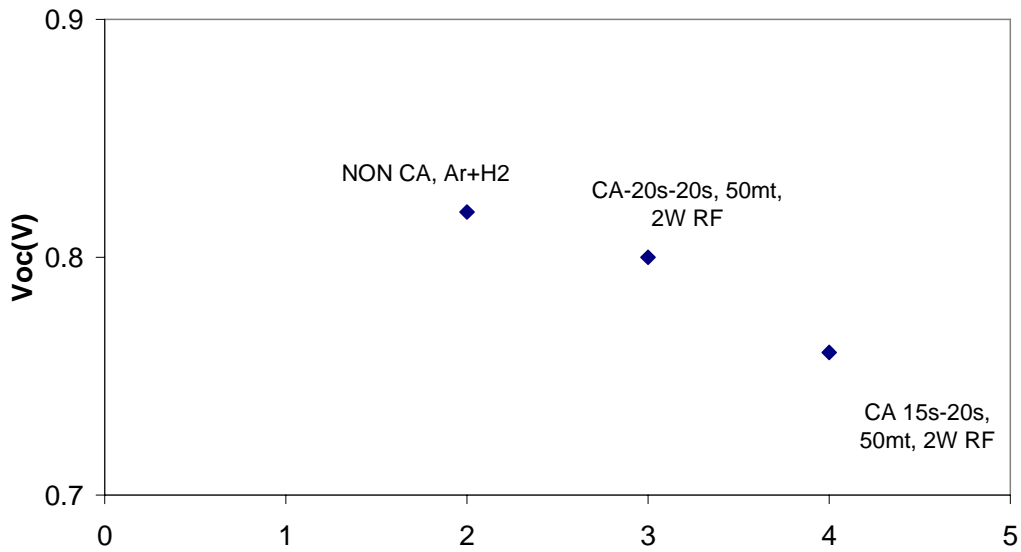


Figure 4.38 Voc as a function of various CA and non CA parameter

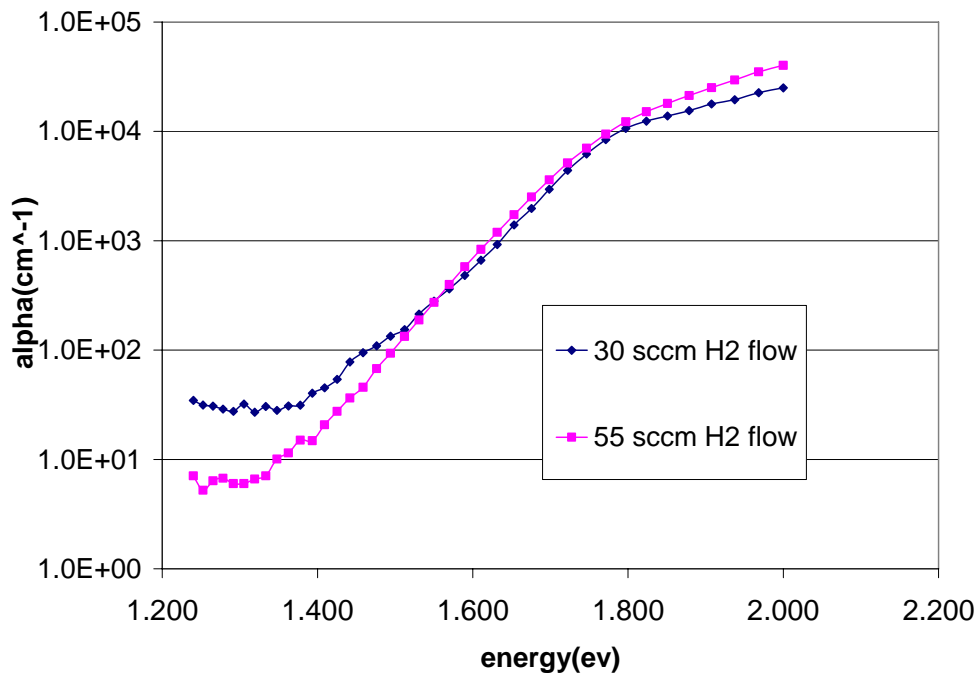


Figure 4.39 Effect of doubling Hydrogen dilution

(VII) Effect of varying growth inducing gas flow

A study was done on NON CA samples to see the effect of Reducing SiH₄, GeH₄ flow while keeping H₂ flow constant- the idea was to try and improve device

quality by increasing the $H_2:SiH_4$ from 15 to the extent possible without crystallizing the material. Table below shows various SiH_4 and GeH_4 flows for the films whose GeH_4 content is investigated. In all the cases the Flow of H_2 was about 60 sccm and Ar about 23 sccm.

Table 4.2 Table for various films with different SiH_4 , GeH_4 , Rf power and their corresponding Ge content

Case no	SiH_4 flow (sccm)	GeH_4 (sccm)	Rf power (W)	Ge content from EDS(%)
1	4	.4	4.5	14
2	3	.3	4.5	18
3	2	.3	2	22

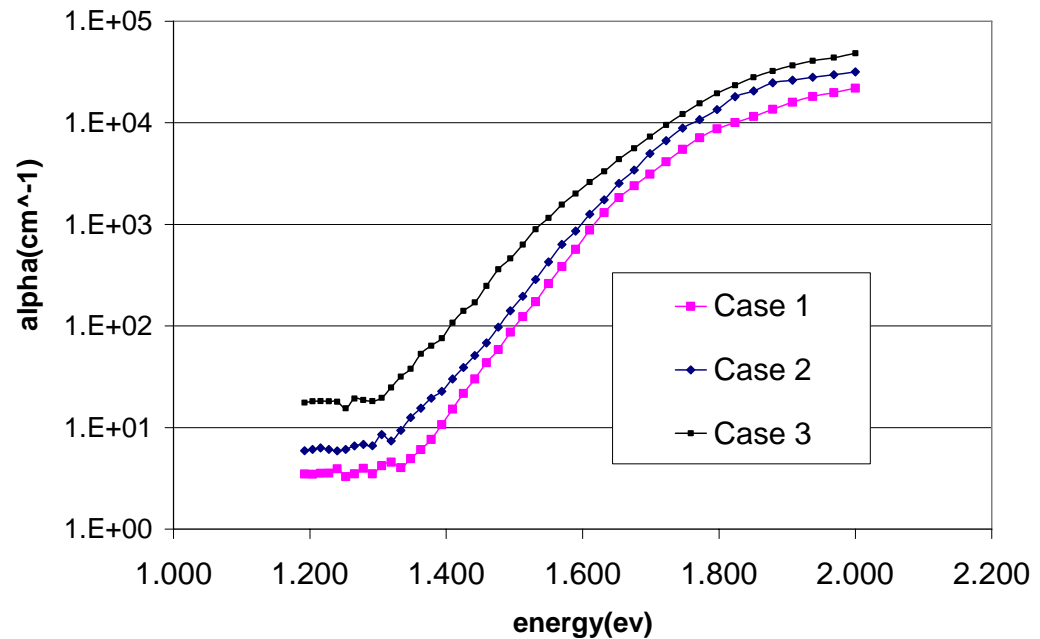


Figure 4.40 Absorption energy curve for devices corresponding to the cases enlisted in the table above. The reason for the gradual degradation of properties as we move on from Case 1 to 3 is increasing Ge content – which is confirmed by absorption data shown above and EDS data shown below for the cases enlisted above. The BSE image and Ge content

data clearly support this case- the BSE image for the case of higher Ge content is clearly lighter than the other case.

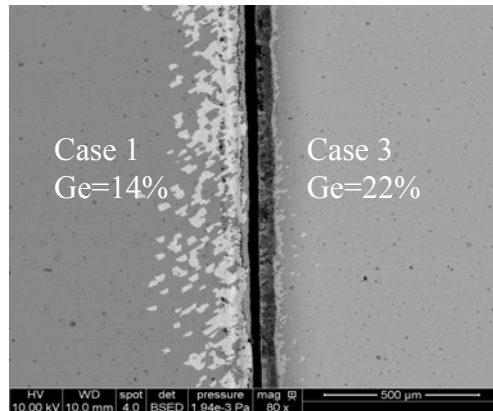


Figure 4.41 Backscattered image comparing Ge content for Case 1 vs Case 3

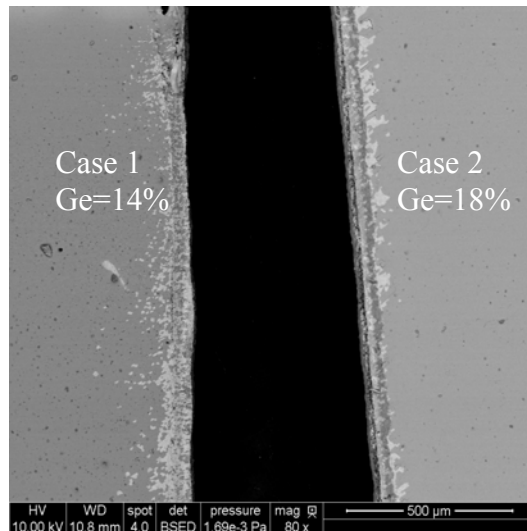


Figure 4.42 Backscattered image comparing Ge content for Case 1 vs Case 2

For the case 3, it was observed that Rf power played an important role in determining the crystallinity of the material. It was seen that at such high $\text{H}_2:\text{SiH}_4$ (~ 30) dilution, the material became crystalline even at relatively low Rf power of 4 W; however at 2 W Rf power the same material remained amorphous. While measuring Raman, low Laser power Intensity of 5% (of 1 mW) was selected to ensure that the laser did not crystallize the material accidentally. In the Raman data shown below, 520 cm^{-1} peak shows up for 4W RF power film but not for the film fabricated at 2W RF power.

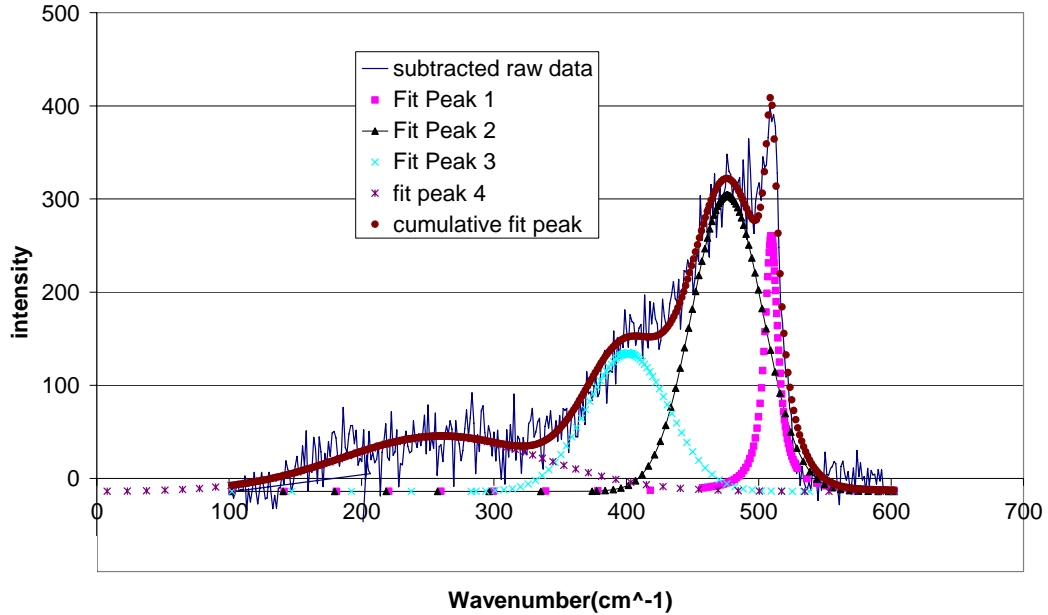


Figure 4.43 Raman data for higher power (4W RF) film - 520cm^{-1} peak is clearly visible indicating that the film has become crystalline

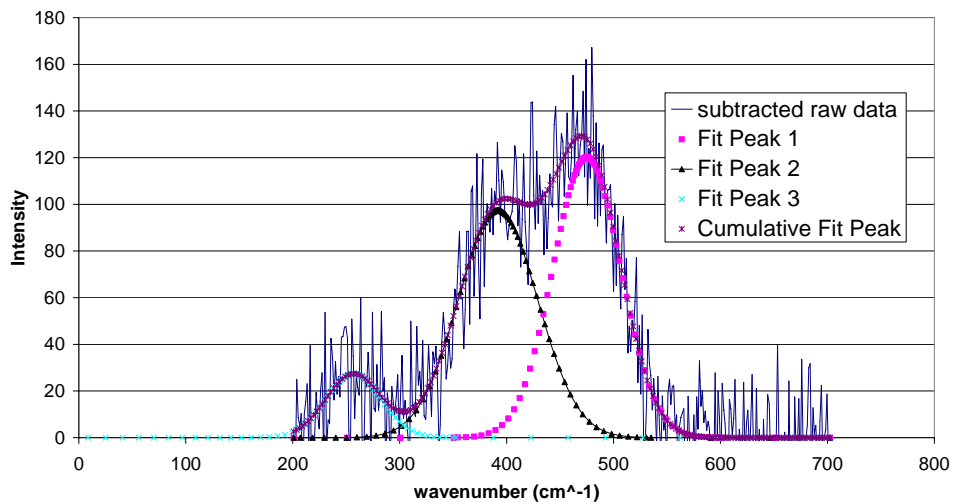


Figure 4.44 Raman data for low power (2W RF) film - Film is amorphous

(VIII) Final device results

The best quality CA device shown above has a FF of $\sim 65\%$ and a bandgap of about 1.56 eV. The Ge content for both CA (fabricated at 2 W Rf power) and NON CA (fabricated at 4W Rf power) device has been measured $\sim 14\%$. The absorption

energy curve for both CA and NON CA devices has been shown below - the Urbach energy has been measured to be about 48 meV for both CA and NON CA devices. The gas flows were -55 Scm H₂, 23 Scm Ar, 4scm SiH₄, .4 scm Geh₄

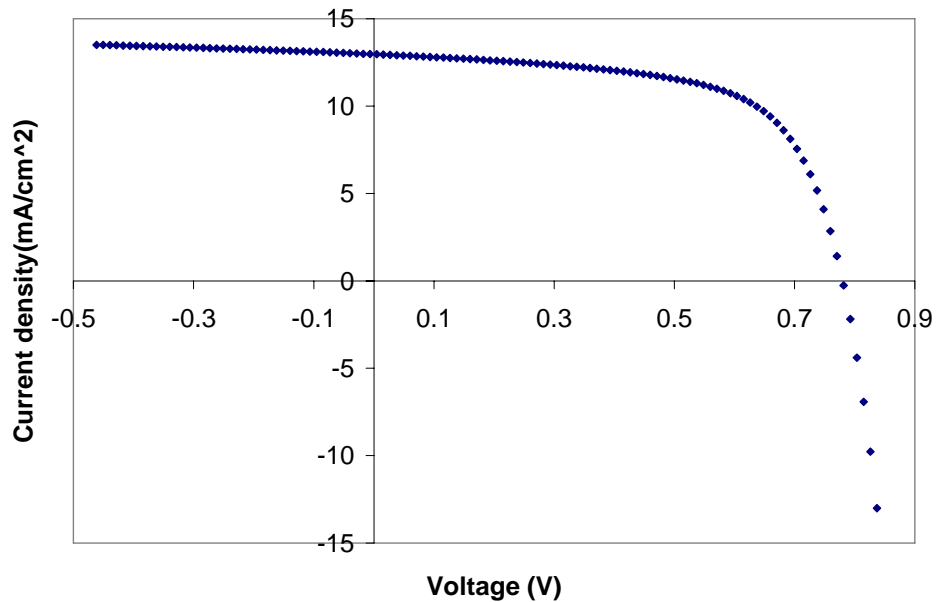


Figure 4.45 Best quality CA device till now -I layer thickness =.3 microns, $J_{sc}=12.95\text{mA}/\text{cm}^2$, $V_{oc}=.78$, $FF=65.4$ (Fabrication temp ~ 250C)

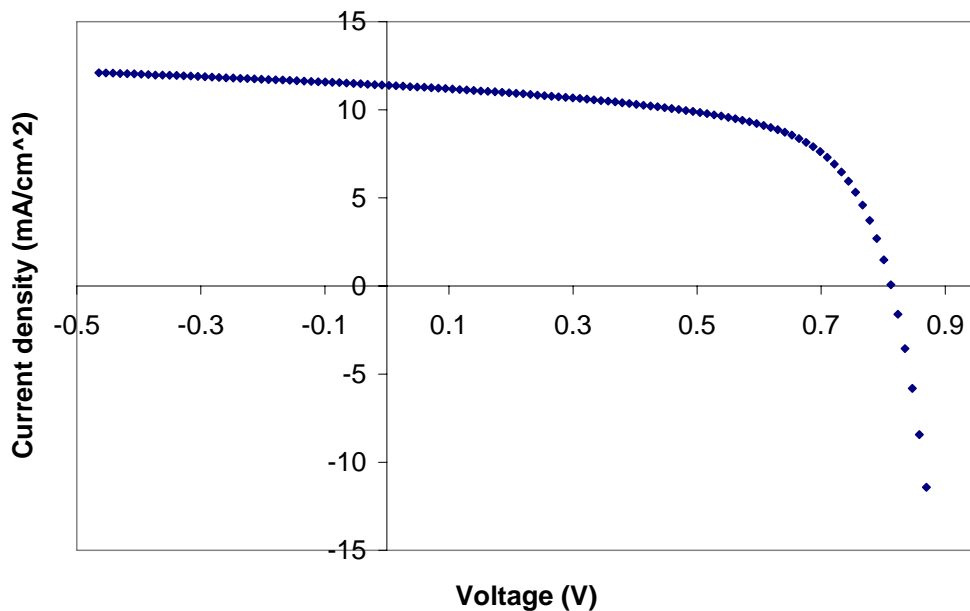


Figure 4.46 Best quality NON CA till now -I layer thickness =.26 microns, $J_{sc}=11.38\text{mA}/\text{cm}^2$, $V_{oc}=.82$, $FF=64\%$ (Fabrication temp ~ 250C)

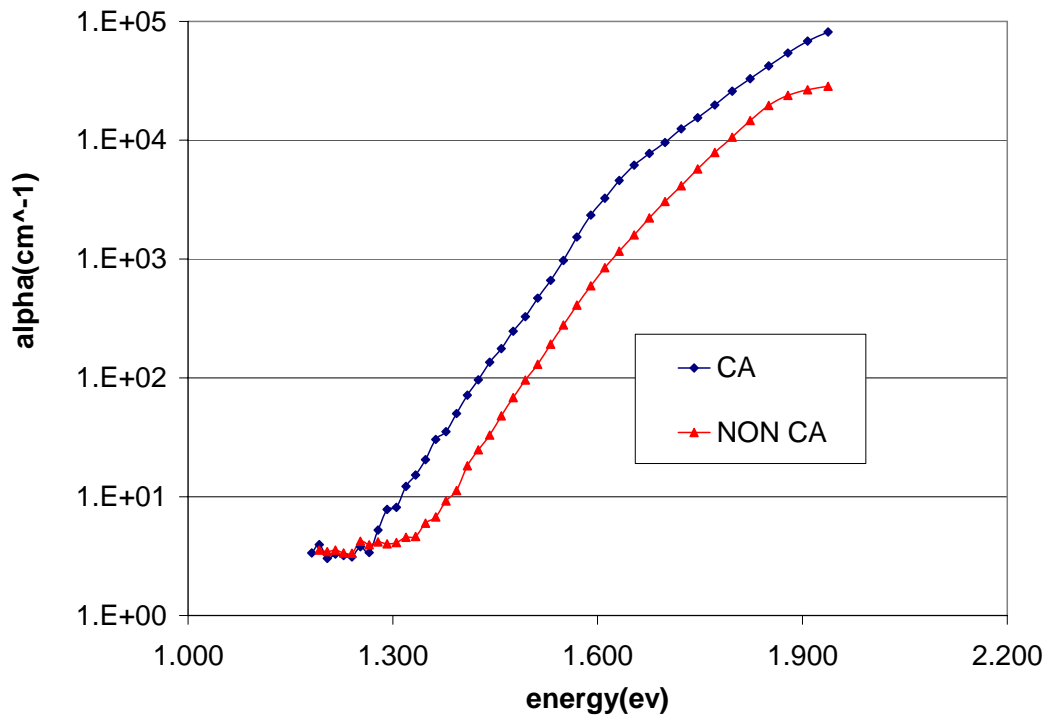


Figure 4.47 Absorption energy curve for CA vs NON CA

(IX) Hole mobility product for CA vs NON CA device

Just like for A-Si, thicker A-SiGe devices (around .6 micron) were fabricated for measuring hole mobility product. The hole mobility product for NON CA A-Si Ge ($E_g \sim 1.63$ eV and Urbach energy of around 48 meV, as shown in Figure 4.50) has been measured to be around 9.4×10^{-9} cm²/V. The methodology is same as for a-Si- the value of mobility lifetime product which gives us the best possible fit of theoretical and measured QE vs bias for three wavelengths – 600 nm, 680 nm and 760 nm has been reported as correct hole mobility lifetime product value. For the best quality thick ($\sim .6$ micron) 1.56 eV CA device so far , Hole mobility Lifetime product of about 8.4×10^{-9} cm²/V has been obtained . Work is currently underway to obtain better quality thick CA device , so we expect to be able to report a better quality CA devices with higher hole mobility lifetime product very soon in near future

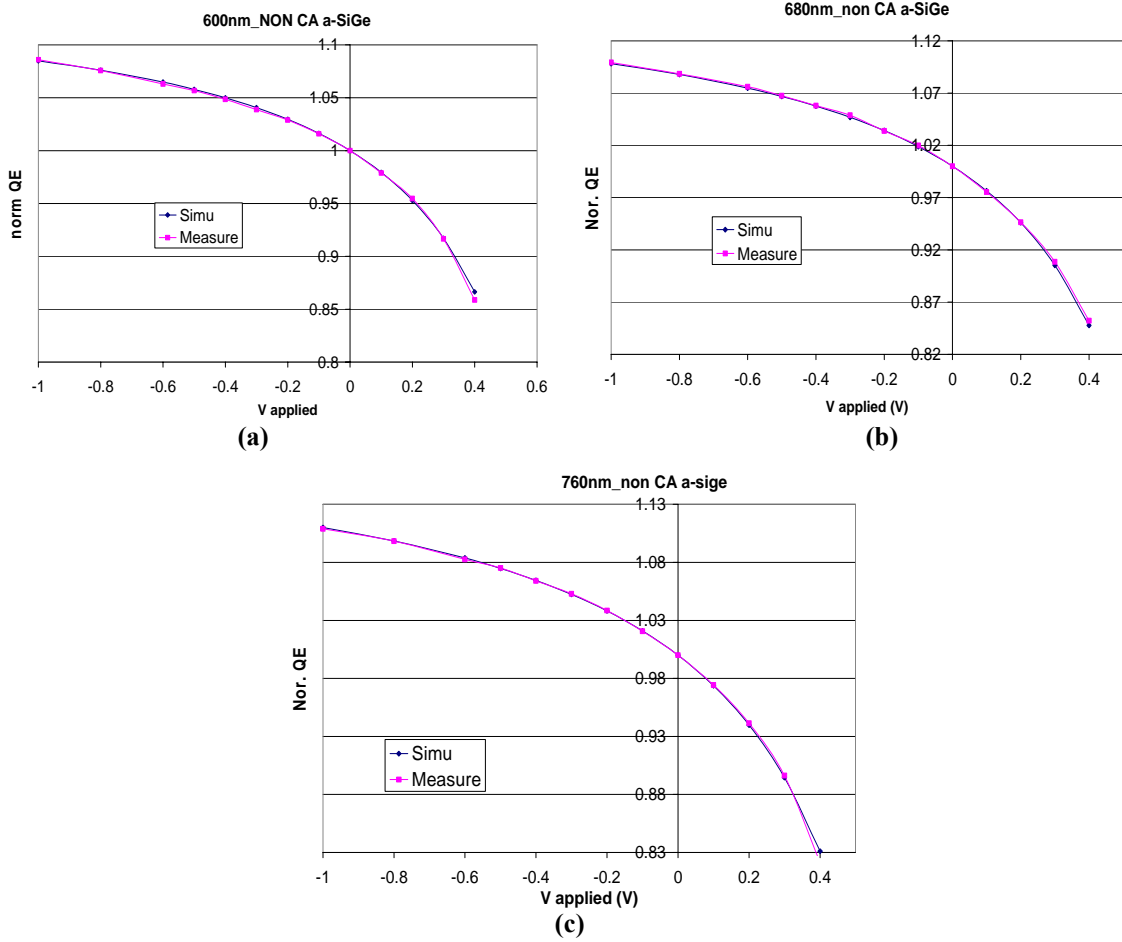
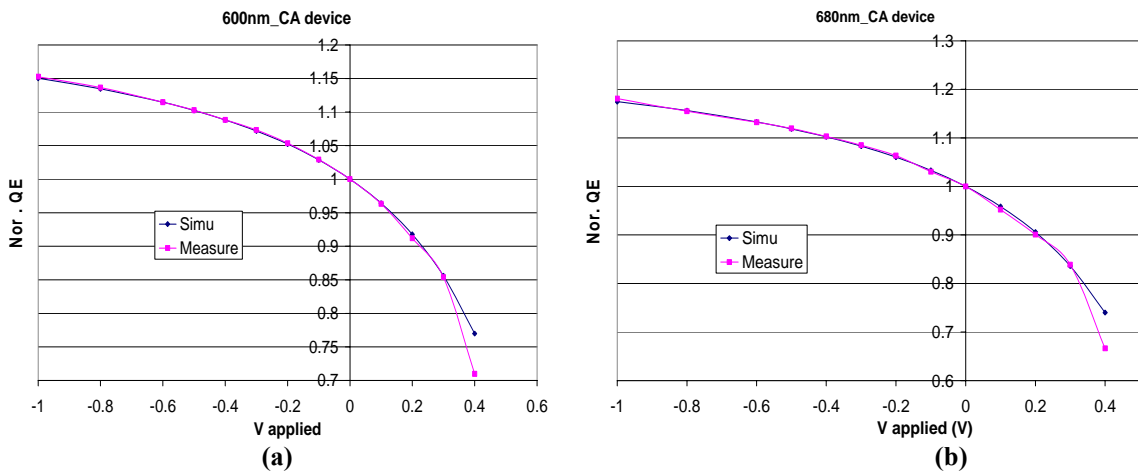
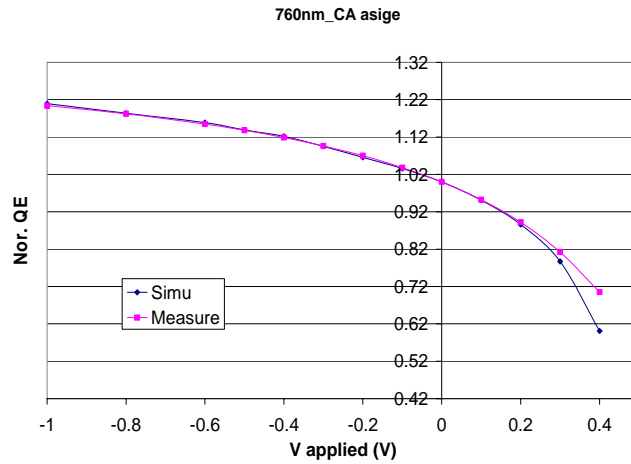


Figure 4.48 Simulation and measured QE vs bias for 1.63 eV NON CA device at (a) 600 nm (b) 680 nm and (c) 760 nm





(c)

Figure 4.49 Simulation and measured QE vs bias for 1.56 eV CA device at (a) 600 nm (b) 680 nm and (c) 760 nm

(X) Defect density calculations

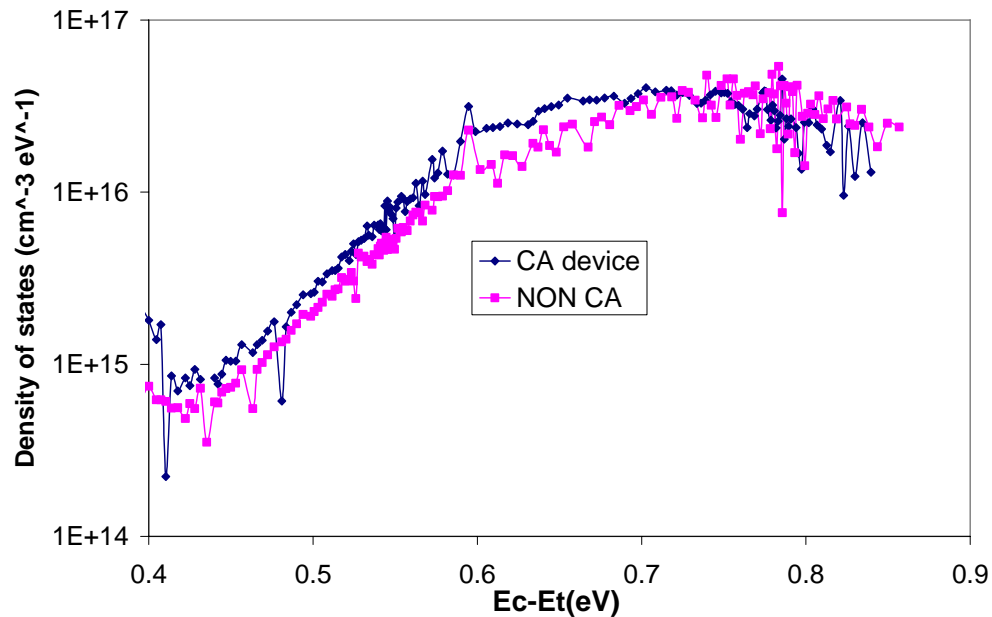


Figure 4.50 Density of states plot for CA and NON CA

Plot of Density of states for best quality CA and NON CA fabricated till date is shown in Figure 4.50 and its corresponding Absorption energy plot is shown below. From the Absorption curve, it can be seen that not only is Urbach energy same for both the cases (~ 48 meV), the absorption shoulder is almost identical which means that the defect density should be the same for CA and NON CA. Indeed when

integrated defect density is calculated from fitting Gaussian to density of states plot shown above, their calculated defect density is same as well ($\sim 2 \cdot 10^{16} \text{ cm}^{-3}$)

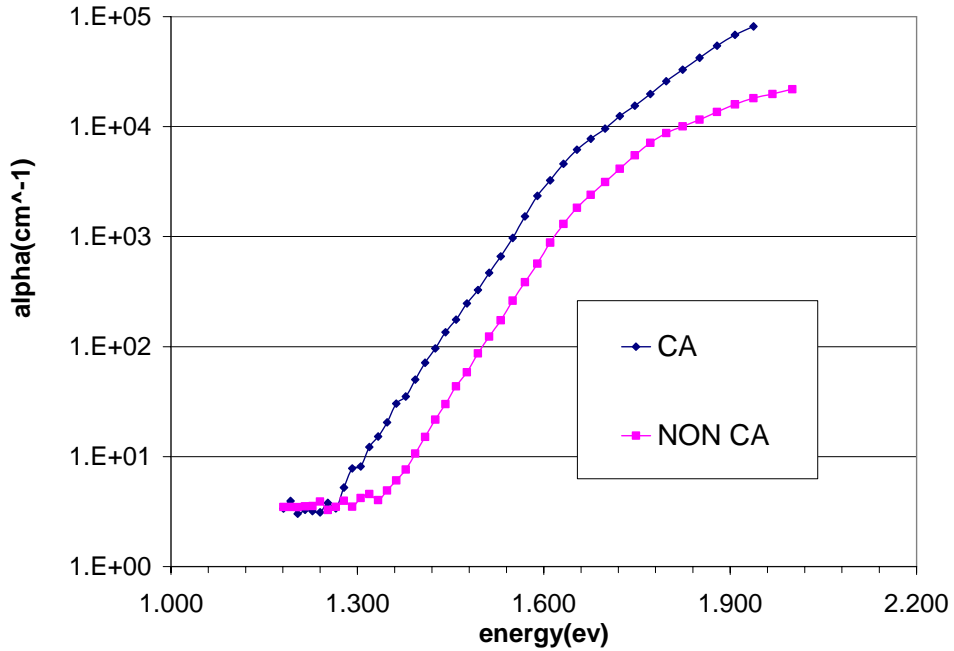


Figure 4.51 Absorption energy curve for CA vs NON CA

(b) *Film Results*

(I) H content data

Hydrogen content as a function of CA

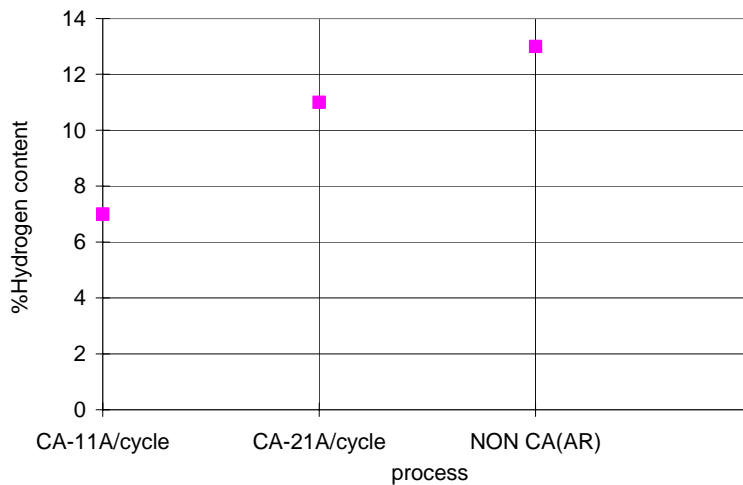


Figure 4.52 Hydrogen content data for CA vs NON CA

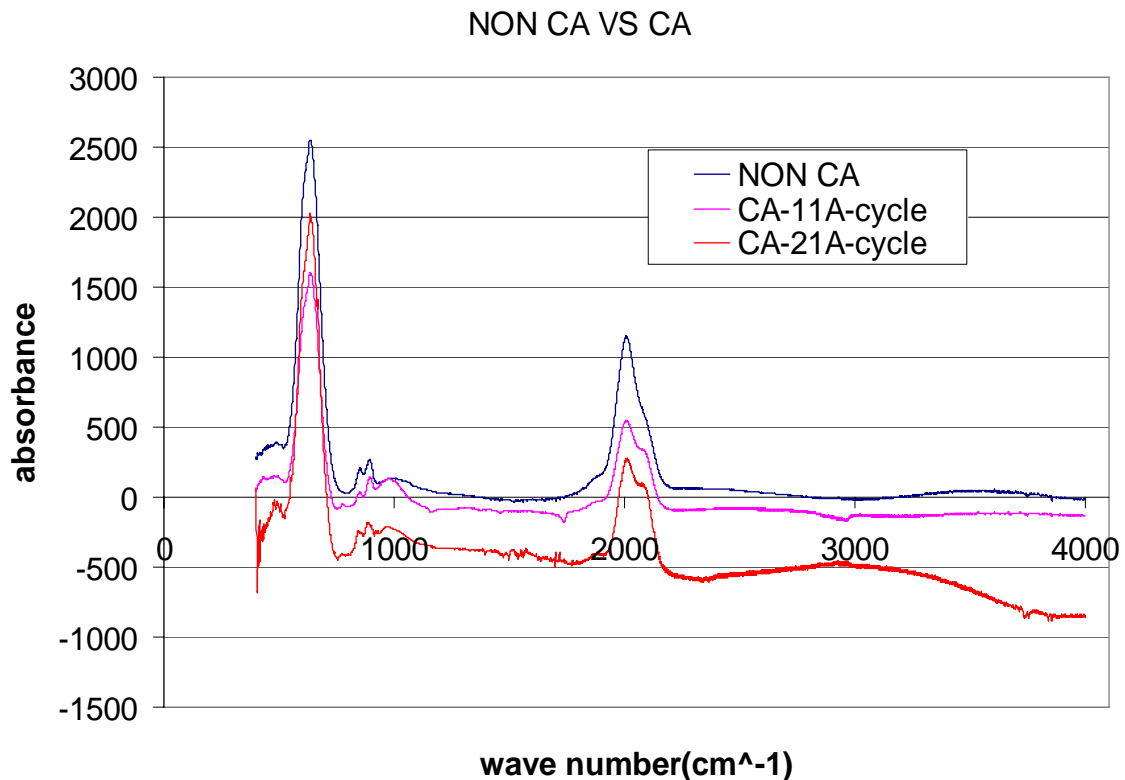


Figure 4.53 FTIR raw data obtained – absorbance vs wave number for various CA processes and NON CA

From the FTIR raw data, we can see that lowest growth per cycle has the lowest hydrogen content – a trend similar to what we saw for A-Si. This upholds our theory that when the growth per cycle is reduced, Ar can penetrate deeper inside the material and successfully cause more ion bombardment –which will lead to lower bandgap as a consequence of lower Hydrogen content.

It is however, seen that SiH/ SiH₂ peak area data (ie 2000 and 2100 cm⁻¹) shows a weird trend- it seems to be lower for CA as compared to NON CA, which is completely contrary to what is expected. Interestingly, a similar trend was observed for A-Si. One of the reason proposed for this anomalous behavior is the presence of some crystallites, which could not be picked up by Raman, probably because these crystallites are not close to the surface.

(II) Electronics properties of films grown

For completion of research work, a few films were fabricated to see if the results follow the same trend as for devices. In all the case H₂ flow of 55 sccm, Ar flow of 23 sccm and GeH₄ flow of .4 sccm was maintained.

Table 4.3 Comparison of optical and electronic properties of CA and NON CA A-SiGe films

Sample	SiH ₄ ,GeH ₄ (sccm/sccm) RF power	PC (1/Ωcm)	DC (1/Ωcm)	Activation Energy(eV)	Urbach energy (meV)	Tauc (eV)
2-15275 NON CA	4 ,4 4.5 W RF	9.33E-6	7.01E-10	0.833	48	1.63
2-15279 CA film	4,4 2 W RF	9.69E-6	1.38E-9	.808	48	1.57
2-15443 NON CA	3,,3 4.5 W RF	8.28E-7	9E-10	.822	55	1.61
2-15449 NON CA	2,,3 2W RF	5.09E-07	1.5E-09	.799	60	1.58

The properties of films grown are shown above are shown above. The growth condition for the first two films (2-15275 and 2-15279) are identical to the best CA and NON CA device I layers reported in Sec 4.2.VIII. The light conductivity and Urbach energy values are comparable for CA and NON CA, whereas Dark conductivity value is higher for CA indicating bandgap reduction, which is in agreement with Tauc's gap reported for both cases. Furthermore, absorption energy data for the two abovementioned film proves reduction in bandgap of CA films compared to NON CA case. The growth conditions for the films 2-15443 and 2-15449 are identical to the I layers grown for the Case 2 and Case 3 reported in section 4.2.VII. The Photoconductivity values for these films are about an order

lower than that for 2-15275 NON CA, indicating poorer quality. The Urbach energy values are also much higher for these films again confirming that film quality is poor, which is in agreement with device results displayed in Sec 4.2.VII.

NON CA films vs CA

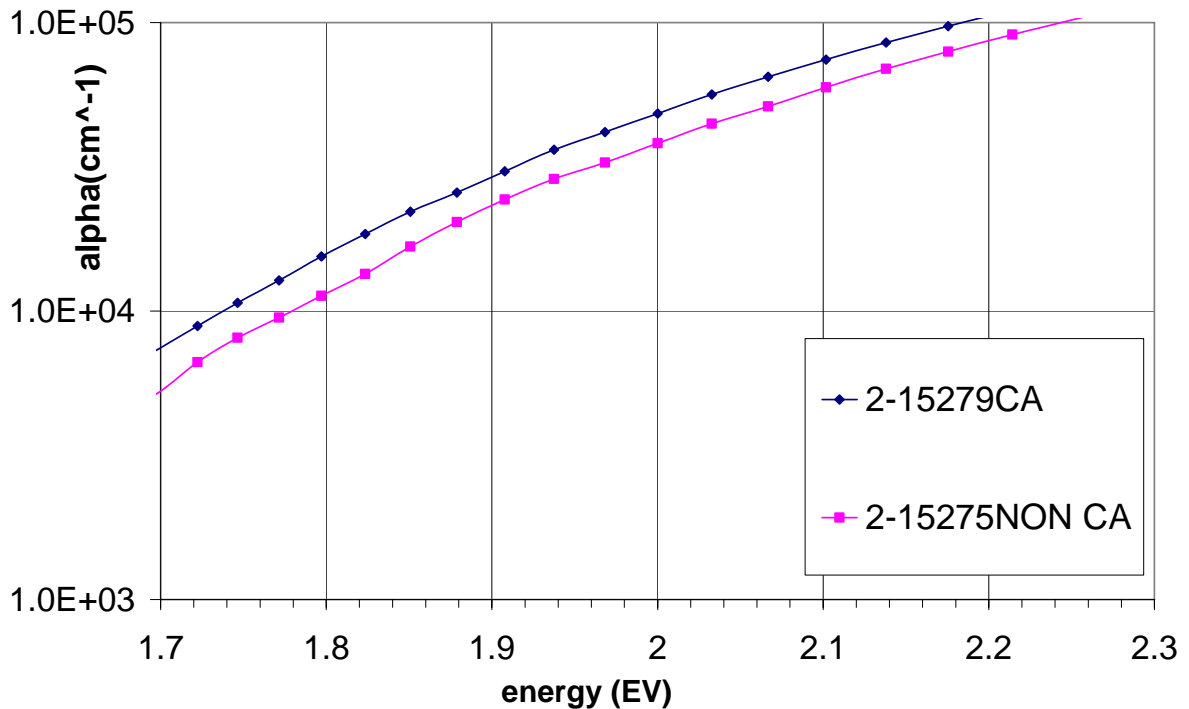


Figure 4.54 Comparison of Absorption energy curves for CA vs NON CA obtained by Spectrophotometry

(c) Summary for A-SiGe chemical annealing

We can summarize the above results and parameters for A-SiGe chemical annealing as following for obtaining best possible results:-

- (i) The most important parameter is low growth per cycle- any and all parameters that lead to this will cause better chemical annealing
- (ii) Importance of Optimum pressure is highlighted again- this will facilitate optimum ion bombardment without adversely affecting device quality.
- (iii) It is essential to use lower power for CA as higher power leads to lower Ge content
- (iv) It is important that we compare CA and NON CA having identical SiGe

(v) Rf power has an important role in deciding crystallinity when $H_2:SiH_4$ dilution is very high

(vi) Film results agree very well with device results- they are following the same trend as devices thus far

We thus can conclude saying that we have successfully been able to reduce bandgap using chemical annealing for A-SiGe as well. All the important observations have been summarized above.

CHAPTER 5 CONCLUSION

We have seen that Chemical annealing by Ar when done under optimum conditions is successful in lowering the bandgap for both A-Si and A-SiGe without adversely affecting growth per cycle. We have tried varying parameters like growth time, reducing pressure and they have been successful in reducing bandgap by facilitating reduced growth per cycle. Low pressure is very successful in reducing bandgap as it leads to higher ion bombardment, however too low pressure can adversely affect device properties by increasing midgap state densities. The reason we stress on low growth per cycle is because Ar being bulkier than H cannot penetrate as deep as H. So unless we keep layers between 7-15 Å/cycle we cannot expect to have effective ion bombardment of the entire layer. Extensive light soaking test prove that CA have better stability than NON CA- which proves that chemical annealing is successful in reducing weak Si-H bond content. Till now best quality CA and NON CA A-Si solar cells have a FF of 65%, and Urbach energy of 45 meV and hole mobility lifetime product of about 3.6×10^{-8} cm²/V. E_g of 1.62 eV has been achieved for CA which is much lower compared to 1.78 eV for NON CA (Ar). Films fabricated also agree very well with device results. FTIR studies confirm drop in bandgap as a result of decrease in hydrogen content, with lowest Hydrogen content of 4 atomic % being obtained for 9Å /cycle.

In case of A-SiGe, it is crucial that we maintain same SiGe composition for CA and NON CA, otherwise we won't be seeing expected result of chemical annealing having lower bandgap than NON CA. Till now for A-Si we have achieved 1.62 eV and for A-SiGe 1.56 eV. FF of solar cells are around about 65% indicating high quality. Furthermore, Urbach energy for best quality CA and NON CA cells are about 48 meV. So far best quality CA device has a mobility lifetime product of slightly excess of 8×10^{-9} cm²/V, indicating high quality. Film results correlate very well with device results. Like A-Si, FTIR measurements again confirm decrease in Hydrogen content in CA samples compared to NON CA.

To conclude, we have managed to prove chemical annealing is successful in lowering bandgap without affecting material quality for both a-Si and a-SiGe.

REFERENCES

- [1] R. A. Street, Technology and Applications of Amorphous Silicon, Springer-Verlag Berlin Heidelberg (2000).
- [2] R. A. Street, Hydrogenated Amorphous Silicon, Cambridge Solid State Science Series (1986).
- [3] M.J. Powell, IEEE Trans. on Electron. Devices, 36 (12) (1989) 2753.
- [4] P.G Le Comber, Journ. of Non-Crystalline Solids ,115(1-3)(1989) 1-13
- [5] REI Schropp, Amorphous and microcrystalline silicon solar cells: modeling, materials, and device technology, Kluwer Academic publishers (1998)
- [6] D.E. Carlson & C. R. Wronski, Appl. Phys. Lett., 28 (1976) 671
- [7] D.E. Carlson & C. R. Wronski, 18th Annual Electronic Materials Conference, Salt Lake City, UT(1976).
- [8] C.R. Wronski, D.E. Carlson and R.E. Daniel, Appl. Phys. Lett., 29 (1976) 602
- [9] D.E Carlson, IEEE Trans. on Electron. Devices, 24(4) (1977) 449.
- [10] Larry E. Antonuk, John M. Boudry, Chung-Won Kim, M. Longo, E. J. Morton, John Yorkston and Robert A. Street, Proc. SPIE, 1443(1991) 108
- [11] J. Mort, F. Jansen, S. Grammatica, M. Morgan, and I. Chen, J. Appl. Phys., 55 (1984) 3197
- [12] K.Tanaka, E.Maruyama, et al., Amorphous Silicon, John Wiley & Sons, New York, (1998)
- [13] Nanlin Wang, Improving the stability of amorphous silicon solar cells by chemical annealing (ISU, dissertation, 2006)
- [14] D.L. Staebler and C.R. Wronski, Appl. Phys. Lett., 31 (1977) 292
- [15] I. Shimizu et al, Sol. E. Mat. & Sol. Cells 66 (2001) 329
- [16] A. Madan, M.P. Shaw, The Physics an Applications of Amorphous Semiconductors, Academic Press, Inc. San Diego, California (1998)
- [17] J.H. Moller, Semiconductors for Solar Cells, Artech House Inc., Boston, MA (1993)
- [18] W. Luft and Y. Tsuo, Hydrogenated Amorphous Silicon Alloy Deposition Processes, Marcel Dekker, Inc., New York, (1993)

- [19] Kim, Ji Cheol and Schwartz, Richard J., Parameter Estimation And Modeling Of Hydrogenated Amorphous Silicon, ECE Technical Reports, Paper 89 (1996).
- [20]. M. H. Cohen, H. Fritzsche, and S. R. Ovshinsky, Simple band model for amorphous semiconducting alloys, *Phys. Rev. Lett.*, 22 (1969) 1065-1068
- [21] T. Tiedje, J. M. Cebuka, D. L. Morel, and B. Abels, Evidence for exponential band tail in amorphous silicon hydride, *Phys. Rev. Lett.*, 46 (1981) 1425- 1428
- [22] H. Dersch, J. Stuke, and J. Beichler, Electron spin resonance of doped glow discharge amorphous silicon, *Phys. Status Solidi (B)*, 105(1981) 265-274,
- [23] Y. Kazama, K. Seki, W. Kim, M. K. S. Yamanaka, and K. Takahashi, High efficiency amorphous silicon solar cells with delta-doped p-layer, *Jap. J. Appl. Phys.*, 28(July 1989) 1160-1164.
- [24] D. Adler, *Semiconductors and Semimetals*, 21 Academic Press, New York, (1984)
- [25] N. F. Mott and E. A. Davis, *Electronic processes in non-crystalline materials*, Clarendon Press, (1979).
- [26] E. A. Davis and N. F. Mott, Conduction in non-crystalline systems. v. conduction, optical absorption and photoconductivity in amorphous semiconductors, *Phil. Mag.*, 22(1970) 903-922.
- [27] J. M. Marshall and A. E. Owen, Drift mobility studies in vitreous arsenic triselenide, *Phil. Mag.*, 24(1971) 1281-1301.
- [28] R. A. Street, Luminescence and recombination in hydrogenated amorphous silicon, *Adv. Phys.*, 30(5) (1981) 593-676
- [29] B. A. Wilson, A. M. Sergent, and J. P. Harbison, Radiative recombination at dangling bonds in a-Si:H, *Phys. Rev. B*, 30(1984) 2282-2285.
- [30] R. A. Street, D.K. Biegelsen, and R. L. Weisfield, Recombination in A-Si:H: Transitions through defect states , *Phys. Rev. B*, 30(1)(1984) 5861-5870.
- [31] K. Morigaki, Y. Sano, and I. Hirabayashi, Radiative and non Radiative recombination processes in hydrogenated amorphous silicon as elucidated by optically detected magnetic resonance, *Solid St. Commun.* , 39 (1981) 947-951.
- [32] J. C. Knights, G. Lucovsky, and R. J. Nemanich, Defects in plasma-deposited a-Si:H, *J. of Non-Crys. Sol.*, 32 (1979) 393-403.

- [33] K. Maschke, E. Merk, and W. Czaja, Thermalization and Radiative recombination of photo-excited carriers in a-Si:H, *Phil. Mag. Lett.*, 56(4) (1987) 457-470.
- [34] W. M. Pontuschka, W. W. Carlos, P. C. Taylor, and R. W. Griffith, Radiation induced paramagnetism in a-Si:H, *Phys. Rev. B*, 25 (1982) 4362-4376
- [35] A. Morimoto, T. Miura, M. Kumeda, and T. Shimizu, Defects in hydrogenated amorphous silicon-carbon alloy films prepared by glow discharge decomposition and sputtering, *J. Appl. Phys.*, 53 (1982) 7299-7305.
- [36] M. Stutzmann, Occupancy of dangling bond defects in doped hydrogenated amorphous silicon, *Solid St. Commun.* 62 (3)(1987) 153-157.
- [37] S. R. Elliot, Defect states in amorphous silicon, *Phil. Mag. B*, 38(4) (1978) 325-334.
- [38] S. R. Elliot, Photo-induced changes in glow-discharge-deposited amorphous silicon: the Staebler-Wronski effect, *Phil. Mag. B*, 39(4) (1979) 349-356.
- [39] D. Adler, *Handbook on semiconductors*, North-Holland Publ. Co., Amsterdam, 1(1982) 805-841
- [40] Y. Bar-Yam and J. D. Joannopoulos, Dangling bond in a-Si:H, *Phys. Rev. Lett.*, 56 (May 1986) 2203-2206.
- [41] M. Stutzmann, Weak bond-dangling bond conversion in amorphous silicon, *Phil. Mag. B*, 56(1) (1987) 63-70.
- [42] Z. E. Smith and S. Wagner, Band tails, entropy, and equilibrium defects in hydrogenated amorphous silicon, *Phys. Rev. Lett.*, 59(Aug 1987) 688-691.
- [43] R. A. Street and K. Winer, Defect equilibria in undoped a-Si:H, *Phys. Rev. B*, 40 (1989) 6236-6649.
- [44] K. Winer, Defect formation in a-Si:H, *Phys. Rev. B*, 41(June 1990)12150-12161.
- [45] K. Pierz, W. Fuhs, and H. Mell, On the mechanism of doping and defect formation in a-Si:H, 63(1) (1991) 123-131.
- [46] Z. Vardeny and J. Tauc, Method for direct determination of the effective correlation energy of defects in semiconductors: Optical modulation spectroscopy of dangling bonds, *Phys. Rev. Lett.*, 54(April 1985) 1844-1847.
- [47] M. Stutzmann, The defect density in amorphous silicon, *Phil. Mag. B*, 60(4) (1989) 531-546.

- [48] K. Winer, Chemical-equilibrium description of the gap-state distribution in a-Si:H, *Phys. Rev. Lett.*, 63(1989) 1487-1490.
- [49] G. Schumm and G. H. Bauer, Thermodynamic equilibrium gap-state distribution in undoped a-Si:H, *Phil. Mag. B*, 64 (4) (1991) 515-527.
- [50] Li Zhao & V Dalal, To be published IPRS (2011).
- [51]. S. Miyazaki, N. Fukuhara and M. Hirose, *J. of Non-Crystalline Solids*, 266 (2000) 59
- [52]. W. Futako et al., *J. Appl. Phys*, 84(3) (1998) 1333
- [53]. I. Shimizu et al, *Mat. Res. Soc. Symp. Proc.* 507 (1998) 211
- [54]. I. Shimizu et al, *J. of Non-Crystalline Solids* 63 (1998) 227–230
- [55]. I. Shimizu et al, *Sol. E. Mat. & Sol. Cells* 66 (2001) 321
- [56] V.L. Dalal et al., *Mat. Res. Soc. Symp. Proc.* 149 (1989) 601
- [57] H. M. Branz, *Phys. Rev. B*, 59 (8), (1999) 5498
- [58] J.B. Dresner, B. Goldstein and D. Szostak, *Appl. Phys. Lett.*, 38 (1981) 998
- [59] R. Biswas, B.C. Pan, and Y. Ye, Metastability of amorphous silicon from silicon network rebonding, *Phys. Rev. Lett.*, 88(2002) 205502 .
- [60] R. Biswas, B.C. Pan, Defect kinetics in new model of metastability in a-Si:H, *Journal of Non-Crystalline Solids*, 299-302(2002) 507
- [61] H. Branz, H collision model, *Phys. Rev. B* 59(1999) 5498
- [62] R. Biswas and B.C. Pan, Microscopic nature of Staebler-Wronski defect formation in amorphous silicon, *Appl. Phys. Lett.*, 72(1998) 371
- [63] R. Biswas, Q. Li, B.C. Pan, Y. Yoon, Mechanism for hydrogen diffusion in amorphous silicon, *Phys. Rev. B.*, 57(1998) 2253
- [64] Q. Li and R. Biswas, Hydrogen Rebonding and defect formation in a-Si:H, *Phys. Rev. B.*, 52(1995) 10705
- [65] R. Biswas, and Y.P. Li, H-flip model of light induced changes of amorphous silicon, *Phys. Rev. Lett.* ,82(1999) 2512.
- [66] V.L. Dalal, E. Ping et al., *Appl. Phys. Lett.*, 64 (1994) 1862
- [67] V.L. Dalal et al., *J. J. of Non-Crystalline Solids*, 227-230 (1998) 1257
- [68] A. H. Mahan, J. Carapella et al., *Appl. Phys. Lett.*, 64 (1991) 1862

- [69] E. Maruyama, S. Tsuda, S. Nakano, Hydrogenated amorphous silicon, Neber-Aeschbacher H. (Ed.), Science Publication, Zurich, Part 2, 44-46(1995) 863
- [70] V.L. Dalal and Greg Baldwin, Mat. Res. Soc. Symp. Proc., 297 (1993) 833
- [71] R.E.I. Schropp, Hydrogenated amorphous silicon, Neber-Aeschbacher H. (Ed.), Science Publication, Zurich, Part 2, 44-46 (1995) 853-861
- [72] S. Guha, in: R. Street (Ed.), Technology and applications of amorphous silicon, Spring, Berlin, 37 (1999) 252.
- [73] X. Xu, J. Yang, S. Guha, Thin solid films 198-200 (1996) 60
- [74] N. Souffi, A. Matsuda et al., Solid State Commun. 122 (2002) 259
- [75] G. Gaungly, A. Matsuda, Phys. Rev. B 49 (1994) 10986
- [76] T. Nishimoto, T. Takagi et al., Solar Energy Materials & Solar Cells, 66 (2001) 179
- [77] K. Ohkawa, S. Shimizu et al., Solar Energy Materials & Solar Cells, 66 (2001) 297
- [78] Ganguly et al, J. of Non-Crystalline Solids 198-200 (1996) 559-562
- [79] S. Ray et al, J. Appl. Phys. 75 (1994) 7340-7348
- [80] S.Ray et al, J. of Non-Crystalline Solids 211 (1997) 22-29
- [81] Dalal, Kaushal et al, Proceedings of 1st World Conference on Photovoltaic Energy Conversion (1994) 464- 467
- [82]Matthew Ring, The effects of ion bombardment during deposition upon the properties of hydrogenated amorphous silicon-germanium thin films and photovoltaic devices (ISU dissertation, 2004)
- [83] H. Aguas, R. Martins, and E. Fortunato, Role of ion bombardment on the properties of a-Si:H films, Vacuum, 60(2001) 247
- [84] T. Sasaki and Y. Ichikawa, Effect of ion bombardment during plasma CVD on the film properties of a-Si:H studied by IEC plasma CVD, J. Non-Cryst. Solids, 198-200 (1996) 1007.
- [85] P. Roca i Cabarrocas, Detailed study of ion bombardment in rf glow discharge systems: role of helium dilution, Mat. Res. Soc. Symp. Proc., 149(1989) 33
- [86] W.C. Weller and G.H. Bauer, Correlation between microstructure and optoelectronic properties of a-SiGe:H, Mat. Res. Soc. Symp. Proc., 149(1989) 339
- [87] Yong Liu, Puneet Sharma, Vikram Dalal, Photovoltaic Specialists Conference Conference Record of the Twenty-Ninth IEEE , (2002) 1154- 1157

- [88] S. Guha et al., *Appl. Phys. Lett.* 54(1989) 2330
- [89] Baldwin et al, *Proceedings of 23rd. IEEE Photovoltaic Spec. Conf.*,(1993) 1037-1042.
- [90] V. L. Dalal et al, *Proc. Of 26th . IEEE Photovolt. Spec. Conf.*, p. 698 (1997)
- [91] Dalal et al, *Mat. Res. Soc. Symp. Proc. Vol. 609*(2000)
- [92] A. Matsuda, M. Koyama, N. Ikushi et al., *Japn. J. Appl. Phys.* 25 (1986) 54
- [93] J. Perrin, M. Shiratani, K. Patrick et al., *J. Vac. Sci. Technol. A* 16(1) (1998) 278
- [94] A. Gallagher, *J. Appl. Phys.*, 63(7) (1988) 2406
- [95] V.L. Dalal, *Thin Solid Films*, 395 (2001) 173
- [96] V.L. Dalal, R. Knox et al., *Conference Record of the IEEE Photovoltaic Specialists Conference*, 22nd (2) (1991) 1399.
- [97] S. K. Kaushal, *Growth of high Quality a-(Si,Ge):H films using low pressure, remote ECR plasma technique* 17, (ISU, thesis, 1995)
- [98] V.L. Dalal, T. Maxson et al., *J. of Non-Crystalline Solids*, 227-230 (1998) 1257.
- [99] Michael William Beckman, *The effects of low pressure helium ion bombardment on hydrogenated amorphous Silicon* (ISU, dissertation, 2008)
- [100] Atul Madhavan, *Alternative designs for nanocrystalline silicon solar cells* (ISU, dissertation, 2009)
- [101] F Finger et al, *Journal of Non-Crystalline Solids* 137&138 (1991) 347-350
- [102] M. Hack, & M. Shur, *J. Appl. Phys.*, 58 (1985) 1997
- [103] G. Baldwin, *Design and modeling of a graded bandgap amorphous silicon solar cell deposited by plasma enhanced chemical vapor deposition*, (ISU thesis, 1994)
- [104] V.L. Dalal, and F. Alvarez, *Journal De Physique, Supplement C4*, 42 (1981) 491
- [105] D.E. Crandall, and C.R. Wronski, *Appl. Phys. Lett.*, 28 (11) (1976) 671
- [106] Daniel Congreve, *Calculation of defect densities in nano-crystalline and amorphous silicon device using differential capacitance measurements*, (ISU thesis, 2011)
- [107] T. Walter, R. Herberholz, C. Muller, and H. W. Schock, *Determination of defect distributions from admittance measurements and application to Cu(In,Ga)Se₂ based heterojunctions*. *Journ. of Appl. Phys.* 80(8). (October 1996) 15
- [108] M.H. Brodsky, M. Cardona, and J.J. Cuomo, *Phys. Rev. B*, 16 (1977) 3556
- [109] M. Bermejo, M. Cardona, *J. of Non-Crystalline Solids*, 32 (1979) 413

[110] A. Shah, J. Meier, E. Vallat-Sauvain, *Solar Energy Materials and Solar Cells*, 78(2003) 469-491

ACKNOWLEDGEMENTS

I would like to first and foremost thank my Advisor Prof Vikram Dalal for his significant role in placing me where I am today. I would not have been where I am today had it not been for his constant guidance and fatherly help and care. I still remember the classes I took with him, in which I had learnt difficult concepts with so much ease.

My parents also have been constant the source of guidance and inspiration. My father being a world renowned nuclear physicist (Prof Radhey Shyam) had always encouraged me to follow my dreams and it has been a constant effort of mine to follow in his footsteps to try and come close to matching his celebrated career. My mom has always been by my side and never for once allowed me to feel the pain of the death of my biological mother- she had taught me the importance of being disciplined, hard working and always protected me from the harsh, unforgiving real world.

Probably the other most important person to thank will be my dear wife, Upasana and sister-in-law Upabali. The years of Phd have been the most difficult ones of my life and I would not have managed to pull it off without their love, affection and care. They have always managed to bring a smile on my face, even under the worst circumstances and have always been there for me when I needed some support. I am indeed been blessed to have them in my life.

Of course it would be unfair to forget my friends and colleagues in MRC whose help and support was instrumental in my completion of PhD namely Max Noack, Nayan, Kanwar , Sambit , Mehran Samiee Esfahani , Keqin Han ,Siva, Shantan, Ron, Atul, Satya, Ted , Brian Wellington Lewis, Michael Beckmann and others.

I would also like to thank NSF, Power Fund and Micron for funding my research work ; Materials Analysis and Research Laboratory for EDS, Back scattered imaging analysis and X –ray analysis and my POS committee members - Prof Sumit Chaudhury, Prof Joseph

Shinar, Prof Rana Biswas, Prof Mani Mina and Prof Ruth Shinar for healthy discussions and guidance concerning my research.